Acta Polytechnica

Editorial Board:

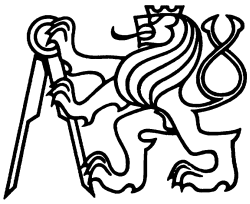

Title of journal: Acta Polytechnica. **Volume:** 63. **Number:** 1.
Periodicity: Bimonthly; 6 issues per year. **Date of issue:** February 28, 2023.
Published by: Czech Technical University in Prague,
Jugoslávských partyzánů 1580/3, 160 00 Praha 6 – Dejvice, Czech Republic.
IČO: 68407700.

Editorial Office: CTU — Central Library,
Technická 6, 160 80 Praha 6, Czech Republic.
acta@cvut.cz

Acta Polytechnica is available at http://ojs.cvut.cz/ojs/index.php/ap
Each article is assigned a digital object identifier https://doi.org/10.14311/AP.2023.63.⟨*4-digit article page number*⟩

ISSN 1805–2363 (online) MK ČR E 4923

Dear Reader

The Acta Polytechnica journal that you have just opened is a scientific journal published by the Czech Technical University in Prague. This journal first appeared in 1961 under the name "Proceedings of the Czech Technical University". The main purpose of the journal was to support publication of the results of scientific and research activities at the Czech technical universities. Five years later, in 1966, the name of the journal was changed to Acta Polytechnica, and it started appearing quarterly. The main title Acta Polytechnica is accompanied by the subtitle Journal of Advanced Engineering, which expresses the scope of the journal more precisely. Acta Polytechnica covers a wide spectrum of engineering topics in civil engineering, mechanical engineering, electrical engineering, nuclear sciences and physical engineering, architecture, transportation science, biomedical engineering and computer science and engineering. The scope of the journal is not limited to the realm of engineering. We also publish articles from the area of natural sciences, in particular physics and mathematics.

Acta Polytechnica is now being published in an enlarged format. Our aim is to be a high-quality multi-disciplinary journal publishing the results of basic research and also applied research. We place emphasis on the quality of all published papers. The journal should also serve as a bridge between basic research in natural sciences and applied research in all technical disciplines.

We invite researchers to submit high-quality original papers. The conditions of the submission process are explained in detail on: `http://ojs.cvut.cz/ojs/index.php/ap`. All papers will be reviewed, and accepted papers are published in English.

We hope that you will find our journal interesting, and that it will serve as a valuable source of scientific information.

Editorial Board

Contents

INDUCTION MOTOR MECHANICAL DEFECT DIAGNOSIS USING DWT UNDER DIFFERENT LOADING LEVELS

Ahcene Bouzida[a,*], Radia Abdelli[b], Aimad Boudouda[c]

[a] *University of Bouira, Faculty of Sciences and Applied Sciences, Department of Electrical Engineering, 10000, Bouira, Algeria*

[b] *University of Bejaia, Faculty of Technology, Department of Electrical Engineering, 06000, Bejaia, Algeria*

[c] *University of Boumerdes, Faculty of Technology, Laboratoire Ingénierie des Systèmes et Télécommunications (LIST), 35000, Boumerdes, Algeria*

[*] corresponding author: a.bouzida@univ-bouira.dz

Abstract. The information extraction capability of the widely used signal processing tool, FFT for diagnosing induction machines, is commonly used at a constant load or at different levels. The loading level is a major influencing factor in the diagnostic process when the coupled load and the machine come with natural mechanical imperfections, and at a low load, the mechanical faults harmonics are strongly influenced. In this context, the main objective of this work is the detection of the mechanical faults and the study of the effect of the loading level on the induction motor diagnostic process. We have employed a diagnosis method based on discrete wavelet transform (DWT) for the multi-level decomposition of stator current and extracting the fault's energy stored over a wide frequency range. The proposed approach has been experimentally tested on a faulty machine with dynamic eccentricity and a shaft misalignment for three loading levels. The proposed method is experimentally tested and the results are provided to verify the effectiveness of the fault detection and to point out the importance of the coupled load.

Keywords: Induction motor, fault diagnosis, eccentricity, misalignment, DWT, energy, loading levels.

1. Introduction

Incorrect configuration of the electrical circuit and mechanical faults in industrial induction machines can lead to serious economic losses, as well as other losses in less tangible terms. If the stator or rotor are incorrectly diagnosed and interpreted as faulty (wrong diagnostic decision), there will be important costs added from the unnecessary maintenance operation, disassembly of the motor, or from a false positive decision which leads to a halt of the entire production process. In addition, the credibility and the efficiency of maintenance operations and technicians can be seriously compromised. In the opposite case, if the machine is identified as healthy (false negative), the fault can aggravate and an accelerate the degradation of the machine and the coupled load may occur. This degraded operation can result in even higher economic costs, the consequences of unplanned shutdowns of production, risks to the safety of users and damage to the company's reputation. These consequences resulting from an incorrect diagnosis of the state of the machine are not at all negligible, at least when using the techniques commonly used in the industry.

The most frequently used methods of diagnosis of mechanical and electrical defects in the industry are derived from the technique of Motor Current Signature Analysis (MCSA) when the defects are classified as electrical faults and can be easily detected by analysing the electrical signature [1–4]. This technique is often used to analyse the stator current, vibration, or torque acquired during operation using the Fast Fourier Transform (FFT). The principle of this method is based on the evaluation of the amplitudes of a predefined frequency component linked to faults. In general, induction machines have two ranges of frequencies that can be affected by faults, the first one is located in the low frequency band and the second one in the high band. Therefore, the tracking of these components without a constant load and mixed faults makes the diagnostic process very difficult and prone to errors. Otherwise, the diagnosis at the low loading level is different from the higher loading level because of the variation of fault harmonics with slip and the amplitude of space harmonics. For a diagnosis of mechanical faults, such as rotor asymmetries, load oscillations, and misalignments using the lower sideband harmonic (LSH) based approach, it is difficult to decide whether the machine is in a fault condition or not [5–7].

The presence of various phenomena in induction motors, such as load torque oscillations and voltage fluctuations, make the diagnostic process notably difficult [8–10]. Despite the prevalence of this circumstance, however, researchers have rarely probed the correlation between the presence of these phenomena and the defect in the machine. Mills, compressors, and other machines that introduce torque oscillations often use induction motors with a degree of eccentricity or even with misalignment [8]. In these instances,

the implementation of the classical FFT method imposes significant limits; the frequencies induced by load torque fluctuations and level may be identical to fault-related frequencies and magnitudes [11], resulting in a wrong diagnostic decision. The similarities between the FFT spectra of a faulty motor and the same motor in a healthy condition but operated under high load and oscillating load torque can result in such a wrong decision. The obvious similarity in spectral analysis could lead to an inaccurate diagnosis. Due to these disadvantages, alternate approaches to diagnosis based on techniques, such as the Discrete Wavelet Transform (DWT) for the analysis of the stator current under wide frequency band, becomes acceptable in this situation [12, 13]. A proposed works in [14, 15], present an effective machine-learning-based fault diagnosis method, developed for induction motors driven by variable frequency drives (VFDs). Two identical induction motors under healthy, single, and multi-fault conditions were tested in the lab. A Signal processing technique, the discrete wavelet transform, is chosen to extract features for machine learning. The derived DWT diagnosis method is proposed to detect and locate the insulated gate bipolar translator open-circuit fault. The discrete wavelet transform is used as a pre-treatment technique for three-phase output currents. Euclidean distance between every two of the energy vectors are calculated for measuring the current similarity [16].

In this study, we present a technique for diagnosing mechanical faults in induction machines. The method is contrasted with the standard decomposition in multi-levels via DWT of the stator current in a steady state, and additional steps are required to determine the energy associated with each level of decomposition [12, 13]. The proposed energy estimation is used to analyse stator currents when the spectral content is distributed over a wide frequency band. To validate this method, several experiments, including those with a healthy machine, an eccentric machine, and shaft misalignment, are carried out to simulate a variety of failure scenarios and operating settings. The focus of this study is on selecting the appropriate decomposition levels for information extraction corresponding to faults caused by stator currents. We will try to show how the harmonic content caused by mechanical faults is largely influenced by the loading level. A dynamic eccentricity fault of 50 % and a shaft misalignment fault will be discussed and validated using this technique.

2. Wavelet decomposition and energy extraction

The Wavelet Transform WT provides time tracking of frequency harmonics of a continuous temporal signal, the main analysing functions are called wavelets. These functions vary their time-scale coefficients to their frequency to be very narrow at higher frequency and broader at a lower frequency. WT is a powerful means for analysing stationary and transient currents, voltages, and vibration in order to detect the presence of failure. DWT is the discrete version of WT and the most common transform employed in electrical engineering applications, particularly in monitoring systems for detection, localisation, and classification of the power system perturbations in time and frequency domains [13, 17, 18].

The DWT has become an effective tool in digital signal processing. It can be written in the same form as the continuous version, which highlights the close relationship between the continuous and the discrete version of this transform. The DWT is based on a discrete scale and localisation parameters that are power of two (2). The values of dilation and translation factors s and τ are: $s = 2j$, $\tau = k * 2^j$ and $(j, k) \in Z$, respectively. These proprieties are achieved by using a scaling function ϕ that is a wavelet aggregate at scales larger than 1. When the functions $\hat{\psi}(\omega)$ and $\hat{\varphi}(\omega)$ are the Fourier transforms of $\psi(\omega)$ and $\varphi(\omega)$, respectively, it leads to high-frequency resolutions at low frequencies and high-time resolutions at high frequencies, and eliminating the redundant information. The positive frequency, contains information in the interval $[0, \pi]$, and contains information in the interval $[\pi, 2\pi]$. Therefore, the two functions have a complete spectral content of the analysed signal without any overlapping, redundancy, or loss. Two filters, $h(n)$ and $g(n)$, are obtained by the inner product of $(\phi(t), \varphi(t))$ allowing the decomposition of the entire signal into $[0, \pi]$. The filters are given by [19–24]:

$$\begin{cases} h(n) = \left\langle 2^{-l}\phi(2^{-l}t)\phi(t-n)\right\rangle \\ g(n) = \left\langle 2^{-j}\psi(2^{-j}t)\psi(t-n)\right\rangle \end{cases} ., \; j = 0, 1, ... \quad (1)$$

For the purpose of decomposing the signal across the entire allowed frequency range, a mother wavelet can be used. After the multi-level decomposition by l times, we get 2^l frequency bands with the same bandwidth defined according to equation (2).

$$[\frac{(i-l)f_n}{2}, \frac{if_n}{n}], \quad i = 1, 2, ..., 2^l, \qquad (2)$$

where fn is the Nyquist frequency in the ith-frequency band. The mother wavelet decomposes the signal via low-pass filter $h(n)$ and $(2^l - 1)$ band-pass filters $g(n)$ to provide, at each level j, the full information in two frequency bands. A_j is the low-frequency approximation and D_j is the high-frequency detail signal [19]:

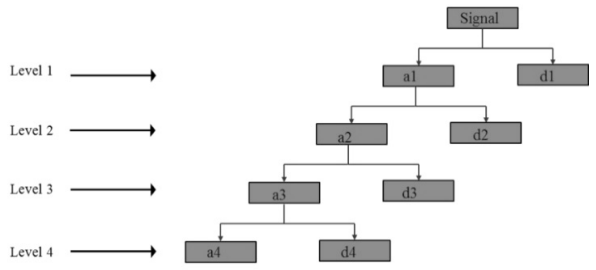

FIGURE 1. Wavelet tree decomposition.

$$\begin{cases} A_j(n) = \sum\limits_k h(k-2n)A_{j-1} \\ D_j(n) = \sum\limits_k g(k-2n)A_{j-1} \end{cases} ., \; n = 0, 1, 2, 3, ..., \tag{3}$$

where $A_0(k)$ is the initial signal. After the multi-level decomposition, the approximation A_j and detail D_j signals will be generated for each node j.

The multi-level decomposition of the stator current was then achieved using the Daubechies *db*8 wavelet. When rotor eccentricity and load misalignment appear in the motor, the information about the fault in the stator current will be included in each frequency band generated by the DWT decomposition process.

The calculation of the vector energy for the approximations in each node allows the construction of a vector data which contain the necessary information about faults over a wide frequency band.

The approximations energy can be computed using the Euclidean norm (or 2-energy) of $A_i(n)$ that has N elements and is defined by:

$$\|EA_i\| = \frac{1}{N}\sqrt{\sum_{k=1}^{N} |A_i(k)|^2} \;\; , \; i = 1, 2, \ldots..N_{ls} \tag{4}$$

Figure 2 shows the estimation of the approximation's energy vector for each node and the corresponding frequency band.

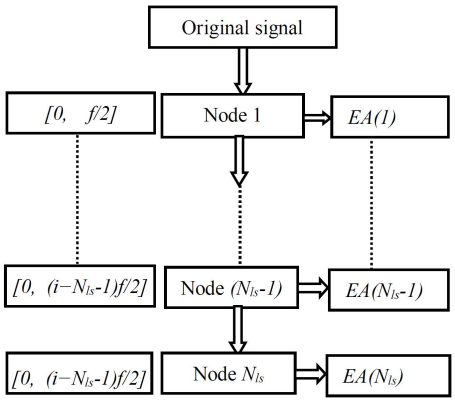

FIGURE 2. Approximations energy estimation steps.

The overall stator current analysis diagram is presented in Figure 3. The different steps are presented, from the stator current acquisition to the estimation of the energy for each level of decomposition.

3. FAULTS DESCRIPTION

In electrical machines, eccentricities are generally generated by the non-constant air-gap distribution. They are the most common faults in induction motors. According to recent studies, mechanical faults represent 50–60 % of the faults in electric motors. About 60 %

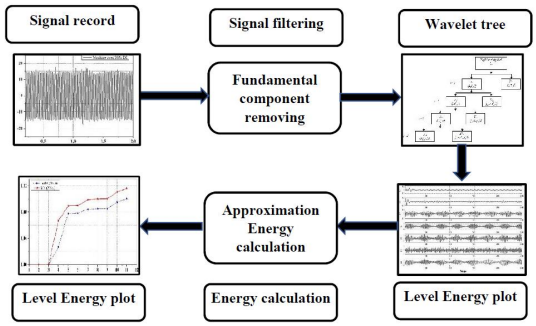

FIGURE 3. Stator current analysis steps.

of mechanical defects are linked to rotor eccentricities. Indeed, the rotor eccentricity is often generated from other defect such as bearing failures or load misalignments. The impact of this fault can be serious; this could even result in a breakdown of the motor due to rotor-to-stator friction [25–27].

Dynamic eccentricity (DE) take place when the rotor axle is not matching the rotation axle and the narrow side of the air-gap rotates at the same speed as the rotor (Figure 4). There are multiple causes of dynamic eccentricity and the most common are manufacturing tolerances, bearing wear, and incorrect manufacture of the machine components. Another source of dynamic eccentricity is the rotation of the rotors at a speed close to the critical speed; it is an important consideration in larger and flexible-shaft machines. In an induction machine, a dynamic eccentricity can be identified by examining the frequency components defined as follows [27–29]:

$$f_{de} = (1 \pm \frac{(1-s)}{p}) f_s, \tag{5}$$

where

f_de : the characteristic frequency of the DE

s : the Slip

f_s : the supply frequency

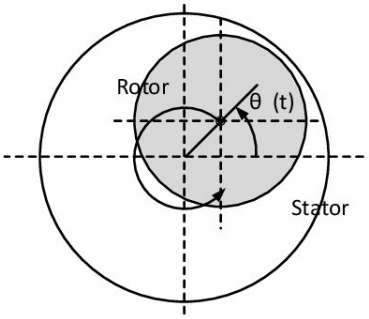

FIGURE 4. Dynamic eccentricity mechanism.

A non-constant air-gap generates a rotating radial force and an Unbalanced Magnetic Pull (UMP) on the rotor and stator due to the interaction of the space harmonic field components with pole pair numbers

differing by one and rotating in the same direction. The dynamic eccentricity may generate vibrations at the supply frequency and at the rotor frequency (f_r), these are given by $2f_r$, $2f_s \pm f_r$ [30]. where f_s is the supply frequency. A misalignment of the coupling is a condition in which the shaft of the drive machine and the driven machine are not on the same centre line (Figure 5). The misalignment can be parallel, angular or both (combined: parallel and angular). It is very difficult to obtain a perfect alignment between two shafts in industrial applications [28, 31].

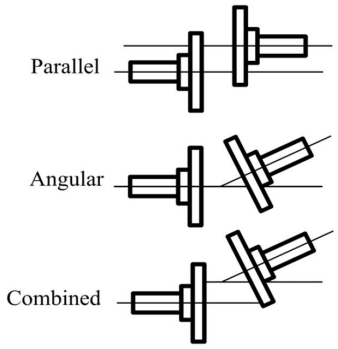

FIGURE 5. Shafts misalignment.

Even if a precise alignment is ensured, it cannot be maintained for a long time due to many external effects such as a disturbance of the base foundation. A shaft misalignment is a commonly encountered problem observed in the large rotor bearing machines and produces significant vibrations. Flexible couplings are commonly employed in industrial production chains to transmit mechanical power between the machine and the driven load. Most couplings transmit electromagnetic torque via an elastomer or a metal spring in order to reduce the vibration within an accepted level of misalignment. Electrical machines manufacturers suggest using the flexible couplings based on thermoplastics as active transmission elements for load aligning by using laser equipment or alignment clocks. The misaligned flexible couplings can transmit torque, producing high vibration levels and may cause damage to the shaft and bearings.

The misalignment induces harmonics in the stator current spectrum at frequencies, this makes it possible to detect these phenomena. However, since similar harmonics are produced by some mechanical faults, their detection and localisation are still a delicate matter when using MCSA. To overcome this limitation, it becomes necessary to identify misalignment faults over a wide band of frequency [4].

The main goal of this paper is to use the DWT approach for the detection of dynamic eccentricity and shaft misalignment in squirrel cage induction motors under various loading conditions, since the frequency components introduced by these faults depend on the load. Their detection and decision can constitute a powerful indicator for the diagnosis. In this work, the obtained approximation signals generated by the multilevel decomposition are used to build an energy vector calculated for each decomposition node. The method allows the detection based on the analysis of the energy of the signals that are amplified by the different faults. This method constitutes an important advantage when compared to the classical methods by analysing the stator current under a wide frequency band and avoiding the tracking of harmonics in a limited band or at predefined frequency.

Parameter	**Value**
Rated power	5.5 kW
Rated Voltage	400 V
Rated line current	10.5 A
Rated speed	1455 rpm
Rated power factor	0.88
DC motor	MS1321
Rated speed	1450 rpm
Rated power	3.9 kW
Rated Voltage	260 V
Rated current	17.6 A

TABLE 1. Characteristics of the 5.5 kW IM and DC load.

4. EXPERIMENTAL SETUP

An experimental analysis of the mechanical faults described previously has been carried out. The experimental setup contains a three-phase squirrel cage induction machine with 4 poles and a rated torque of 36 Nm. The induction motor is coupled to a DC motor to provide the necessary load. The used motors are driven by a variable speed drive (Leroy Somer) working in open loop. The DC motor is connected to a resistor bank via a DC-DC buck converter for controlling the armature current. The principal characteristics of tested machines are given in Table 1.

The experimental setup is illustrated in Figure 6. It consists mainly of an industrial induction motor with its drive loaded by a DC motor. Two induction motors with the same characteristics are tested. The first one is healthy; it will be considered as a reference for the comparison with the faulty one. The second motor is faulty and has a dynamic eccentricity and misalignment. The measurement card contains current sensors LA-55P, voltage sensors LV-25P, tachymeter and torque sensor. A maximum current and voltage of 50 A and 480 V can be achieved respectively.

The acquisition card used is a PCI data card, 16-bit, with a sampling frequency of 200 kHz, and it is installed in a computer and connected to the measuring board via a serial cable. These motors are supplied by the industrial drive and have been tested under three loading level conditions. All the experiments are carried out with the same sampling frequency 26,5 Hz during 10 s recording time. To obtain 50 % of DE, the original ball bearings are replaced by other ball bearings of the same external diameter, but of greater

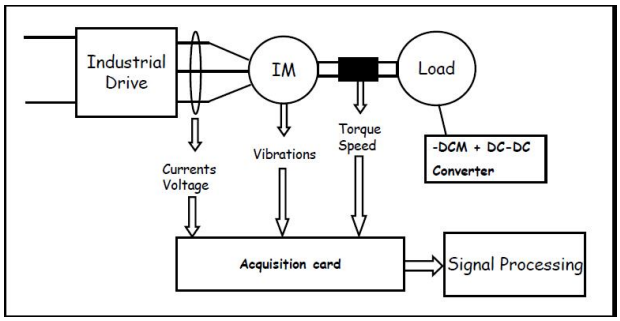

FIGURE 6. Mechanical faults experimental setup.

internal diameter. A 0.2 mm bore offset is introduced. After an aligned positioning of the eccentric rings on the shaft (to guarantee a uniform direction of the eccentricity), we insert the new ball bearings. The introduced air-gap of the machine is considered to be 0.4 mm; 50 % of DE of the rotor compared to the stator (Figure 7).

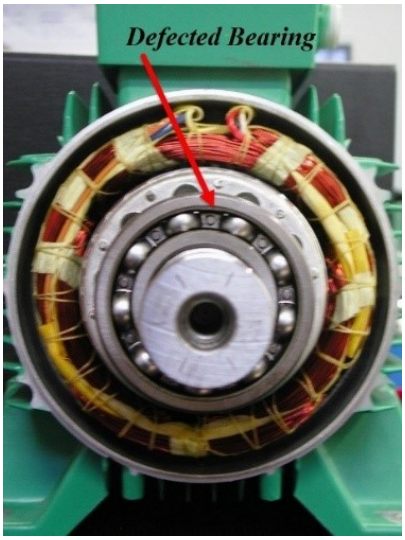

FIGURE 7. Eccentric bearing assembling.

The tests carried out to analyse the DE have been performed on two machines (a healthy machine and another with 50 % of DE) with the principal characteristics shown in Table 1. The sampling frequency of the measured signals was chosen equal to 25.6 KHz. The two machines were tested under three levels of load: 4 Nm, 18 Nm and 29 Nm of the nominal torque. The Figure 8 illustrates the wave form of the recorded stator current for the machine with the dynamic eccentricity.

In order to study a more realistic mechanical fault, a small misalignment of the load shaft is introduced under different loads (4 Nm, 18 Nm and 29 Nm). The Figure 9 shows the measurement of the misalignment degree.

For the misalignment faults, the same mechanical setup and signal processing steps as above are used for recording and analysing the stator current under the same loading conditions

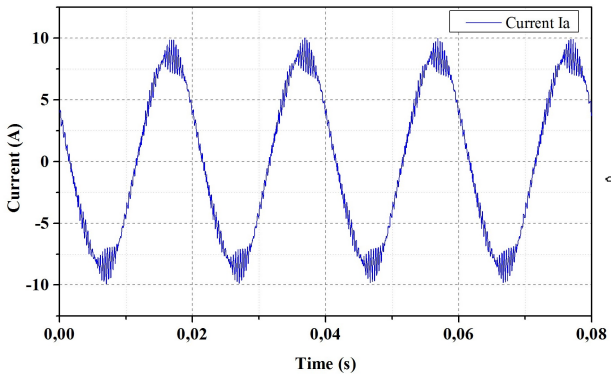

FIGURE 8. Recorded stator current with dynamic eccentricity.

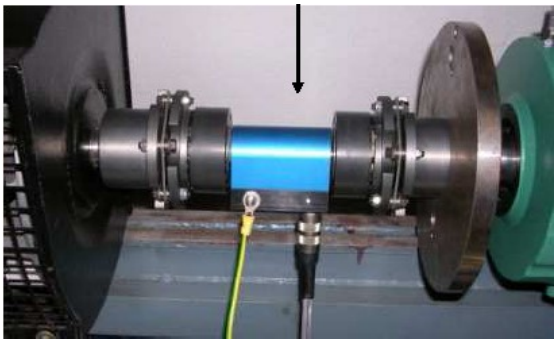

FIGURE 9. Misalignment degree measurement.

4.1. Stator current decomposition

The mother wavelets "db8" are used to decompose the stator current for each machine. The decomposition in multi-level requires some consideration in order to obtain a good approximation and detail signals.

4.2. Stator current filtering

Among the methods used in this paper, the fundamental component of the stator current has been removed before the signal goes through the multi-level decomposition process by DWT. This procedure amplifies the small harmonics induced by the faults.

4.3. Optimal level calculation

The required number of decompositions N_{ls} is linked to the acquisition conditions, such as the sampling frequency f and the supply frequency. The necessary level N_{ls} is chosen to obtain a high-level signal (approximation) with a highest frequency along which the faults harmonics are located. The minimum levels of decomposition needs an approximation signal (A_{nf}) with the upper limit of the frequency band being less than the fundamental frequency. This limit is expressed by the following condition [19].

$$2^{-(L_{ls}+1)} f_s < f \tag{6}$$

From this requirement, the successive decomposition of the approximation signals can be limited to level N_{ls} that is given by:

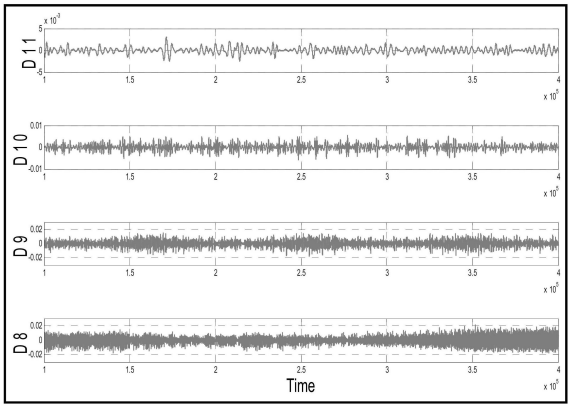

(A). Healthy motor.

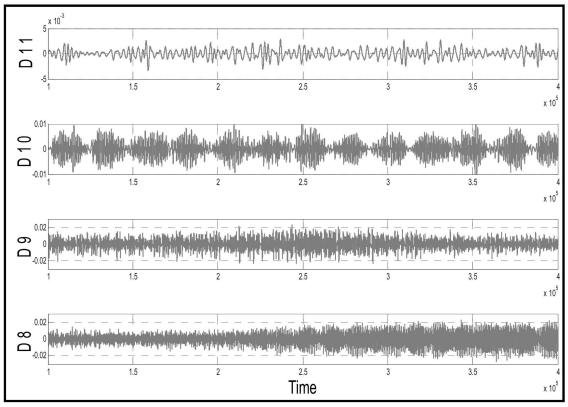

(B). Eccentric motor.

FIGURE 10. First 4 details signals for (A) symmetric motor and (B) eccentric motor.

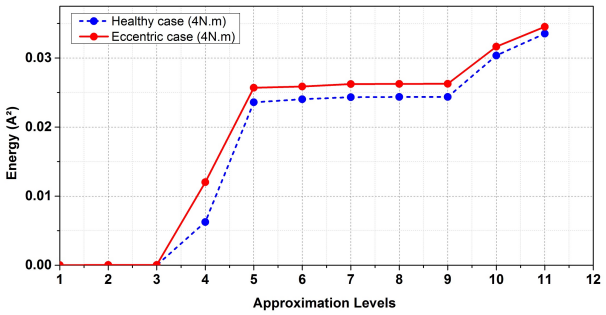

(A). 4 Nm

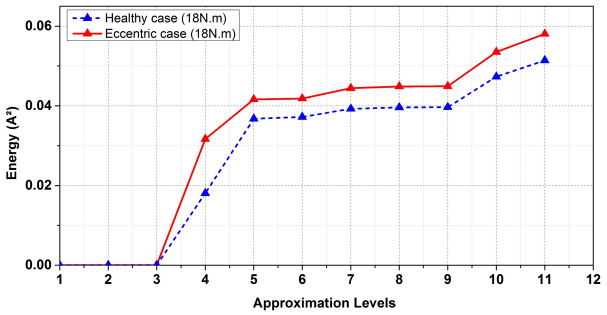

(B). 18 Nm

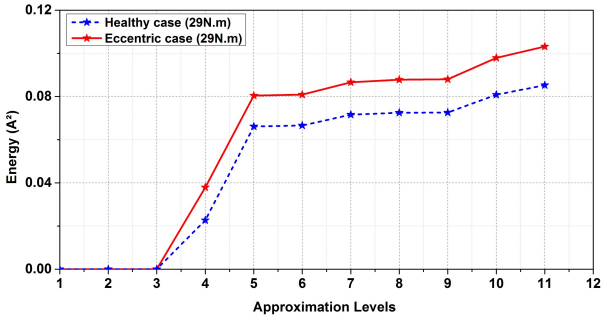

(C). 29 Nm

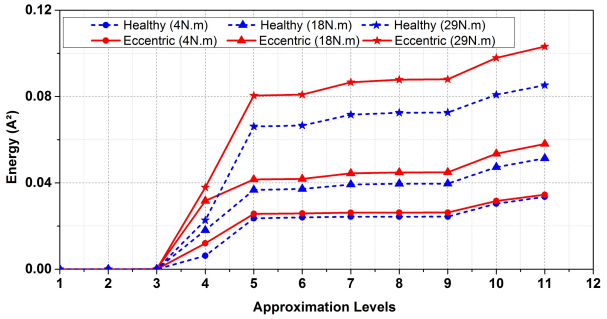

(D). all cases

FIGURE 11. Estimated nodes energy for eccentricity fault under (A) load = 4 Nm, (B) load = 18 Nm, (C) load = 29 Nm and (D) all cases.

$$N_{ls} = \text{int}\left(\frac{\log(f_s/f)}{\log(2)}\right). \tag{7}$$

For this technique, an additional decomposition of the stator current should be carried out so that the frequency band [0–f] is divided into several bands. Generally, two extra levels of decomposition $N_{ls} + 2$ will be suitable [19].

According to the suitable level, the different frequency bands are given in Table 2.

The Figure 10 compares the details obtained from DWT of a steady state stator current for a symmetric machine and for the eccentric machine with 50 $ of DE under a load 4 Nm. The purpose of this comparison is to demonstrate that when the harmonics are introduced by the dynamic eccentricity, the DWT analysis can distinguish clearly between the faults when present.

5. RESULTS AND DISCUSSION

5.1. DYNAMIC ECCENTRICITY

For the dynamic eccentricity fault, the energy vector is calculated for 11 levels with 3 loading levels. Figure 11 shows the plot of vector $\|EA_i\|$ for the three loading levels.

The analysis of the three figures shows an increase in energies for eccentric cases starting at level 3, which corresponds to the frequency band [0–3312.5Hz]. We also see that the deviation is important as a function

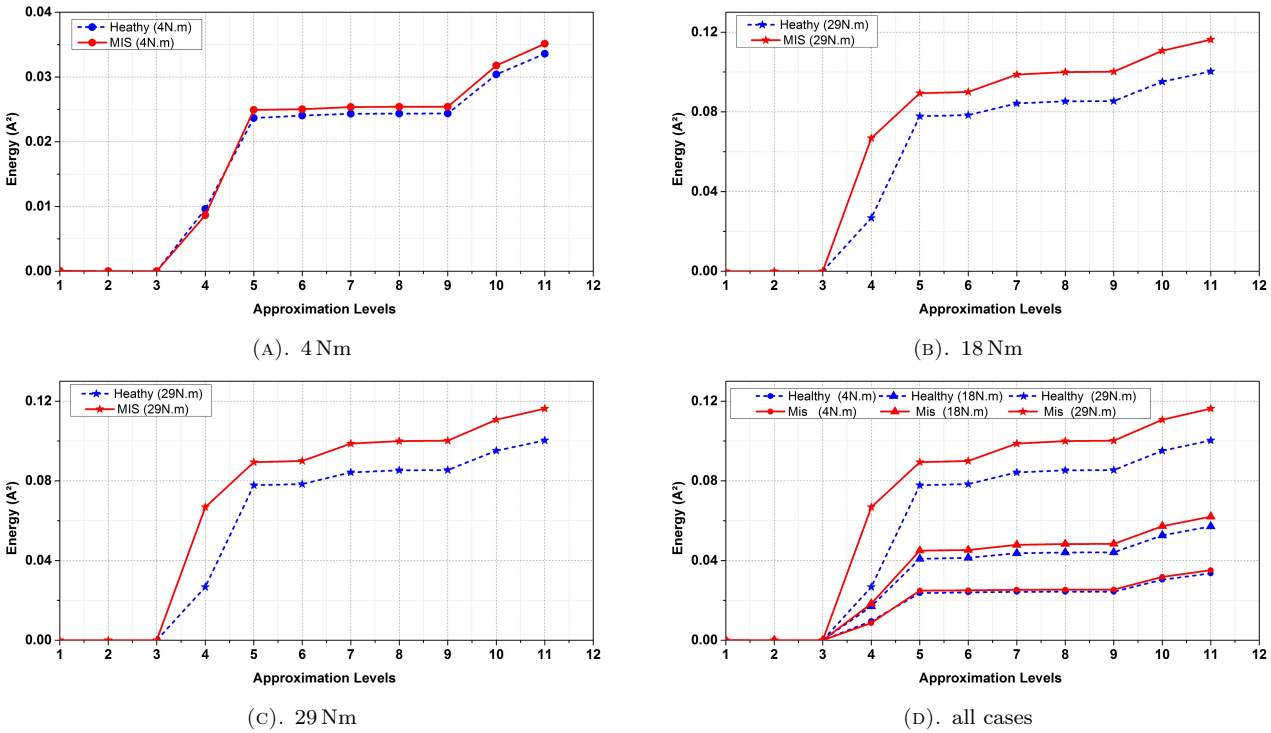

(A). 4 Nm (B). 18 Nm

(C). 29 Nm (D). all cases

FIGURE 12. Estimated nodes energy for misalignment fault under (A) load = 4 Nm, (B) load = 18 Nm, (C) load = 29 Nm and (D) all cases.

Level	A_i	**Band [Hz]**	D_i	**Band [Hz]**
J=1	A1	0-13250	D1	13250-26500
J=2	A2	0-6625	D2	6625-13250
J=3	A3	0-3312.5	D3	3312.5-6625
J=4	A4	0-1656.2	D4	1656.25-3312.5
J=5	A5	0-828.12	D5	828.12-1656.25
J=6	A6	0-414	D6	414-828.125
J=7	A7	0-207	D7	207-414
J=8	A8	0-103.5	D8	103.5-207
J=9	A9	0-51.75	D9	51.75-103.5
J=10	A10	0-25.87	D10	25.875-51.75
J=11	A11	0-12.94	D11	12.94-25.87

TABLE 2. Details and approximation bands for N_{ls}.

of the loading, even at high frequencies. These results show that eccentricity can be detected in the frequency band [0–4000 Hz] with useful information on the faults concentrated in the low frequencies and gradually decreasing in the high frequencies.

5.2. MISALIGNMENT

For the misalignment fault, the energy vector is also calculated for 11 levels with 3 loading levels. Figure 12 shows the plot of vector $\|EA_i\|$ for the three loading levels.

Similarly to the an eccentricity fault results, the figure analysis shows an increase in energies for misalignment cases beginning at level 3, which corresponds to the frequency band [0–3312.5 Hz].These results show that a misalignment fault can be detected in the frequency band [0–4000 Hz] with useful information concentrated in low frequencies and gradually decreasing in high frequencies. The curves obtained for mechanical faults show that the load has an important role in the detection process, and it is recommended to carry out the diagnostic operation under full loading conditions in order to increase the separation between the healthy and the defective machine.

A comparison between energies for healthy and defective machines under various loads is performed in order to show the energy deviation as a function of the load level. Table 3 displays numerical values for the energy deviation for various machine loadings. Figure 13 shows the graphical plot of this deviation for both cases of eccentric and misaligned machines.

The plot of the difference in energies of the nodes showed a large deviation when the load increases, precise for the fault of the dynamic eccentricity and less accurate for the fault of misalignment. This result is critical to consider when performing any diagnostic procedure. It is obvious that the diagnosis at high load is more precise than that at low load.

6. CONCLUSION

In this work, a study was carried out to diagnose electrical and mechanical faults under different loading levels in a squirrel cage induction machine. The main aim is to find an effective method to decide whether the machine is faulty or not. The proposed method is a multi-resolution analysis based on the Discrete Wavelet Transform (DWT). Unlike traditional methods based on the Fast Fourier Transform (FFT),

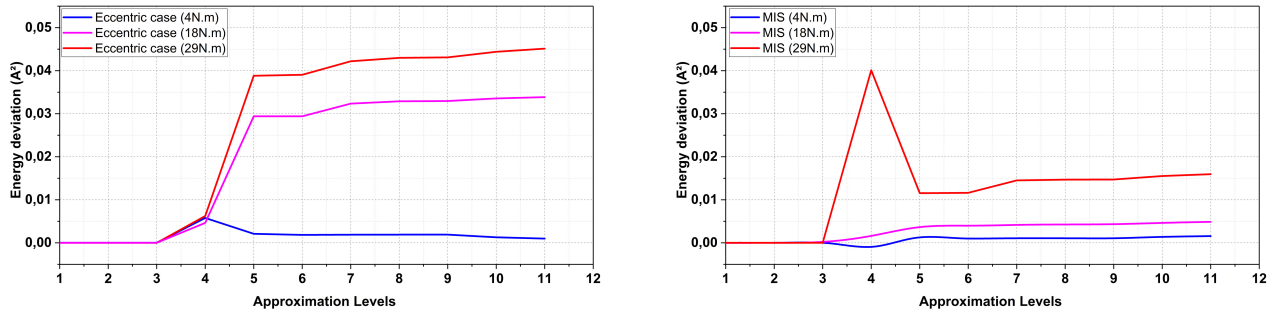

(A). Eccentric case.

(B). Misalignment case.

FIGURE 13. Energy deviation between healthy and faulty cases, (A) Eccentric case, (B) Misalignment case.

	Eccentric case			Misalignment case		
	4 Nm	18 Nm	29 Nm	4 Nm	18 Nm	29 Nm
Level 1	1.98E-05	-9.05E-06	-4.68E-06	6.09E-06	-2.99E-05	3.41E-06
Level 2	2.34E-05	-1.34E-05	-6.62E-06	4.49E-07	-1.81E-05	3.85E-06
Level 3	3.20E-05	-1.03E-05	-7.24E-06	4.20E-08	-1.66E-05	3.51E-06
Level 4	0.00578	0.00623	0.00464	-9.58E-04	0.00138	0.04011
Level 5	0.0021	0.03883	0.0294	0.00126	0.00416	0.01154
Level 6	0.00184	0.03904	0.0294	9.89E-04	0.00387	0.01162
Level 7	0.00189	0.04219	0.03235	0.00104	0.00421	0.01451
Level 8	0.0019	0.04299	0.03288	0.00105	0.00427	0.01469
Level 9	0.0019	0.04309	0.03295	0.00105	0.00427	0.01471
Level 10	0.00129	0.0444	0.03355	0.00137	0.00465	0.01553
Level 11	9.82E-04	0.04512	0.03386	1.55E-03	0.00487	0.01595

TABLE 3. Energy deviation between healthy and faulty machines.

the DWT method allows searching information for related to faults over wide frequency bands and to avoid tracking the fault indicators related to predefined frequencies. The results obtained by applying the proposed method on the different faults show the efficiency and the precision of detection and separation between healthy and defective machines. Moreover, the results show that the load applied during the acquisition process has an important role in the detection of mechanical faults.

We have also shown in this work that the diagnosis of faults at a high load is strongly recommended to reveal the different harmonics related to the fault. The proposed method in this paper also shows that the spectral content caused by the mechanical defects like eccentricity and misalignment is more important at high frequencies than at low frequencies.

REFERENCES

[1] O. E. Hassan, M. Amer, A. K. Abdelsalam, B. W. Williams. Induction motor broken rotor bar fault detection techniques based on fault signature analysis – a review. *IET Electric Power Applications* **12**(7):895–907, 2018. https://doi.org/10.1049/iet-epa.2018.0054

[2] S. K. Ramu, G. C. R. Irudayaraj, S. Subramani, U. Subramaniam. Broken rotor bar fault detection using hilbert transform and neural networks applied to direct torque control of induction motor drive. *IET Power Electronics* **13**(15):3328–3338, 2020. https://doi.org/10.1049/iet-pel.2019.1543

[3] K. Gyftakis, P. Panagiotou, D. Spyrakis. Detection of simultaneous mechanical faults in 6 kV pumping induction motors using combined MCSA and stray flux methods. *IET Electric Power Applications* pp. 1–8, 2020 [E-First]. https://doi.org/10.1049/iet-epa.2020.0099

[4] H. S. Gerçekcıoğlu, M. Akar. Instantaneous power signature analysis for misalignment fault diagnosis in 3-phased induction motors. In *2018 26th Signal Processing and Communications Applications Conference (SIU)*, pp. 1–4. IEEE. https://doi.org/10.1109/SIU.2018.8404303

[5] R. A. Ayon-Sicaeros, E. Cabal-Yepez, L. M. Ledesma-Carrillo, G. Hernandez-Gomez. Broken-rotor-bar detection through STFT and windowing functions. In *2019 IEEE Sensors Applications Symposium (SAS)*, pp. 1–5. IEEE. https://doi.org/10.1109/SAS.2019.8706086

[6] P. Lombard, V. Fireteanu, A.-I. Constantin. Influences on the electromagnetic torque and rotor force of different faults in squirrel-cage induction motors. *International Journal of Applied Electromagnetics and Mechanics* **59**(3):805–815, 2019. https://doi.org/10.3233/jae-171136

[7] A. Kucuker, M. Bayrak. Detection of mechanical imbalances of induction motors with instantaneous power signature analysis. *Journal of Electrical Engineering and Technology* **8**(5):1116–1121, 2013. https://doi.org/10.5370/jeet.2013.8.5.1116

[8] W. T. Thomson. Vibration monitoring of induction motors and case histories on shaft misalignment and soft foot. In *Vibration Monitoring of Induction Motors*, pp. 1–46. Cambridge University Press, 2020. https://doi.org/10.1017/9781108784887.002

[9] T. Goktas, M. Arkan, M. S. Mamis, B. Akin. Separation of induction motor rotor faults and low frequency load oscillations through the radial leakage flux. In *2017 IEEE Energy Conversion Congress and Exposition (ECCE)*, pp. 3165–3170. IEEE, 2017. https://doi.org/10.1109/ecce.2017.8096576

[10] C. Prakash, R. K. Saini. IoT-based monitoring and controlling of crop field and induction motor protection from voltage fluctuation. *Agricultural Journal* **15**(4):49–56, 2020. https://doi.org/10.36478/aj.2020.49.56

[11] R. R. Schoen, T. G. Habetler. Evaluation and implementation of a system to eliminate arbitrary load effects in current-based monitoring of induction machines. In *IAS '96. Conference Record of the 1996 IEEE Industry Applications Conference Thirty-First IAS Annual Meeting*, vol. 1, pp. 671–678. IEEE. https://doi.org/10.1109/ias.1996.557108

[12] M. Singh, A. G. Shaik. Broken rotor bar fault diagnosis of a three-phase induction motor using discrete wavelet transform. In *2019 IEEE PES GTD Grand International Conference and Exposition Asia (GTD Asia)*, pp. 13–17. IEEE, 2019. https://doi.org/10.1109/gtdasia.2019.8715925

[13] O. Bolshunova, A. Kamyshian, A. Bolshunov. Diagnostics of career dump truck traction induction motors technical condition using wavelet analysis. In *2016 Dynamics of Systems, Mechanisms and Machines (Dynamics)*, pp. 1–4. IEEE. https://doi.org/10.1109/Dynamics.2016.7818988

[14] M. Z. Ali, M. N. S. K. Shabbir, S. M. K. Zaman, X. Liang. Single- and multi-fault diagnosis using machine learning for variable frequency drive-fed induction motors. *IEEE Transactions on Industry Applications* **56**(3):2324–2337, 2020. https://doi.org/10.1109/tia.2020.2974151

[15] M. Z. Ali, M. N. S. K. Shabbir, X. Liang, et al. Machine learning-based fault diagnosis for single- and multi-faults in induction motors using measured stator currents and vibration signals. *IEEE Transactions on Industry Applications* **55**(3):2378–2391, 2019. https://doi.org/10.1109/tia.2019.2895797

[16] F. Wu, Y. Hao, J. Zhao, Y. Liu. Current similarity based open-circuit fault diagnosis for induction motor drives with discrete wavelet transform. *Microelectronics Reliability* **75**:309–316, 2017. https://doi.org/10.1016/j.microrel.2017.05.036

[17] T. K. Sarkar, C. Su, R. Adve, et al. A tutorial on wavelets from an electrical engineering perspective. I. Discrete wavelet techniques. *IEEE Antennas and Propagation Magazine* **40**(5):49–68, 1998. https://doi.org/10.1109/74.735965

[18] B. A. Vinayak, K. A. Anand, G. Jagadanand. Wavelet-based real-time stator fault detection of inverter-fed induction motor. *IET Electric Power Applications* **14**(1):82–90, 2020. https://doi.org/10.1049/iet-epa.2019.0273

[19] A. Bouzida, O. Touhami, R. Ibtiouen, et al. Fault diagnosis in industrial induction machines through discrete wavelet transform. *IEEE Transactions on Industrial Electronics* **58**(9):4385–4395, 2010. https://doi.org/10.1109/TIE.2010.2095391

[20] T. Ameid, A. Menacer, H. Talhaoui, Y. Azzoug. Discrete wavelet transform and energy eigen value for rotor bars fault detection in variable speed field-oriented control of induction motor drive. *ISA Transactions* **79**:217–231, 2018. https://doi.org/10.1016/j.isatra.2018.04.019

[21] N. R. Alham, R. M. Utomo, D. A. Asfani, et al. Detection of unbalanced voltage supply and static eccentricity on three-phase induction motor using discrete wavelet transform. In *2020 12th International Conference on Information Technology and Electrical Engineering (ICITEE)*, pp. 269–274. IEEE. https://doi.org/10.1109/ICITEE49829.2020.9271691

[22] M. A. Mohamed, A.-A. A. Mohamed, M. Abdel-Nasser, et al. Induction motor broken rotor bar faults diagnosis using ANFIS-based DWT. *International Journal of Modelling and Simulation* **41**(3):220–233, 2021. https://doi.org/10.1080/02286203.2019.1708173

[23] B. Belkacemi, S. Saad, Z. Ghemari, et al. Detection of induction motor improper bearing lubrication by discrete wavelet transforms (DWT) decomposition. *Instrumentation Mesure Métrolo* **19**(5):347–354, 2020. https://doi.org/10.18280/i2m.190504

[24] I. Chouidira, D. Khodja, S. Chakroune. Continuous wavelet technique for detection of broken bar faults in induction machine. *Traitement du Signal* **36**(2):171–176, 2019. https://doi.org/10.18280/ts.360207

[25] K. Tian, T. Zhang, Y. Ai, W. Zhang. Induction motors dynamic eccentricity fault diagnosis based on the combined use of WPD and EMD-simulation study. *Applied Sciences* **8**(10):1709, 2018. https://doi.org/10.3390/app8101709

[26] Nikhil, L. Mathew, A. Sharma. Various indices for diagnosis of air-gap eccentricity fault in induction motor – a review. *IOP Conference Series: Materials Science and Engineering* **331**:012032, 2018. https://doi.org/10.1088/1757-899x/331/1/012032

[27] G. Mirzaeva, K. I. Saad. Advanced diagnosis of rotor faults and eccentricity in induction motors based on internal flux measurement. *IEEE Transactions on Industry Applications* **54**(3):2981–2991, 2018. https://doi.org/10.1109/TIA.2018.2805730

[28] A. Ortiz, J. Garrido, Q. Hernandez-Escobedo, B. Escobedo-Trujillo. Detection of misalignment in motor via transient current signature analysis. In *2019 IEEE International Conference on Engineering Veracruz (ICEV)*, vol. 1, pp. 1–5. IEEE. https://doi.org/10.1109/ICEV.2019.8920719

[29] A. F. Aimer, A. H. Boudinar, M. E. A. Khodja, et al. Monitoring and fault diagnosis of induction motors mechanical faults using a modified auto-regressive approach. In *Advanced Control Engineering Methods in Electrical Engineering Systems*, pp. 390–410. Springer International Publishing, 2018. https://doi.org/10.1007/978-3-319-97816-1_30

[30] R. S. C. Pal, A. R. Mohanty. A simplified dynamical model of mixed eccentricity fault in a three-phase induction motor. *IEEE Transactions on Industrial Electronics* **68**(5):4341–4350, 2020. https://doi.org/10.1109/TIE.2020.2987274

[31] S. Prainetr, S. Tunyasrirut, S. Wangnipparnto. Testing and analysis fault of induction motor for case study misalignment installation using current signal with energy coefficient. *World Electric Vehicle Journal* **12**(1):37, 2021. https://doi.org/10.3390/wevj12010037

ESTIMATION OF STRESSES IN A MASSIVE GRANITE USING LASER ULTRA-SONIC TESTING AND STRESS MEMORY EFFECT

Ondřej Kašpar[a], Alexander Kravcov[b,*], Jiří Štoller[c], Petr Kubeček[b], Radovan Vnuk[b], Zbyněk Zušťák[b]

[a] *Charles University in Prague, Faculty of Science, Engineering Geology and Applied Geophysics, Albertov 6, 128 43 Prague 2, Czech Republic*

[b] *Czech Technical University in Prague, Faculty of Civil Engineering, Department of Construction Technology, Thákurova 7, 160 00 Prague, Czech Republic*

[c] *University of Defence in Brno, Faculty of Military Technologies, Kounicova 65, 662 10 Brno, Czech Republic*

[*] corresponding author: kravtale@fsv.cvut.cz

Abstract. This paper addresses in-situ stress-estimation methods based on the Kaiser effect. The physical and mechanical properties of granite, diorite, and granodiorite samples selected at different depth intervals of the core obtained from a wellbore were examined. The ultimate uniaxial compressive strength, modulus of elasticity, and Poisson's ratio of the rock samples were determined using presses and strain gauges. Also, local longitudinal and shear wave velocities were measured using a high-accuracy laser-ultrasonic system with a view to assessing the structure of the samples. Based on the resulting elastic wave velocity maps, samples with no obvious discontinuities were chosen. These undisturbed samples were subjected to uniaxial compression and their acoustic emission was simultaneously measured. In-situ stresses were estimated from the results of the interpretation of acoustic emission measurements. The experimental in-situ stresses were compared with the results of a numerical simulation. The ratio of the estimated in-situ stresses to the calculated ones is within the range from 0.81 to 1.11. This means that the laser ultrasonic and acoustic emission methods make it possible to effectively estimate in-situ stresses in a rock mass and assess the degree of rock mass damage.

Keywords: Rock cores, acoustic emission, laser ultrasonic method, structure, stress state, rocks, Kaiser effect.

1. Introduction

Rocks are heterogeneous media that contain defects at different scales; this may cause crack initiation even at light loads [1]. That is why mining operations should be preceded by a detailed study of the geological and geotechnical conditions and analysis of the stress state of the rock mass [2, 3]. Note that one of the main methods for studying the stress state is numerical simulation [4–6]. This is due to the fact that there are no direct methods for measuring in-situ stresses in a rock mass. However, the results of a numerical simulation need to be verified, which is usually done with indirect methods. These are borehole methods, such as hydrofracturing, borehole stress relief, analysis of the erosion of the walls of boreholes, as well as methods for estimating in-situ stresses using core samples (strain recovery analyses, core disking, and acoustic emission testing based on the Kaiser effect). Also, there are methods for stress control in rock outcrops (rock stress relief through the use of hydraulic pads and slots) and analyses of large-scale geological structures (analyses of focal mechanisms of earthquakes and shear displacements) [7–9]. Each of these methods works at a certain scale, which depends on the volume of the rock mass examined. For example, the acoustic methods require the volume of the rock sample to be in the order of 10-3 m^3. On the recommendation of the International Society for Rock Mechanics (ISRM) [10], two downhole methods have been widely adopted: hydraulic fracturing (HF) and complete stress relief. However, these methods are quite complicated and very costly; therefore, alternative methods for determining in-situ stresses are required.

One of the optimal methods for studying in-situ stresses in a rock mass is the method of acoustic emission (AE) [11–14] based on the Kaiser effect [15, 16]. Importantly, this method does not require high-accuracy deformation measurements.

The Kaiser effect describes the phenomenon that repeated loading cycles cause the level of AE signals decrease up to their complete absence until the level of the previously applied load is exceeded [17, 18]. A sharp increase is observed when approaching the previously achieved maximum value of load [12]. Therefore, the repeated loading of samples recovered from different depths makes it possible to estimate the respective in-situ stresses from a sharp increase in the acoustic emission [17, 18]. For this purpose, the Felicity ratio is introduced in [17] and [18], which is the ratio of the load at which acoustic emission (AE) pulses reappear to the maximum load of the previous

load cycle. This ratio can be either greater than 1 or less, depending on the structural and textural features of rock samples, the directions of the principal stresses in the rock mass and other parameters [19–21]. In work [22], data on the seismic wave velocities are used to estimate Young's modulus and Poisson's ratio, in [23], the damage characterisations of granites were studied by a combination of AE and ultrasonic transmission methods under a quasi-static uniaxial compression test. Mechanical characteristics and failure prediction of cement mortar with a sandwich structure was investigated in [24]. In studies [25–29], acoustic emission is used for understanding the mechanical properties of materials.

The value of the Felicity ratio changes in response to an increase in the time interval between loading cycles, which may make the effect less distinct. The duration of stress memory also depends on the rock type, the loading regime in successive cycles, and the effect of other factors (heating and moistening). Moreover, some rocks retain information on the experienced mechanical stresses for many months, or even years. That is why it is important to study and identify patterns of AE activity inside one type of rocks.

In this study, we investigate if it is possible to estimate in-situ stresses in a granite mass using acoustic emission observed during uniaxial compression of core samples preliminarily examined in structural terms using laser ultrasonic methods.

2. Materials and methods

2.1. Materials

To assess the possibility of using the method of acoustic emission when studying the stress-strain state of a rock mass, granite samples taken from a core sample while drilling a well in the crystalline massif from depths from 70 m to 400 m were studied.

Sample PB1-11 (depth 95.5 m) is grey, heterogeneous, fine-to-medium-grained, dense, massive granodiorite containing inclusions of light-coloured minerals and thin long healed cracks running through the sample;

Sample PB1-32 (depth 95.5 m) is dark pink with a greyish tinge, medium-to-coarse-grained, dense, massive granite interspersed with dark-coloured minerals and thin cracks no more than 1.5 cm long in places;

Sample PB1-56 (depth 230.2 m) is dark pink, heterogeneous, fine-to-medium-grained, dense, massive granite with a large number of inclusions of dark-coloured minerals (> 20 %) and occasional inclusions of mica; no visible cracks are present;

Sample PB1-80 (depth 302.0 m) is light pink with a greyish tinge, fine-to-medium-grained, dense, massive granite interspersed with inclusions of biotite (no more than 5 %); solitary thin cracks no more than 1 cm long are present;

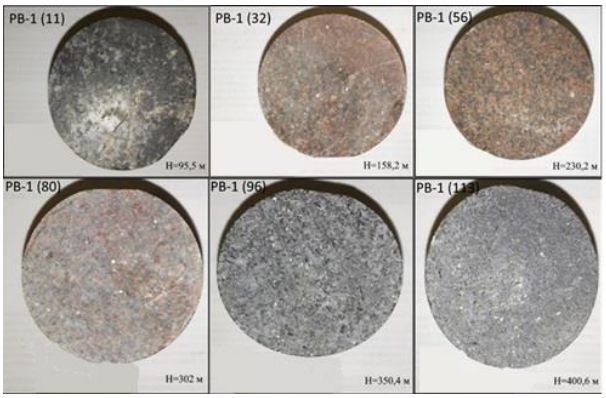

Figure 1. Samples of granite from crystalline massif.

Sample PB1-96 (depth 350.4 m) is dark grey, medium-to-fine-grained, dense, massive diorite interspersed with dark-coloured minerals and inclusions of mica (about 5 %); no visible cracks are present; and

Sample PB1-113 (depth 400.6 m) is dark grey, fine-grained, dense, massive diorite interspersed with dark-coloured minerals and inclusions of mica (about 5-7 %); no visible cracks are present.

Figure 1 shows six granite samples recovered from different depths.

Cylindrical specimens about 10 cm long and about 6 cm in diameter were prepared from these samples. The volume V and density ρ of the specimens were determined.

According to the research, it was found that granodiorites of fine-grained structure, dense and massive, with healed cracks noted (according to sample PB1-11), belong to the migmatite-plagiogranite formation. They are composed of plagioclase, quartz, and biotite in variable amounts – hornblende, epidote, microcline. The structure of the rock shows elements of gneiss and taxite appearance and without metallogenic prospects.

One typical photograph of granite is presented in Figure 2 (No. 2). The samples are presented slightly different in composition, structure (PB1-32 – coarse-medium-grained, PB1-56 and 80 – fine-medium-grained) and patterns of relationship with the rocks of the enclosing frame by species and varieties. Unlike granodiorites, they are two-feldspar rocks with higher silicic acidity and potassium alkalinity.

There are two pictures of diorites (No. 3 – medium-grained and No. 4 – fine-grained) – these samples include plagioclase, hornblende, biotite, as well as apatite, garnet, epidote, chlorite, ore (magnetite, sulphides) in the smallest proportions. Texturally dense, massive, structurally intact.

2.2. Ultrasonic measurements

First, it was necessary to select specimens without long internal cracks which could relieve the stress the specimens experienced in situ; in that case, information

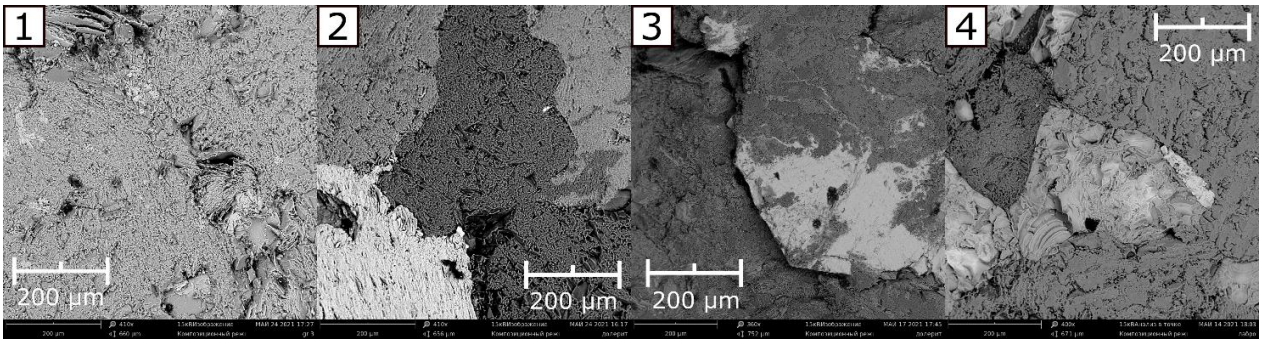

FIGURE 2. Results of microscopic study of characteristic polished sections of each sample of rocks – grano-diorite (No. 1 – PB1-11), granite (No. 2 – PB1-32 / 56/80) and diorites (No. 3 and 4 – PB1-113 and PB1-96) using a Phenom ProX scanning electron microscope.

about these stresses may get lost. To check the "homogeneity" of the specimens, they were scanned using a laser-ultrasonic flaw detector operating in an automatic pulse-echo mode. Figure 3 shows a schematic diagram of scanning. A laser optoacoustic transducer excites a short powerful longitudinal wave pulse. At the transducer-specimen interface, the longitudinal wave is partially converted into shear wave. Both waves are reflected from the diametrically opposite generatrix of the specimen and recorded by a broadband piezoelectric transducer (Figure 3). Their velocities are calculated from the time delay of the waves for a given sample diameter. The measurement error of elastic wave velocities was 0.2 % [21]. Scanning was carried out along the generatrix with a step of 1 cm. Longitudinal wave velocity maps produced using the MatLab software were used for a visual inspection of the specimens to find out if there are large-scale defects such as cracks/pores larger than 5 mm in size. Also, the dynamic Young's modulus E_d and shear modulus G, and Poisson's ratio ν were calculated from the velocities using the formula [21]:

$$E_d = \rho \cdot V_p^2 \cdot \left[3 - \frac{1}{\chi^{-1}}\right], \tag{1}$$

$$G = \rho \cdot V_s^2, \tag{2}$$

$$\nu = \frac{\chi^{-2}}{2 \cdot (\chi^{-1})}, \tag{3}$$

where G is the shear modulus, ρ is the density, and $\chi = (\frac{\nu_p}{\nu_s})^2$ is the square of the ratio of longitudinal wave velocity to shear wave velocity.

2.3. MECHANICAL TESTING

The physical and mechanical properties of the specimens (ultimate uniaxial compressive strength R_c, static modulus of elasticity E, and Poisson's ratio ν) were determined with the use of TP-1-1500 press with

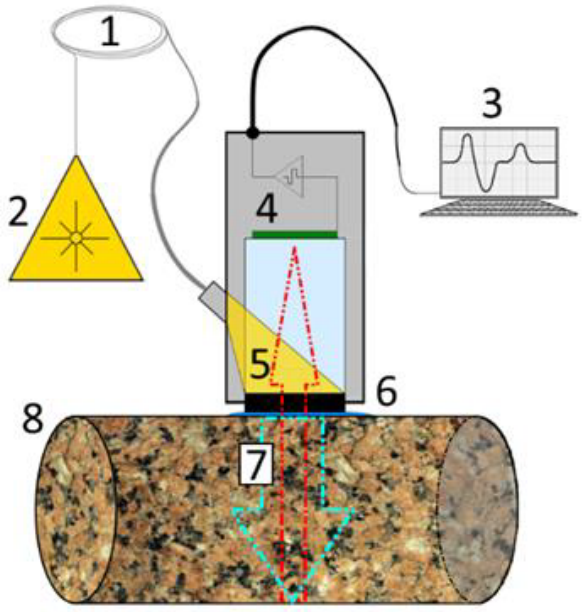

FIGURE 3. Schematic diagram of measurement of elastic wave velocities using laser ultrasonic flaw detector: optical cable (1), laser (2), computer (3), detector (4), laser radiation (5), optoacoustic generator (6), pulses (7), granite specimen (8).

a maximum load of 1500 kN and a tensometric complex consisting of an LTR crate system and ACTEST-OEM software (modules LTR 212M-2 and LTR-EU-2-5). The press and the tensometric complex were synchronised to stress recording. Then, longitudinal and lateral compressive strains were measured as the specimens were subjected to load changing from 5 % to 50 % of the ultimate compressive strength.

2.4. ACOUSTIC EMISSION MEASUREMENTS

The memory effect was studied with a SDS 1008 acoustic emission monitoring system and Maestro 1.2.2 software for data processing. The cumulative AE count Nand acoustic emission activity C_Σ were analysed [1].

№	h_{abb} [m]	h [cm]	d [cm]	m [g]	V [cm^3]	ρ [g cm^{-3}]	V_p [m s^{-1}]	V_S [m s^{-1}]	ν	E [GPa]	R_c [MPa]
1	74,6	9,83	6,26	864,19	308,2	2,78	6018	3774	0,21	102	51
2	95,5	9,99	6,3	881,03	315,2	2,76	5490	2998	0,22	72	94
3	150	10,31	6,3	847,48	325,3	2,61	5253	3096	0,23	72	158
4	158,2	10,19	6,3	833,13	321,5	2,59	5673	3067	0,22	84	150
5	201,2	10,24	6,29	839,46	322,1	2,61	5523	3106	0,27	80	191
6	212,2	9,94	6,29	823,75	313,6	2,63	5696	3443	0,21	85	195
7	230,2	11,74	6,3	908,62	370,4	2,57	6485	3781	0,24	103	195
8	260	10,43	6,26	853,73	326	2,62	6052	3507	0,25	96	146
9	302	10,31	6,3	850,54	326,3	2,61	5627	3124	0,28	83	175
10	350,4	10,16	6,28	925,96	319,6	2,85	5971	3467	0,25	103	116
11	400,6	10,31	6,28	925,8	326,3	2,78	5764	3044	0,31	94	149

Table 1. Physical and mechanical properties of specimens.

3. Results

The physical and mechanical properties of the specimens are shown in Table 1.

According to Table 1, the specimens are hard; the highest values of rock skeletal density are typical of granodiorite and diorite ($\rho = 2.81$–$2.90\,\mathrm{g\,cm^{-3}}$) unit, the density of granite specimens (ρ) varies from 2.57 to $2.63\,\mathrm{g\,cm^{-3}}$; the dynamic modulus of elasticity varies from 72 to 103 GPa. The hardest granite is found in the middle of the analysed depth interval (from 200 to 230 m).

The specimens were subjected to uniaxial compression and their acoustic emission was simultaneously recorded.

The rocks in the massif were in stress state, so the goal of acoustic emission testing was to estimate in-situ stresses and compare them with the results of a numerical simulation. However, since available archive materials do not have the level of detail that is required for a numerical simulation, the vertical stresses in the rock mass were calculated under the assumption that rock stress changes with depth as a result of geostatic load, according to which the expression for vertical stresses is as follows

$$\sigma = \rho\, g\, h, \tag{4}$$

where h_{abb} is the depth. Accordingly, horizontal stresses can be estimated in terms of the parameters presented in Table 1:

$$\sigma = \xi\, \rho\, g\, h, \tag{5}$$

where ξ is the lateral earth pressure coefficient:

$$\xi = \frac{\nu}{(1-\nu)}, \tag{6}$$

where ν is Poisson's ratio.

In this approximation, vertical and horizontal stresses were calculated with respect to the borehole axis.

Figure 4 shows longitudinal velocity maps for Specimens No. 4 and No. 5 (given in Table 1). Specimens C and D (sample depths of 157.1 and 200.3 m, respectively) were discarded due to the considerable variation of the P-wave velocity. Specimen C has a variation coefficient of 3.5 %, and specimen D of 2.1 %. A total of 54 velocity values were determined for each specimen (the grid of scanning was 9 by 6 points). Specimens A and B were homogeneous and structurally undisturbed; so they were investigated using the acoustic emission method.

Stress calculations were performed for granite, diorite, and granodiorite, which are igneous rocks; they are characterised by similar structural-textural features and similar behaviour under load. The resulting values of vertical and horizontal stresses are given in Table 2. The third column of the table contains the names of the specimens subjected to uniaxial compression accompanied with simultaneous recording of acoustic emissions.

Figure 5 shows the calculated distribution of the stress with depth (based on Table 2).

The specimens mentioned in Table 2 were subjected to uniaxial compression and acoustic emission was simultaneously recorded. It was found that the experimental relationship between stress and AE count is similar to that determined from theoretical experiments aimed at recovering in-situ stresses in different types of granite. Figure 6 shows the cumulative number of AE events (AE count N) versus the applied load (Specimen PB1-50). Calculated by the above formula, the averaged vertical stress at the sampling depth of PB1-50 is equal to 5.44 MPa. Using inflection of the experimental AE count versus stress curve (Figure 6), the in-situ stress the specimen experienced is estimated at 5.56 MPa; so the Felicity ratio is $FR = 1.02$. Thus, the error of in-situ stress estimation is 2 %.

The AE testing of Specimen PB1-113 produced similar results. Figure 6 shows the AE activity (Σ) versus the applied load for this sample. Clearly, two differently inclined tangents can be drawn to the AE

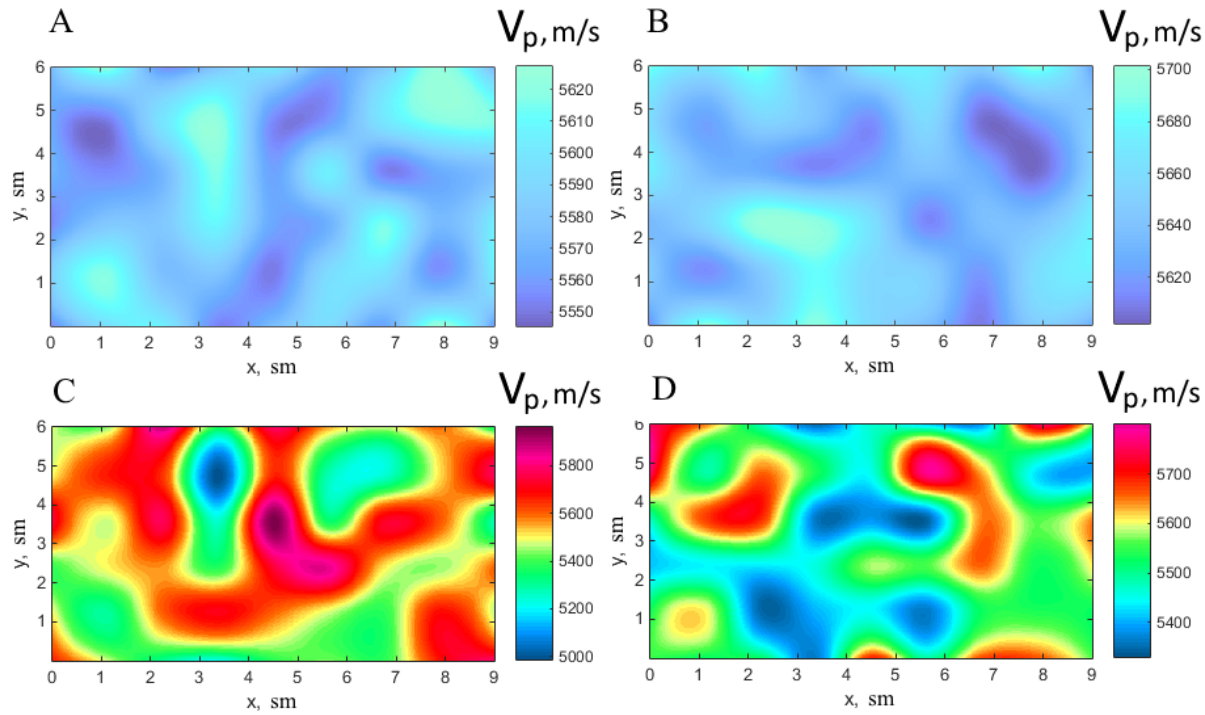

FIGURE 4. Velocity distributions: homogeneous specimens (A and B) and heterogeneous specimens (C and D).

Depth h from [m]	to	**Specimen №**	ρ [$g\,cm^{-3}$]	ν	ξ	[MPa]	[MPa]	**Rock type**
0	20,5		2,01	0,29	0,69	0,40	0,69	quaternary sediments
20,5	44,0		2,63	0,22	0,28	1,01	0,28	granite
44,0	74,8	PB1-4(74.6 m)	2,78	0,21	0,27	1,84	0,49	granite
74,8	95,7	PB1-11(95.5 m)	2,76	0,22	0,28	2,41	0,64	granodiorite
95,7	107,0		2,78	0,21	0,27	2,73	0,72	granodiorite
107,0	119,5		2,63	0,22	0,28	3,05	0,86	granite
119,5	121,8		2,58	0,33	0,49	3,11	1,53	granite
121,8	145,0		2,63	0,22	0,28	3,71	1,05	granite
145,0	150,2	PB1-29(150.0 m)	2,61	0,23	0,49	3,83	1,89	granite
150,2	153,0		2,58	0,33	0,49	3,91	1,93	granite
153,0	158,4	PB1-32(158.2 m)	2,59	0,22	0,28	4,04	1,14	granite
158,4	177,3		2,63	0,22	0,28	4,54	1,28	granite
177,3	193,7		2,64	0,21	0,28	4,96	1,40	granite
193,7	201,4	PB1-46(201.2 m)	2,61	0,29	0,41	5,15	2,10	granite
201,4	208,6		2,61	0,29	0,41	5,34	2,18	granite
208,6	212,4	PB1-50(212.2 m)	2,62	0,28	0,40	5,43	2,22	granite
212,4	228,2		2,61	0,29	0,41	5,84	2,38	granite
228,2	230,4	PB1-56(230.2 m)	2,65	0,20	0,25	5,89	1,47	granite
230,4	260,2	PB1-66(260.0 m)	2,65	0,20	0,25	6,67	1,67	granite
260,2	302,4	PB1-80(302.2 m)	2,65	0,20	0,25	7,76	1,94	granite
302,4	302,7		2,65	0,20	0,25	7,78	1,94	diorite
302,7	305,0		2,61	0,32	0,47	7,83	3,69	diorite
305,0	350,6	PB1-96(350.4 m)	2,65	0,20	0,25	9,01	2,25	diorite
350,6	400,6	PB1-113(400.6 m)	2,65	0,20	0,25	10,32	2,58	diorite

TABLE 2. The most intense UV-Vis spectral lines of SM-I and its investigated derivatives.

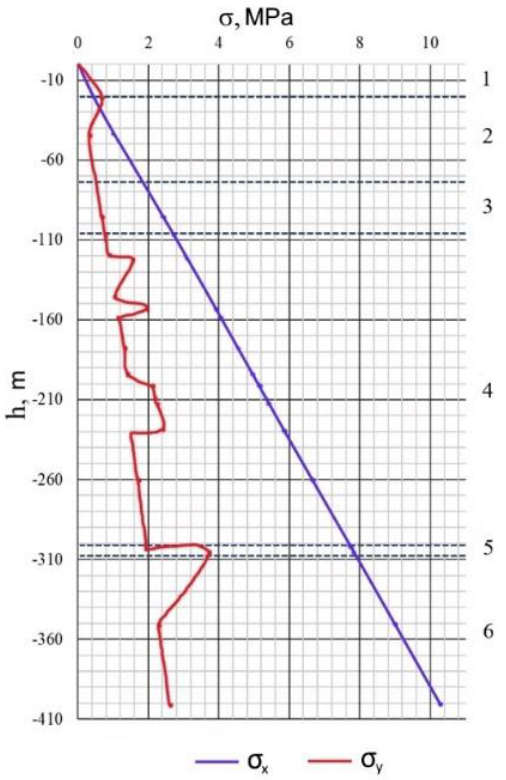

Figure 5. Distribution of averaged vertical and horizontal stresses with depth (deformation properties ignored) along the borehole axis: Quaternary sediments (1), granite (2), granodiorite (3), and granite (4); zone of higher level of fracturing (5); diorite (6) Quaternary sediments (1); granite (2); granodiorite (3); granite (4); zone of higher level of fracturing (5); diorite (6).

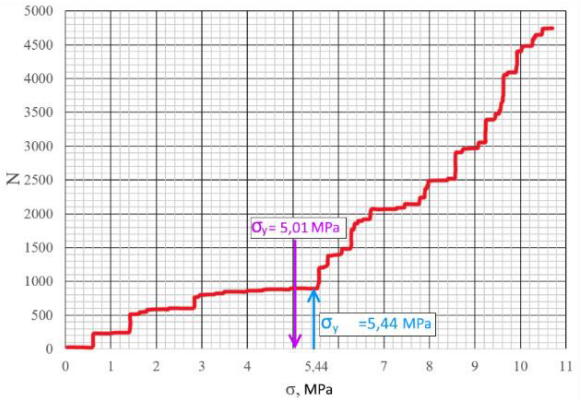

Figure 6. Cumulative AE count versus stress (Specimen PB 1-50): recovered in-situ stress value (purple arrow – approximate value of stresses acting in the array; blue arrow – the value of the restored voltage).

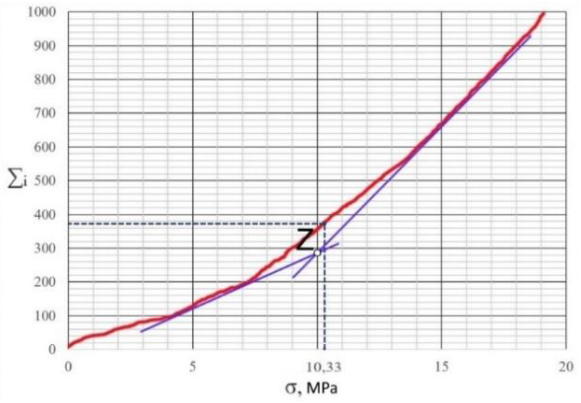

Figure 7. Cumulative AE count versus stress (specimen PB 1-113).

activity versus the applied load curve. The coordinate of the intersection of these tangent lines corresponds to the value of the in-situ vertical stress the specimen experienced before its recovery from the borehole. So, based on the results of AE testing of this sample, the vertical in-situ stress is 10.33 MPa, the stress memory factor being equal to 0.97 (based on numerical simulations, the vertical in-situ stress is 10.00 MPa). Note that this sample demonstrates a classical example of estimating the stress memory effect using the generally accepted technique of drawing tangents to linear sections of the AE count (N) vs. stress plot (point Z is the intersection of the tangents in Figure 7).

4. Discussion

Thus, in the case of specimen PB1-50 (granite), the stress memory effect is manifested by a significant increase in the AE count after the applied load has exceeded the previously experienced stress, which was observed in theoretical experiments as well. Specimen PB1-113 (diorite) did not show such a pattern; therefore, it was required that tangents be drawn. This is most likely due to lithological differences between the specimens.

Table 3 shows the values of calculated vertical stress σ_y and vertical stress $\sigma_y^{estimated}$ recovered from AE measurements, and the Felicity ratio FR_y. Clearly, except for a depth of 95.5-95.7 m, the values of the Felicity ratio are close to 1, belonging to the interval [0.81; 1.12], which indicates that the principal in-situ stress can be recovered.

5. Conclusions

The acoustic emission method based on the Kaiser effect has some advantages over other in-situ stress estimation methods. The method is an efficient and easy-to-use one. No complex high-precision deformation measurements are required. It is quite reasonable to use this AE method for studying the stress state of a rock mass. The method is very informative, describing in detail how the distribution of stress with depth depends on the structure of the rock mass.

Acknowledgements

This study was financially supported by the research team from the National Ministry of the interior of the Czech Republic VB01000057 and the authors also want to express their gratitude to the Czech Technical University in Prague for the grants No. 211453T11 and No. 211473T11.

Depth h from [m]	to	Specimen №	σ_y [MPa]	$\sigma_y^{estimated}$ [MPa]	FR_y
74,6	74,8	4	1,85	2,29	0,81
95,5	95,7	11	2,42	1,36	1,55
150,0	150,2	29	3,84	3,82	1,00
158,2	158,4	32	4,05	-	-
201,2	201,4	46	5,15	6,18	0,83
212,2	212,4	50	5,44	5,54	0,99
230,2	230,4	56	5,90	5,25	1,12
260,0	260,2	66	6,67	6,78	0,98
302,2	302,4	80	7,77	9,62	0,81
350,4	350,6	96	9,02	-	-
400,6	400,8	113	10,32	10,0	0,96

TABLE 3. Estimation of in-situ stresses using the AE method.

REFERENCES

[1] Y. A. Kashnikov, S. G. Ashikhmin, A. E. Kukhtinskii, D. V. Shustov. The relationship of fracture toughness coefficients and geophysical characteristics of rocks of hydrocarbon deposits. *Journal of Mining Institute* **241**:83, 2020. https://doi.org/10.31897/pmi.2020.1.83

[2] M. A. Karasev, M. A. Buslova, M. A. Vilner, T. T. Nguyen. Method for predicting the stress-strain state of the vertical shaft lining at the drift landing section in saliferous rocks. *Journal of Mining Institute* **240**:628, 2019. https://doi.org/10.31897/pmi.2019.6.628

[3] I. A. Shibaev, I. E. Sas, E. B. Cherepetskaya, D. M. Bagryantsev. Substantiation of possible simplifications in the assessment of soil-foundation interaction. *Mining informational and analytical bulletin* (9):152–157, 2018. https://doi.org/10.25018/0236-1493-2018-9-0-152-157

[4] X. F. Li, Q. B. Zhang, H. B. Li, J. Zhao. Grain-based discrete element method (GB-DEM) modelling of multi-scale fracturing in rocks under dynamic loading. *Rock Mechanics and Rock Engineering* **51**:3785–3817, 2018. https://doi.org/10.1007/s00603-018-1566-2

[5] H. Munoz, A. Taheri. Specimen aspect ratio and progressive field strain development of sandstone under uniaxial compression by three-dimensional digital image correlation. *Journal of Rock Mechanics and Geotechnical Engineering* **9**(4):599–610, 2017. https://doi.org/10.1016/j.jrmge.2017.01.005

[6] F. Wu, Y. Deng, J. Wu, et al. Stress–strain relationship in elastic stage of fractured rock mass. *Engineering Geology* **268**:105498, 2020. https://doi.org/10.1016/j.enggeo.2020.105498

[7] B. Amadei, O. Stephansson. *Rock Stress and its Measurement*. Chapman & Hall, London, Great Britain, 1997.

[8] J. Sjöberg, R. Christiansson, J. A. Hudson. ISRM suggested methods for rock stress estimation – Part 2: overcoring methods. *International Journal of Rock Mechanics and Mining Sciences* **40**(7):999–1010, 2003. https://doi.org/10.1016/j.ijrmms.2003.07.012

[9] A. Zang, O. Stephansson. *Stress Field of the Earth's Crust*. Springer, Potsdam, Germany, 2010, p 321.

[10] B. C. Haimson, F. H. Cornet. ISRM suggested methods for rock stress estimation – Part 3: hydraulic fracturing (HF) and/or hydraulic testing of pre-existing fractures (HTPF). *International Journal of Rock Mechanics and Mining Sciences* **40**(7):1011–1020, 2003. https://doi.org/10.1016/j.ijrmms.2003.08.002

[11] A. Lehtonen, J. W. Cosgrove, J. A. Hudson, E. Johansson. An examination of *in situ* rock stress estimation using the Kaiser effect. *Engineering Geology* **124**:24–37, 2012. https://doi.org/10.1016/j.enggeo.2011.09.012

[12] A. Lavrov. Fracture-induced physical phenomena and memory effects in rocks: A review. *Strain* **41**(4):135–149, 2005. https://doi.org/10.1111/j.1475-1305.2005.00233.x

[13] Z.-H. Zhang, J.-H. Deng. A new method for determining the crack classification criterion in acoustic emission parameter analysis. *International Journal of Rock Mechanics and Mining Sciences* **130**:104323, 2020. https://doi.org/10.1016/j.ijrmms.2020.104323

[14] E. Zezulová, K. Hasilová, T. Komárková, et al. NDT methods suitable for evaluation the condition of military fortification construction in the field. *Applied Sciences* **10**(22):8161, 2020. https://doi.org/10.3390/app10228161

[15] V. L. Shkuratnik, Y. L. Filimonov, S. V. Kuchurin. Acoustic emission memory effect in coal samples under uniaxial cyclic loading. *Journal of Applied Mechanics and Technical Physics* **47**:236–240, 2006. https://doi.org/10.1007/s10808-006-0048-6

[16] R. Yu, Y. Tian, X. Wang. Relation between stresses obtained from Kaiser effect under uniaxial compression and hydraulic fracturing. *Rock Mechanics and Rock Engineering* **48**(1):397–401, 2015. https://doi.org/10.1007/s00603-014-0573-1

[17] GOST R 55045-2012 Technical diagnostics. Acoustic emission diagnostics: Terms, definitions, and designations, Moscow, 2014.

[18] ISO 12716:2001 Non-destructive testing – Acoustic emission inspection – Vocabulary ISO/TC 135/SC 9 Acoustic emission testing.

[19] Y. Zhang, Y. Chen, R. Yu, et al. Effect of loading rate on the Felicity effect of three rock types. *Rock Mechanics and Rock Engineering* **50**:1673–1681, 2017. https://doi.org/10.1007/s00603-017-1178-2

[20] Y. Tian, R. Yu, Y. Zhang. Application of Felicity effect in crack stress identification and quantitative damage assessment of limestone. *Rock Mechanics and Rock Engineering* **53**:2907–2913, 2020. https://doi.org/10.1007/s00603-020-02062-x

[21] A. I. Sagaydak, V. V. Bardakov, S. V. Elizarov, V. I. Ivanov. Standards for the technical state testing of reinforced concrete structures by means of acoustic emission method. *Testing Diagnostics* (06):32–39, 2020. https://doi.org/10.14489/td.2020.06.pp.032-039

[22] N. N. Melnikov, S. P. Mesyats, S. P. Ostapenko, et al. Investigation of disturbed rock zones in open-pit mine walls by seismic tomography. In *Structural and Mechanical Engineering for Security and Prevention*, vol. 755 of *Key Engineering Materials*, pp. 147–152. Trans Tech Publications Ltd, 2017. https://doi.org/10.4028/www.scientific.net/KEM.755.147

[23] G. K. Zhang, H. B. Li, M. Y. Wang, X. F. Li. Crack initiation of granite under uniaxial compression tests: A comparison study. *Journal of Rock Mechanics and Geotechnical Engineering* **12**(3):656–666, 2020. https://doi.org/10.1016/j.jrmge.2019.07.014

[24] X. Liu, Q. Gu, Y. Tan, et al. Mechanical characteristics and failure prediction of cement mortar with a sandwich structure. *Minerals* **9**(3):143, 2019. https://doi.org/10.3390/min9030143

[25] I. A. Shibaev, V. A. Vinnikov, G. D. Stepanov. Determining elastic properties of sedimentary strata in terms of limestone samples by laser ultrasonics. *Mining Informational and Analytical Bulletin* (7):125–134, 2020. https://doi.org/10.25018/0236-1493-2020-7-0-125-134

[26] T. Y. Guo, L. N. Y. Wong. Microcracking behavior of three granites under mode I loading: Insights from acoustic emission. *Engineering Geology* **278**:105823, 2020. https://doi.org/10.1016/j.enggeo.2020.105823

[27] J. Kluczyński, L. Śnieżek, A. Kravcov, et al. The examination of restrained joints created in the process of multi-material FFF additive manufacturing technology. *Materials* **13**(4):903, 2020. https://doi.org/10.3390/ma13040903

[28] A. N. Kravcov, A. Konvalinka, V. A. Vinnikov, et al. On the issue of typical grain size assessment by the methods of broadband laser opto-acoustics. In *Structural and Mechanical Engineering for Security and Prevention*, vol. 755 of *Key Engineering Materials*, pp. 212–218. Trans Tech Publications Ltd, 2017. https://doi.org/10.4028/www.scientific.net/KEM.755.212

[29] J. Li, Y. Huang, Z. Chen, et al. Particle-crushing characteristics and acoustic-emission patterns of crushing gangue backfilling material under cyclic loading. *Minerals* **8**(6):244, 2018. https://doi.org/10.3390/min8060244

LINEARISATION OF A SECOND-ORDER NONLINEAR ORDINARY DIFFERENTIAL EQUATION

ADHIR MAHARAJ*, PETER G. L. LEACH, MEGAN GOVENDER, DAVID P. DAY

Durban University of Technology, Steve Biko Campus, Department of Mathematics, Durban, 4000, Republic of South Africa

* corresponding author: adhirm@dut.ac.za

ABSTRACT. We analyse nonlinear second-order differential equations in terms of algebraic properties by reducing a nonlinear partial differential equation to a nonlinear second-order ordinary differential equation via the point symmetry $f(v)\partial_v$. The eight Lie point symmetries obtained for the second-order ordinary differential equation is of maximal number and a representation of the $sl(3,R)$ algebra. We extend this analysis to a more general nonlinear second-order differential equation and we obtain similar interesting algebraic properties.

KEYWORDS: Lie symmetries, integrability, linearisation.

1. INTRODUCTION

Nonlinear differential equations are ubiquitous in mathematically orientated scientific fields, such as physics, engineering, epidemiology etc. Therefore, the analysis and closed-form solutions of differential equations are important to understand natural phenomena. In the search for solutions of differential equations, one discovers the beauty of the algebraic properties that the equations possess. Even though closed-form solutions are the primary objective, one cannot ignore the interesting properties of the equations [1–6]. In recent years, one such area in relativistic astrophysics involves the embedding of a four-dimensional differentiable manifold into a higher dimensional Euclidean space which gives rise to the so-called Karmarkar condition for Class I spacetimes [7]. The Karmarkar condition leads to a quadrature, which reduces the problem of determinig the gravitational behaviour of a gravitating system to a single generating function. This is then used to close the system of field equations in order to get a full description of the thermodynamical and gravitational evolution of the model. In a recent approach, Nikolaev and Maharaj [8] investigated the embedding properties of the Vaidya metric [9]. The Vaidya solution is the unique solution of the Einstein field equations describing the exterior spacetime filled with null radition of a spherical mass distribution undergoing dissipative gravitational collapse. In their work, Nikolaev and Maharaj showed that the Vaidya solution is not Class I embeddable but the generalised Vaidya metric describing an anisotropic and inhomogeneous atmosphere comprising of a mixture of strings and null radiation gives rise to interesting embedding properties. Here, we consider the nonlinear partial differential equation arising from the generalised Vaidya metric be of Class I. The governing equation is

$$2r^2mm'' - r^2m'^2 - 2rmm' + 3m^2 = 0, \tag{1}$$

where the prime denotes differentiation of the dependent variable, $m(v,r)$, with respect to the independent variable, r. Equation (1) is not v-dependent explicitly and possesses the point symmetry $f(v)\partial_v$ where $f(v)$ is an arbitrary function of v only. Using this symmetry, we obtain the invariants $r = x$ and $m = y(x)$, which reduces (1) to a nonlinear nonautonomous second-order ordinary differential equation

$$2x^2yy'' - x^2y'^2 - 2xyy' + 3y^2 = 0, \tag{2}$$

where y is a function of x only. We use the Lie symmetry approach to obtain the solution of (2). Using the solution of (2), we obtain the solution of (1).

2. PRELIMINARIES

Let (x,y) denote the variables of a two-dimensional space. Suppose that x is the independent variable and y is the dependent variable. An infinitesimal transformation in this space has the form

$$\bar{x} = x + \epsilon\xi(x,y) \tag{3}$$

$$\bar{y} = y + \epsilon\eta(x,y) \tag{4}$$

which can be regarded as generated by the differential operator

$$\Gamma \;=\; \xi(x,y)\frac{\partial}{\partial x} + \eta(x,y)\frac{\partial}{\partial y}. \tag{5}$$

Since we are concerned with point symmetries in this paper, ξ and η depend upon x and y only. Under the infinitesimal transformation (3) and (4), the nth derivative transform is given by

$$\zeta_n = \eta^{(n)} - \sum_{j=1}^{n}\binom{n}{j}y^{(n+1-j)}\xi^{(j)} \tag{6}$$

and

$$\Gamma_n = \zeta_n\frac{\partial}{\partial y^{(n)}}, \tag{7}$$

where the notation $\eta^{(n)}, \xi^{(j)}$ and $y^{(n)}$ denote the nth, jth and nth derivative of the dependent variable with respect to x. In the case of a function, $f(x, y, y', ..., y^{(n)})$, the infinitesimal transformation is generated by $\Gamma + \Gamma_1 + \Gamma_2 + ... + \Gamma_n$ which we write as $\Gamma^{[n]}$, where [10]

$$\Gamma^{[n]} = \Gamma + \sum_{i=1}^{n} \left[\eta^{(i)} - \sum_{j=1}^{i} \binom{i}{j} y^{(i+1-j)} \xi^{(j)} \right] \frac{\partial}{\partial y^{(i)}}, \quad (8)$$

is called the nth extension of Γ.

In the case of an equation

$$E(x, y, y', ..., y^{(n)}) = 0 \quad (9)$$

the equation is a constraint and the condition [11, 12] Γ a symmetry of the equation

$$\Gamma^{[n]} E|_{E=0} = 0, \quad (10)$$

i.e. the action of th nth extension of Γ on the function E is zero when the Equation (9) is taken into account. We note that $E = 0$ may be a scalar equation or a system of equations[1].

3. Symmetry analysis

The Lie point symmetries[2] of (2) are

$$\begin{aligned}
\Gamma_1 &= x\frac{\partial}{\partial x} \\
\Gamma_2 &= y\frac{\partial}{\partial y} \\
\Gamma_3 &= x^{3/2}\sqrt{y}\frac{\partial}{\partial y} \\
\Gamma_4 &= \sqrt{xy}\frac{\partial}{\partial y} \\
\Gamma_5 &= 2x\frac{\partial}{\partial x} + 3y\frac{\partial}{\partial y} \\
\Gamma_6 &= x^2\frac{\partial}{\partial x} + 3xy\frac{\partial}{\partial y} \\
\Gamma_7 &= \sqrt{\frac{y}{x}}\frac{\partial}{\partial x} + \left(\frac{y}{x}\right)^{3/2}\partial_y \\
\Gamma_8 &= \sqrt{xy}\frac{\partial}{\partial x} + \frac{3y^{3/2}}{\sqrt{x}}\frac{\partial}{\partial y}
\end{aligned}$$

which is a maximal number for a second-order ordinary differential equation and must be a representation of the $sl(3, R)$ algebra in the Mubarakzyanov Classification Scheme [21–24]. Equation (2) is linearisable to

$$\frac{d^2Y}{dX^2} = 0, \quad (11)$$

by means of a point transformation. The solution of (11) is

$$Y = AX + B, \quad (12)$$

while the solution of (2) is not exactly obvious. However, one can transform (2) to (11). We seek the transformation from (2) to (11) which casts $\Gamma_4 = \sqrt{xy}\partial_y$ into canonical form. Γ_4 assumes canonical form provided

$$\xi(x, y)\frac{\partial X}{\partial x} + \eta(x, y)\frac{\partial X}{\partial y} = 0 \quad (13)$$

$$\xi(x, y)\frac{\partial Y}{\partial x} + \eta(x, y)\frac{\partial Y}{\partial y} = 1, \quad (14)$$

where $\xi = 0$ and $\eta = \sqrt{xy}$ because (2) possesses a symmetry of the general form $\Gamma = \xi\partial_x + \eta\partial_y$.

When we apply the method of characteristics for first-order partial differential equations to (13) and (14), we obtain

$$\frac{dx}{0} = \frac{dy}{\sqrt{xy}} = \frac{dX}{0} \quad (15)$$

$$\frac{dx}{0} = \frac{dy}{\sqrt{xy}} = \frac{dY}{1} \quad (16)$$

for which the solutions are

$$X = x, \qquad Y^2 = \frac{4y}{x}. \quad (17)$$

Under the transformation (17), Equation (2) takes the form in (11). Hence we may apply (17) to (12) to obtain the solution to (2), which is

$$y(x) = \frac{1}{4}x(Ax + B)^2, \quad (18)$$

where A and B are two constants of integration.

By using the invariants $r = x$ and $m = y(x)$, the solution of (1) follows from (18) and is

$$m(v, r) = \frac{1}{4}r(A(v)r + B(v))^2, \quad (19)$$

where $A(v)$ and $B(v)$ are functions of integration.

4. The general case

We consider a general case by setting $y(x) = u^n$, where u is a function of x in Equation (2), we obtain a more general second-order equation

$$2nx^2uu'' + n(n-2)x^2u'^2 - 2nxuu' + 3u^2 = 0. \quad (20)$$

[1] An interested reader is referred to [13–16].

[2] The Mathematica add-on package SYM [17–20] was used to obtain the symmetries.

The Lie point symmetries of (20) are

$$\Lambda_1 = x\frac{\partial}{\partial x}$$
$$\Lambda_2 = \frac{\partial}{\partial x} + \frac{u}{nx}\frac{\partial}{\partial u}$$
$$\Lambda_3 = \frac{1}{n}x^{3/2}u^{1-n/2}\frac{\partial}{\partial u}$$
$$\Lambda_4 = \frac{1}{n}\sqrt{x}u^{1-n/2}\frac{\partial}{\partial u}$$
$$\Lambda_5 = 2x\frac{\partial}{\partial x} + \frac{3}{n}u\frac{\partial}{\partial u}$$
$$\Lambda_6 = x^2\frac{\partial}{\partial x} + \frac{3}{n}xu\frac{\partial}{\partial u}$$
$$\Lambda_7 = \sqrt{\frac{u^n}{x}}\frac{\partial}{\partial x} + \frac{u^{1+n/2}}{nx^{3/2}}\frac{\partial}{\partial u}$$
$$\Lambda_8 = \sqrt{xu^n}\frac{\partial}{\partial x} + \frac{3}{n}\sqrt{\frac{u^{n+2}}{x}}\frac{\partial}{\partial u}.$$

As (20) is a second-order ordinary differential equation and possesses eight Lie point symmetries, it is related to the generic second-order equation [25]

$$\frac{d^2Y}{dX^2} = 0. \quad (21)$$

When we apply the method of characteristics for first-order partial differential equations to (13) and (14), and using symmetry Λ_4, we obtain

$$\frac{dx}{0} = \frac{du}{\frac{1}{n}\sqrt{x}u^{1-n/2}} = \frac{dX}{0} \quad (22)$$
$$\frac{dx}{0} = \frac{du}{\frac{1}{n}\sqrt{x}u^{1-n/2}} = \frac{dY}{1} \quad (23)$$

for which the solutions are

$$X = x, \qquad Y^2 = \frac{4u^n}{x}. \quad (24)$$

From the solution of (21), by means of the transformation (24), we obtain the solution of (20) as

$$u(x) = \left(\frac{x}{4}\right)^{\frac{1}{n}}\left(C_1x + C_2\right)^{\frac{2}{n}}, \quad (25)$$

where C_1 and C_2 are constants of integration.

5. Conclusion

Most studies of the algebraic properties of ordinary differential equations are focused on the first, second and third order equations, which is most natural since these are the equations which arise in the modelling of natural phenomena. In this paper, we performed the symmetry analysis of Equation (2) and showed that the equation possesses the $sl(3,R)$ algebra. In turn, we reported the solution of (2) and thus obtained the solution of (1). A natural generalisation of (2) followed. By setting $m(v,r) = z^n$, where z is a function of v and r in Equation (1), we obtain a more general partial differential differential

$$2nr^2zz'' + n(n-2)r^2z'^2 - 2nrzz' + 3z^2 = 0, \quad (26)$$

where the prime denotes differentiation of the dependent variable, $z(v,r)$, with respect to the independent variable, r. We note that, as in Equation (1), (26) is not explicitly dependent on v, and therefore possesses the point symmetry $g(v)\partial_v$, where $g(v)$ is an arbitrary function of v only. We use this symmetry to obtain the invariants $r = x$ and $z = u(x)$ which reduce (26) to the second-order nonlinear Equation (20) with the solution given by (25). Using (25) and the invariants mentioned above, we obtain the solution for Equation (26) to be

$$z(v,r) = \left(\frac{r}{4}\right)^{\frac{1}{n}}\left(C_1(v)r + C_2(v)\right)^{\frac{2}{n}}, \quad (27)$$

where $C_1(v)$ and $C_2(v)$ are functions of integration.

This paper demonstrates that the Equations (1), hence (26), which, at first glance, looks complicated, has some very interesting properties from the viewpoint of Symmetry analysis. Using the symmetry approach we were able to show that these equations are integrable and have closed-form solutions.

Acknowledgements

MG expresses grateful thanks to the National Research Foundation of South Africa and the Durban University of Technology for their continuing support. AM acknowledges support of the Durban University of Technology. PGLL appreciates the support of the National Research Foundation of South Africa, the University of KwaZulu-Natal and the Durban University of Technology. DPD acknowledges the support provided by Durban University of Technology.

References

[1] B. Abraham-Shrauner, P. G. L. Leach, K. S. Govinder, G. Ratcliff. Hidden and contact symmetries of ordinary differential equations. *Journal of Physics A: Mathematical and General* **28**(23):6707, 1995. https://doi.org/10.1088/0305-4470/28/23/020

[2] K. Andriopoulos, P. G. L. Leach, A. Maharaj. On differential sequences. *Applied Mathematics & Information Sciences* **5**(3):525–546, 2011.

[3] C. Géronimi, M. R. Feix, P. G. L. Leach. Third order differential equation possessing three symmetries the two homogeneous ones plus the time translation. Tech. rep., SCAN-9905040, 1999.

[4] A. K. Halder, A. Paliathanasis, P. G. L. Leach. Singularity analysis of a variant of the Painlevé–Ince equation. *Applied Mathematics Letters* **98**:70–73, 2019. https://doi.org/10.1016/j.aml.2019.05.042

[5] A. Maharaj, P. G. L. Leach. Properties of the dominant behaviour of quadratic systems. *Journal of Nonlinear Mathematical Physics* **13**(1):129–144, 2006. https://doi.org/10.2991/jnmp.2006.13.1.11

[6] A. Maharaj, K. Andriopoulos, P. G. L. Leach. Properties of a differential sequence based upon the Kummer-Schwarz equation. *Acta Polytechnica* **60**(5):428–434, 2020. https://doi.org/10.14311/AP.2020.60.0428

[7] K. Karmarkar. Gravitational metrics of spherical symmetry and class one. *Proceedings of the Indian Academy of Sciences – Section A* **27**:56, 1948. https://doi.org/10.1007/BF03173443

[8] A. V. Nikolaev, S. D. Maharaj. Embedding with Vaidya geometry. *The European Physical Journal C* **80**(7):1–9, 2020. https://doi.org/10.1140/epjc/s10052-020-8231-0

[9] P. Chunilal Vaidya. The external field of a radiating star in general relativity. *Current Science* **12**:183, 1943.

[10] F. M. Mahomed, P. G. L. Leach. Symmetry Lie algebras of nth order ordinary differential equations. *Journal of Mathematical Analysis and Applications* **151**(1):80–107, 1990. https://doi.org/10.1016/0022-247X(90)90244-A

[11] H. Stephani. *Differential equations: Their solution using symmetries*. Cambridge University Press, 1989.

[12] G. W. Bluman, S. Kumei. *Symmetries and differential equations*, vol. 81. Springer Science & Business Media, 2013.

[13] A. Maharaj, P. G. L. Leach. The method of reduction of order and linearization of the two-dimensional Ermakov system. *Mathematical methods in the applied sciences* **30**(16):2125–2145, 2007. https://doi.org/10.1002/mma.919

[14] A. Maharaj, P. G. L. Leach. Application of symmetry and singularity analyses to mathematical models of biological systems. *Mathematics and Computers in Simulation* **96**:104–123, 2014. https://doi.org/10.1016/j.matcom.2013.06.005

[15] P. G. L. Leach. Symmetry and singularity properties of a system of ordinary differential equations arising in the analysis of the nonlinear telegraph equations. *Journal of mathematical analysis and applications* **336**(2):987–994, 2007. https://doi.org/10.1016/j.jmaa.2007.03.045

[16] P. G. L. Leach, J. Miritzis. Analytic behaviour of competition among three species. *Journal of Nonlinear Mathematical Physics* **13**(4):535–548, 2006. https://doi.org/10.2991/jnmp.2006.13.4.8

[17] K. Andriopoulos, S. Dimas, P. G. L. Leach, D. Tsoubelis. On the systematic approach to the classification of differential equations by group theoretical methods. *Journal of computational and applied mathematics* **230**(1):224–232, 2009. https://doi.org/10.1016/j.cam.2008.11.002

[18] S. Dimas, D. Tsoubelis. SYM: A new symmetry-finding package for Mathematica. In *Proceedings of the 10th international conference in modern group analysis*, pp. 64–70. University of Cyprus Press, 2004.

[19] S. Dimas, D. Tsoubelis. A new Mathematica-based program for solving overdetermined systems of PDEs. In *8th International Mathematica Symposium*, pp. 1–5. Avignon, 2006.

[20] S. Dimas. *Partial differential equations, algebraic computing and nonlinear systems*. Ph.D. thesis, University of Patras, Greece, 2008.

[21] V. V. Morozov. Classification of nilpotent Lie algebras of sixth order. *Izvestiya Vysshikh Uchebnykh Zavedenii Matematika* **4**:161–171, 1958.

[22] G. M. Mubarakzyanov. On solvable Lie algebras. *Izvestiya Vysshikh Uchebnykh Zavedenii Matematika* (1):114–123, 1963.

[23] G. M. Mubarakzyanov. Classification of real structures of Lie algebras of fifth order. *Izvestiya Vysshikh Uchebnykh Zavedenii Matematika* (3):99–106, 1963.

[24] G. M. Mubarakzyanov. Classification of solvable Lie algebras of sixth order with a non-nilpotent basis element. *Izvestiya Vysshikh Uchebnykh Zavedenii Matematika* (4):104–116, 1963.

[25] F. M. Mahomed, P. G. L. Leach. The linear symmetries of a nonlinear differential equation. *Quaestiones Mathematicae* **8**(3):241–274, 1985. https://doi.org/10.1080/16073606.1985.9631915

SELF-INTERFERENCE CANCELLATION IN UNDERWATER ACOUSTIC COMMUNICATIONS SYSTEMS USING ORTHOGONAL PILOTS IN IBFD

HALA A. NAMAN[a,b], AMMAR E. ABDELKAREEM[a,*]

[a] *Al-Nahrain University, College of Information Engineering, Department of computer Networks Engineering, Baghdad, Iraq*

[b] *University of Wasit, College of Engineering, Department of Architecture, Wasit, Iraq*

[*] corresponding author: Ammar.algassab@nahrainuniv.edu.iq

ABSTRACT. This paper proposes a Self-interference (SI) cancellation system model of Underwater acoustic (UWA) communication for in-band full-duplex (IBFD) technology. The SI channel is separated from the Far channel by exploiting a concurrently orthogonal pilot channel estimation technique using two orthogonal frequency-division multiplexing (OFDM) blocks to establish orthogonality between them based on a unitary matrix. Compared to the half-duplex channel estimator, the mean squared error (MSE) and the bit error rate (BER) provided strong evidence for the efficiency of the proposed SI cancellation. Since full-duplex systems are more efficient than half-duplex ones, the proposed approach might be seen as a viable option for them. The proposed method proved effective when used with a fixed full-duplex (FD) position and FD shifting of up to 4°. Different channel lengths and distances are adopted to evaluate the proposed method. Initial findings indicate that MSE for the SI channel minimum mean-square error (MMSE) estimator at 20 dB is $0.118 \cdot 10^{-3}$, for fixed FD. In addition, this paper presents a geometry channel model for the Far channel in the IBFD underwater communication system that describes the propagation delay of the multipath reflection. The simulation results for the multipath propagation delay spread are similar to the traditional results, with the delay spread of the suggested model reaching (79 ms), which is close to the Bellhop simulator result (78 ms).

KEYWORDS: Full duplex, self-interference cancellation, Far channel model, channel estimation, multipath propagation, underwater acoustic communication.

1. INTRODUCTION

Many industries have found a use for the UWA communication technology, which has been extensively researched and put into practice in areas including underwater sensor networks, marine environment observation, oceanographic engineering building, etc. [1]. UWA communication systems' spectral efficiency is limited by three variables: the small frequency bandwidth available, the complexity of UWA multipath propagation, and the slow speed of sound underwater ($1500\,\mathrm{m\,s^{-1}}$) [2, 3]. To maximise the usage of the radio spectrum, the FD communication technology was developed [4, 5]. This technology may also be applied to UWA communications systems. Many studies have been done on the viability of FD technology in UWA communication systems [6, 7], particularly the IBFD technology, due to its ability to increase system performance by a factor of two by doubling the frequency spectrum efficiency. Due to the signal of the near transmitter in FD interfering with the signal of interest from the far transmitter and preventing the receiver of FD from detecting the desired signal because of its high power and long delay spread of multipath propagation, the SI cancellation is a primary challenge regarding FD communications and has been the primary focus of research efforts. The SI cancellation may be realised in two ways: analog cancellation and digital cancellation. The SI cancellation performance can be enhanced by obtaining more precise SI and Far channel estimations [8, 9]. To reach an excellent estimation, we should be able to distinguish between the SI and the Far channel at the reception. This separation may be attained using orthogonality, which is employed in the transmission techniques of OFDM that operate in a half-duplex mode. Signals orthogonal to one another do not interact, conflict with one another, and can be examined individually without the other affecting the results. In order to estimate the SI and communication channel, it is common practice to employ a known pilot sequence; alternatively, it is recommended to use an orthogonal sequence as a pilot sequence. In this work, we assume that the corresponding positions of both the transmitter and the receiver are fixed. According to a research on SI channel characteristics, it is safe to deduce that the rapid channel fluctuations and the long SI channel reflections are the most crucial factors to take into account when developing a digital SI canceller.

2. Related works

In this section, we cover the literature on communication channel models for multipath propagation and self-interference cancellation methods in full-duplex transmissions. The suggested approach advances a previous research by maximising the precision of channel estimates while reducing unnecessary overhead.

In [10], the researchers suggested a model based on a binomial expression to describe the propagation delay of channel geometry for four types of multipath reflection based on the height difference between the transmitter and the receiver and the distance between them. They demonstrated that the attenuation coefficient would impact the system's efficiency when there is a significant height difference between the transmitter and receiver. In [11], a geometrical channel model for the propagation delay of multipath scattering based on the angles of departure and arrival in UWA communication was introduced. The researchers pretend that the multipath scatterers are spread out on the ocean surface and floor. In [12], a non-stationary wideband channel model in shallow water environments is proposed based on the angles of departure and angle of arrival. The researchers demonstrated that the suggested model was realistic and effective in enabling extended time/distance simulations because it takes into account numerous motion effects, such as time-varying angles, distances, and clusters' positions with the channel geometry caused by various motion factors that impact UWA channels. In [13], researchers offered a geometry model describing the propagation range and delay for direct and multipath reflected from surface and bottom in a tank environment with taking into account chemical constituents of water and sodium chloride with other factors of attenuation. They demonstrated that the transmission in the tank is substantially strong due to the enclosed space and the reflections from the tank wall and the surface and floor. Based on the previous literature, the previous models suffered from the complexity in geometry models and the direction of communication between the transmitter and the recipient is required to be in the horizontal direction only. In [14], researchers presented a digital SIC based on Non-parametric-Maximum-likelihood (NPML) with a sparse constraints approach to estimate the SI channel considering OFDM intended signal after Peak-to-Average Power ratio (PAPR) treated as non-Gaussian noise. The suggested method outperformed both standard NPML and LS in simulations and experiments, with a quicker convergence rate, more accurate SI channel estimate, and superior SI cancelation performance. In [15], researchers suggested a digital RF SIC system model of a transmitter and two receivers within the same equipment, used to collect a copy of the transmitted signal, which is then subtracted from the signal at the primary receiver. A Kalman filter is derived to estimate the correlated main channel and the auxiliary channel of both receivers in the presence of two forms of noise. In [16], researchers offered an SIC system model in Co-time Co-frequency FD (CCFD) UWA communication. To improve the performance of digital SIC by using the reconstructed SI signal from the SI channel obtained using an adaptive filter, they suggested using the SI signal combined with the intended signal in the estimation of the SI channel. In [17], an SIC model to estimate the SI and communication channels concurrently across a FD connection utilising orthogonal pilot sequences was proposed. The HD and FD of both channel estimators using the Cramer-Rao Lower Bound were compared. The estimators' effectiveness depends on the sequence length and number of channel taps. Maintaining sequence orthogonality and synchronisation through correlation characteristics is crucial to the efficacy of channel estimators. Both channel estimators are impacted by the cross-correlation deviation, whose sequences that are not synchronised at the receiver will determine the impact on the performance. The results also indicated a degradation of the estimator's performance with increasing channel length. Additionally, most existing works suffer from overhead and complexity caused by iterations of an adaptive filter; also, any small error in SI residual will affect the SIC performance.

Below is a description of the paper's contribution. We proposed a system model that can eliminate self-interference signal in the digital domain in an FD configuration by separating the Self signal from the Far signal without needing a complex overhead adaptive filter. The proposed system for cancelling self-interference employs two orthogonal OFDM blocks by creating an orthogonality between the Self signal and the Far signal, resulting in the complete separation of the two signals, proved mathematically, and the complete cancelation of self-interference. The proposed model does not depend on the channel length or the tap number of the channel impulse response and also applied efficiency with fixed FD and shifted FD. Additionally, we proposed a simple geometrical model for the Far channel based on a triangle to describe the multipath propagation of shallow underwater acoustic communication. The suggested model provides flexibility to the direction between the transmitter and receiver and consists of the direct path, multipath propagated by reflections on the sea surface, and multipath propagated by reflections on the sea floor. The outline for this paper is as follows: In Section 3, we dissect the proposed system model for channel model and SI cancellation. The simulation results and discussion are described in Section 4. Section 5 offers a summary of the paper.

3. System model

In this section, we introduce the architecture of the SIC model for the IBFD-UWA communication system along with the channel model, including both SI and Far channels and the measurements.

3.1. Structure of both transmitters

This work explores a scenario in which two UWA nodes communicate in IBFD mode where the Far node is a transmitter, and the Self node is a receiver. OFDM is used with quadrature phase shift keying (QPSK) modulation method with $\boldsymbol{N}$ subcarriers and equispaced comb-type pilot patterns for channel estimation with data index $\boldsymbol{d}$ and pilot index $\boldsymbol{p}$. The OFDM block $\boldsymbol{x}$ has been obtained by IFFT of baseband transmitted signal $\boldsymbol{X}$, which contains data and pilot subcarriers.

$$x = \text{IFFT}\{X\} = \frac{1}{N}\sum_{k=0}^{N-1} X[k] \exp\left(\frac{-j2\pi kn}{N}\right) \tag{1}$$

For each OFDM block, the cyclic prefix selected of length longer than the propagation of the excessive delay of the impulse response has been considered to overcome ISI caused by multipath propagation.

In the proposed system for full-duplex SIC, it is assumed that the Self and Far nodes use real-valued equispaced comb-type pilot patterns with the same subcarriers with index p as shown in Figure 1.

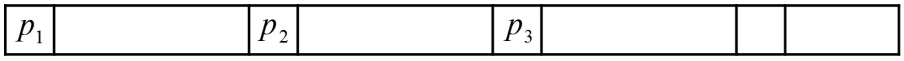

Figure 1. Pilot pattern.

Pilot vector $X_p = \left[P_1, P_2, \ldots, P_{N_p}\right]^T$ with the length N_p has been used for both Self and Far nodes.

At the Self node part, after the combination of data X_d at index d and pilot X_p at index p, the data X_S were created. Then, data X_S passed through IFFT and cyclic prefix blocks and $x_{S_{cp}}$ has been obtained. By using a similar way, $x_{F_{cp}}$ has been obtained at the Far node part. These two signals are subsequently sent through the SI and communication channels. The following subsection shows the model of SI and far channels.

3.2. The model of the channel

We construct a propagation channel model in this subsection, assuming a typical shallow water setting with water column level d_W shown in Figure 2.

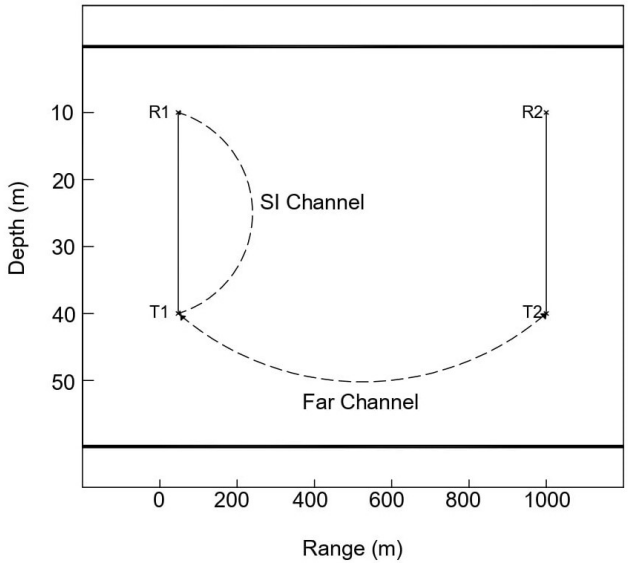

Figure 2. An acoustic IBFD shallow water communication system.

The two transmitted signals pass through their separate channels, indicated by the SI channel and Far channel, respectively. The UWA channel has a significant impact on the performance of the IBFD underwater wireless communication system. Due to the strong self-interference and multipath propagation, reliable information about the SI and communication channels are required to develop SI cancellation strategies successfully.

3.2.1. Far channel model

Characterising the propagation delay, spreading loss, transmission loss, and absorption loss of the vertical channel is essential for developing a fundamental model of the channel. Distance-related weakening of signal strength is expressed as a decibel (dB) value called transmission loss (TL). Attributable to a combination of

spreading loss and attenuation, it is quantified by [18]. The latter is what would happen if the sound was transmitted and immediately converted into heat due to friction.

$$\mathrm{TL}\,(f) = 2\alpha_z + k\,\log_{10}(r) + a\,(f)\,r, \tag{2}$$

where α_z denotes the 15 dB attenuation in the zy and zx planes. This is due to the fact that both the transducer and the receiver employ toroidal transducers with a beam pattern, r represents the propagation range in meters, and k is the spreading factor, which is 10 for spherical spreading and 20 for free-field spreading. In this computation, a practical law that lies between both the spherical and cylindrical laws is selected. The presence of magnesium sulphate in saltwater begins to contribute extra attenuation at frequencies lower than 500 kHz. Despite its low quantity in saltwater, boric acid contributes at frequencies lower than 700 Hz, and the equations that follow are related to the computation of $\alpha(f)$ where:

$$\alpha(f) = \alpha_1 + \alpha_2 + \alpha_3, \tag{3}$$

$$\text{(Freshwater attenuation) } \alpha_1 = af^2, \tag{4}$$

$$\text{(MgSO}_4\text{Relaxation) } \alpha_2 = b\,f_0/(1 + (f_0/f)^2), \tag{5}$$

$$\text{(Boric acid relaxation) } \alpha_3 = c\,f_1/(1 + (f_1/f)^2), \tag{6}$$

$$a = 1.3 \times (10 * \exp(-7)) + 2.1 \times ((10 * \exp(-10))\,(T - 38)^2, \tag{7}$$

$$b = 2S \times (10 * \exp(-5))\,, \tag{8}$$

$$c = 1.2 \times 10^{-4}, \tag{9}$$

$$f_0 = 50 \times (T + 1), \tag{10}$$

$$f_1 = (10)^{(T-4)/100}, \tag{11}$$

where $S = 35$ represents salinity in h, $T = 14$ means temperature in degrees of Celsius, and f=12 kHz indicates frequency band.

To model the communication channel between the self and far nodes, we propose a geometry model to represent the multipath propagation in the Far channel based on a triangle by setting the angle between the FD modem direction and water column $\theta = 90°$. Direct path propagation delay T_D is determined by using the velocity formula:

$$T_D = (D_T - D_R)/c, \tag{12}$$

where the transmitter depth, denoted by D_T, and the reception depth, indicated by D_R and $c = 1500$ means the sound speed. This model posits that D_R is not constant, and its value varies with respect to D_T. As seen in Figure 3, the angle $\theta = 90°$ is between a column of water and the FD direction.

$$D_R = D_T - L * \cos(\theta)\,, \tag{13}$$

where the distance L is separated between the transmitter and receiver. According to Figure 3, the delay in the propagation between the transmitter and the receiver may be calculated using the Pythagorean theorem of right triangles, whether the signal is traveling over a straight path or multipath. In this case, the hypotenuse reflects the time it takes for each reflection to complete its propagation. There are two sorts of assumed reverberations: surface reflections, in which the initial reflection occurs on the surface, and bottom reflections, in which the initial reflection occurs on the seafloor.

According to the Pythagorean theorem in a vast triangle, S constitutes d_1, which shows the propagation range by the initial reflection between the transmitter and the surface (the magnitude of the vertical motion on

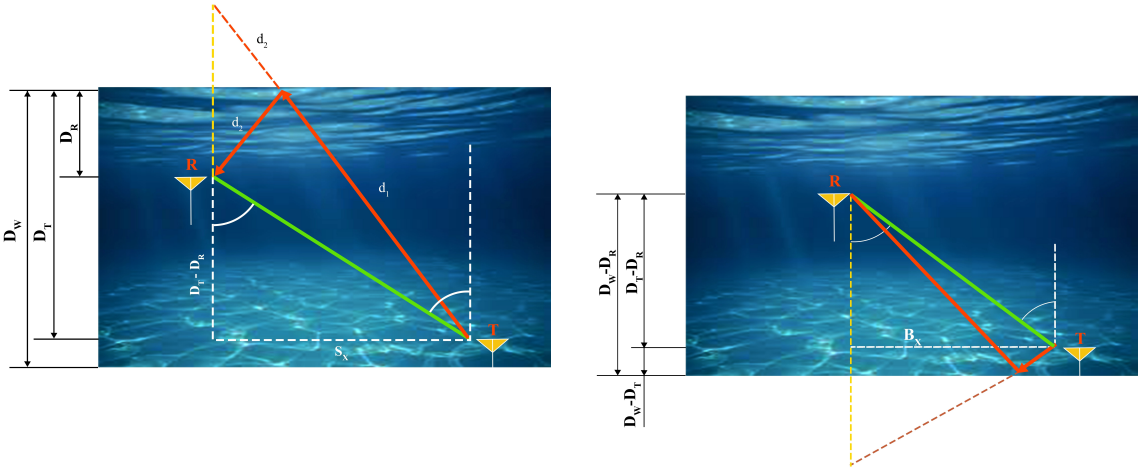

(A). Surface reflections. (B). Bottom reflections.

FIGURE 3. Multipath reflections in Far channel.

the first reflection line segment is equal to D_T) and then to the receiver, d_2 (the magnitude of the vertical motion on the second reflection line segment is equal to D_R) after drawing the reflected distance, d_2 is supplied to d_1 as an extension. So the sum of the vertical motion on these two line segments d_1 and d_2 is equal to $D_T + D_R$. The side indicated by S_y is perpendicular to the hypotenuse, while the side indicated by S_x is next to it.

$$S = \sqrt{{S_x}^2 + {S_y}^2} \tag{14}$$

$$S_y = D_T + D_R \tag{15}$$

$$S_x = (D_T + D_R) \tan\theta \tag{16}$$

For every number of surface reflections, n, between 1 and N, the propagation delay is calculated as:

$$S_{y_n} = D_T + \left[\frac{n}{2}\right] 2D_W + (-1)^{n+1} D_R, \tag{17}$$

where D_W is the water depth.

$$T_{Sn} = \left(\sqrt{(D_T + D_R)^2 \tan^2\theta + \left(D_T + \left[\frac{n}{2}\right] 2D_W + (-1)^{n+1} D_R\right)^2}\right)/c \tag{18}$$

The same method is used to calculate the time taken for a single bottom reflection to propagate. As illustrated in Figure 9 and the corresponding equation, B_x is unaffected by the number of reflections, whereas B_y does change.

$$B = \sqrt{{B_x}^2 + {B_y}^2} \tag{19}$$

$$B_y = D_T + D_R \tag{20}$$

$$B_x = (D_T - D_R) \tan\theta \tag{21}$$

For every number of bottom reflections, n, between 1 and N, the propagation delay is calculated as:

$$B_{y_n} = \left[\frac{n}{2}\right] 2D_W - \left(D_T + (-1)^{n+1} D_R\right) \tag{22}$$

The propagation delay for any number of reflections is computed depending on the velocity formula:

$$T_{Bn} = \left(\sqrt{(D_T - D_R)^2 \tan^2 \theta + \left(\left[\frac{n}{2} \right] 2D_W - \left(D_T + (-1)^{n+1} D_R \right) \right)^2} \right) / c \tag{23}$$

For normal incidence waves at the ocean's surface boundary, the pressure reflection coefficient is around -1, whereas for waves reflected off the ocean floor, it is roughly 1. Reflections from surfaces that are evenly spaced contribute positively at the receiver, whereas reflections from uneven surfaces or the bottom negatively.

Figure 4 shows the Far channel response of the multipath between the source and the receiver. The delay spread of the echoes in the Far channel was as high as 79 ms because of the multipath propagation. This is because the arrival times, amplitudes, and phases of signals change depending on the lengths of their original signal routes and the delay spread. Intersymbol interference is caused by the delayed receiver copies; hence, the propagation delay of the multipath compared to the direct path is an important feature of the underwater channel.

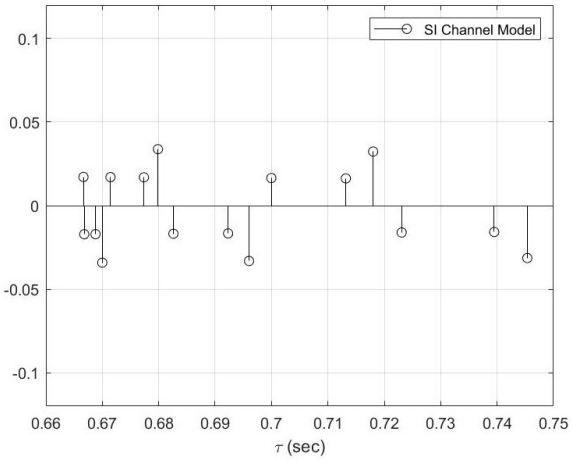

Figure 4. Far magnitude CIR with L=1000.

The Bellhop simulator [19] is used to evaluate the effectiveness of the proposed model with the same configuration parameters (D_W, D_R, D_T, L, f) as shown in Figures 5a and 5b, where the red path indicates a direct path or a signal that originates at the sea floor and refracts or diverges upwards until it encounters a steep positive sound speed gradient at which point it refracts downwards. By reflecting off of the water's surface and/or bottom, the signal may make its way to the receiver via the water's green route. In this case, the black routes indicate an increase in multipath components at the receiver as a result of a more significant number of potential paths reflected off of the sea surface and the uneven sea bottom. Results are relatively comparable when comparing the delay spread of the suggested model (79 ms) to those of the Bellhop simulator [19] (78 ms).

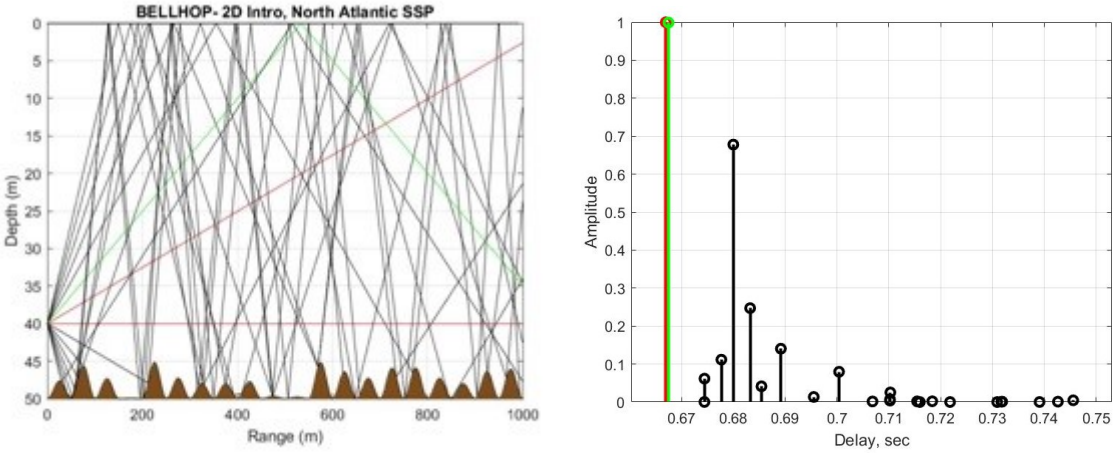

(a). Ray trace. (b). CIR.

Figure 5. Bellhop's multipath propagation setting in underwater.

3.2.2. SI CHANNEL MODEL

The channel coefficients and the magnitude channel impulse response, in seconds, for the Self node are generated based on the proposed modelr [20]. Due to the fluid nature of the marine environment, including the movement of organisms and ships, the FD may be displaced from the vertical direction at varying angles with the water column.

This research assumes two situations to describe a self-interference channel: one in which the angle between the water column and the FD direction is 0 degrees and another in which it is 4 degrees, as seen in Figure 6.

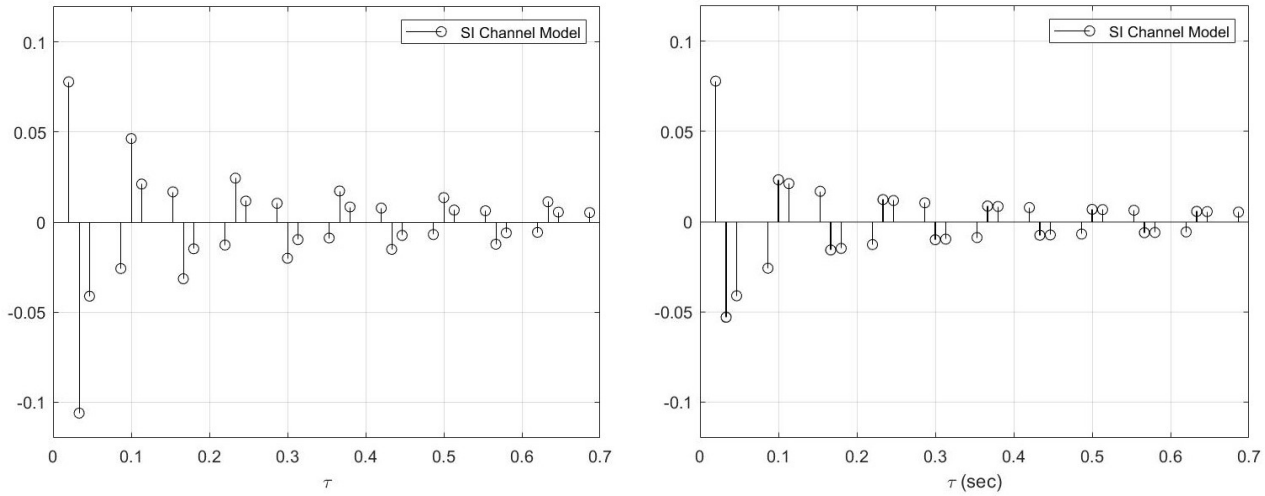

(A). $\theta = 0°$. (B). $\theta = 4°$.

FIGURE 6. SI magnitude CIR with L=30.

3.3. STRUCTURE OF THE RECEIVER

In this section, we propose a model that can remove self-interference in a full-duplex system by separating the Self signal from the Far signal. As mentioned previously, the two transmitted signals pass through their separate channels denoted SI channel and Far channel, respectively, and the summation of them with AWGN noise is received by the receiver antenna of the Self node, $\boldsymbol{r_{cp}}$ as shown in Figure 7.

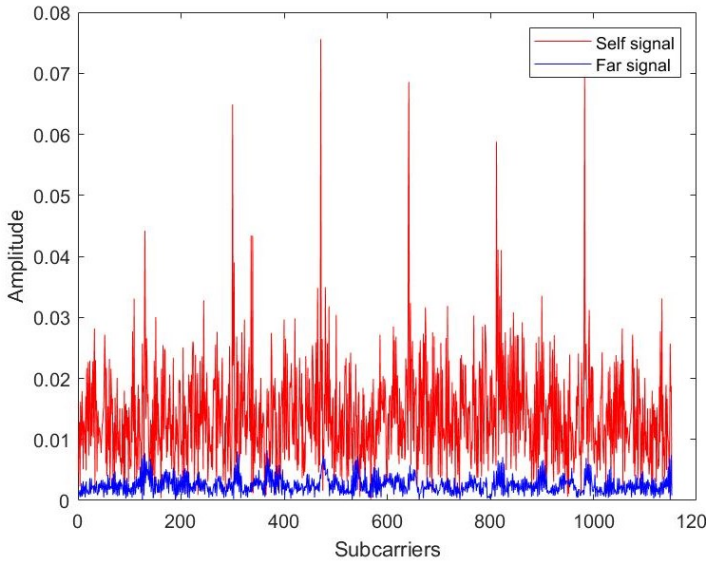

FIGURE 7. Received signals.

After removing the cyclic prefix and getting FFT from the received signal r_{cp} as illustrated in Figure 8, with an indication to number of subcarriers at each block, we have:

$$R = \tilde{X}_S H_S + \tilde{X}_F H_F + \mathcal{N}. \tag{24}$$

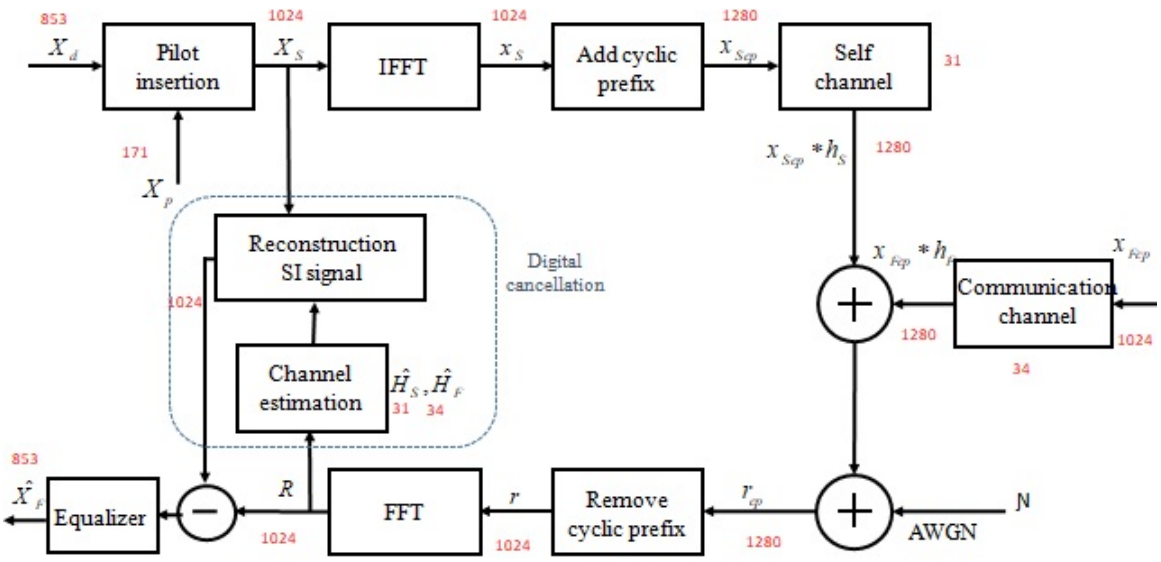

Figure 8. Structure of SIC-based OFDM IBFD-UWA communication system.

Whose $\tilde{X}$ referred to the diagonal matrix created by X.

$$X = [X_1, X_2, \ldots, X_N]^T$$
$$\tilde{X} = \begin{bmatrix} X_1 & 0 & 0 & 0 \\ 0 & X_2 & 0 & 0 \\ 0 & 0 & \ddots & \vdots \\ 0 & 0 & \ldots & X_N \end{bmatrix} \tag{25}$$

The proposed system assumed that the Self and Far channels are fixed for two OFDM blocks, and the Self node uses the pilot vector X_p for the first OFDM block, same as the Far node, but it uses $-X_p$ as the pilot vector for the second OFDM block, unlike the Far node that uses the same X_p as the first block. So we have

$$\begin{aligned} R_1 &= \tilde{X}_{S_1} H_S + \tilde{X}_{F_1} H_F + \mathcal{N}_1, \\ R_2 &= \tilde{X}_{S_2} H_S + \tilde{X}_{F_2} H_F + \mathcal{N}_2. \end{aligned} \tag{26}$$

In matrix form, we have

$$\begin{bmatrix} R_1 \\ R_2 \end{bmatrix} = \begin{bmatrix} \tilde{X}_{S_1} & \tilde{X}_{F_1} \\ \tilde{X}_{S_2} & \tilde{X}_{F_2} \end{bmatrix} \begin{bmatrix} H_S \\ H_F \end{bmatrix} + \begin{bmatrix} \mathcal{N}_1 \\ \mathcal{N}_2 \end{bmatrix} \tag{27}$$

If only pilot subcarriers for two received OFDM blocks R_1 and R_2 have been chosen, we have

$$\begin{bmatrix} R_{p_1} \\ R_{p_2} \end{bmatrix} = \begin{bmatrix} \tilde{X}_p & \tilde{X}_p \\ -\tilde{X}_p & \tilde{X}_p \end{bmatrix} \begin{bmatrix} H_{pS} \\ H_{pF} \end{bmatrix} + \begin{bmatrix} \mathcal{N}_{p_1} \\ \mathcal{N}_{p_2} \end{bmatrix} = A \begin{bmatrix} H_{pS} \\ H_{pF} \end{bmatrix} + \begin{bmatrix} \mathcal{N}_{p_1} \\ \mathcal{N}_{p_2} \end{bmatrix} \tag{28}$$

The matrix A is a $2N_p \times 2N_p$ real-valued unitary matrix [], $A^T A = I$, so the channel frequency response (CFR) of Self and Far channels in pilot subcarriers can be estimated by:

$$\begin{bmatrix} \hat{H}_{pS} \\ \hat{H}_{pF} \end{bmatrix} = \begin{bmatrix} \tilde{X}_p & \tilde{X}_p \\ -\tilde{X}_p & \tilde{X}_p^T \end{bmatrix}^T \begin{bmatrix} R_{p_1} \\ R_{p_2} \end{bmatrix} \tag{29}$$

With an interpolation, Self, and Far CFRs, $\hat{H}_S$ and $\hat{H}_F$ are estimated and because $\tilde{X}_{S_1}$ and $\tilde{X}_{S_2}$ are known by the Self node we have; therefore, SI $\hat{X}_{F_1}$ and $\hat{X}_{F_2}$ can be obtained by

$$\begin{bmatrix} \hat{X}_{F_1} \\ \hat{X}_{F_2} \end{bmatrix} = \tilde{\hat{H}}_F^{-1} \left(\begin{bmatrix} R_1 \\ R_2 \end{bmatrix} - \begin{bmatrix} \tilde{X}_{S_1} \\ \tilde{X}_{S_2} \end{bmatrix} \hat{H}_S \right) \tag{30}$$

In the proposed system, it can be seen that at the Self node, the separation of two Self and Far signals has been done completely, and SI cancellation from the Far node signal is made perfectly.

4. Simulation results

In this section, the simulation results of the proposed method for full-duplex systems will be discussed. The proposed orthogonal self-interference cancelation method based on mathematical proofs has no restrictions on the channel characteristics and all the channels that can be used in the OFDM system can be used in the proposed full-duplex system. Therefore, the proposed method for eliminating self-interference from Far signal is independent of the number of channel taps unlike method of [17], where the orthogonality condition is satisfied only in a certain number of channel taps.

Of course, similar to other communication systems, the characteristics of the channel, the length of the channel impulse response, the number of pilots used for the channel estimation and the type of the method used for channel estimation will be important and influential for the channel estimation efficiency of the proposed system and the MSE and BER curves, but it will not have any effect on the main goal of the proposed paper, which is the complete and accurate removal of self-interference signal from the Far signal.

All simulations are done in MATLAB based on the system model shown in the Figure 8 and Table 1 and the simulation results are the average of 1000 simulation repetitions. In the following figures, the efficiency of the proposed method for self-interference cancelation and channel estimation is well illustrated by MSE and BER parameters.

Parameter	**Value**
Bandwidth B	6 kHz
Number of sub-carrier Nc	1024
Signal constellation	QPSK
CP interval	256 (1024/4)
Carrier frequency	12 kHz
Sampling frequency	48 kHz
Pilot arrangement	Comb type

Table 1. Simulation parameters.

In the following figures, the simulation results of the proposed self-interference cancelation method for full-duplex systems are shown based on establishing orthogonality between two Self signals and Far signals in different modes and the efficiency and performance of the proposed system have been evaluated.

As shown in Figure 9, the MSE curve of the Far channel estimation in the two modes of the proposed full-duplex and the conventional half-duplex completely coincide, and this figure shows the accuracy and efficiency of the proposed method, which results in the correct separation of the Self and Far channels that is obtained based on orthogonality and is the main goal and contribution of this paper. In the MSE curves, the estimation efficiency of the Self channel is better than that of the Far channel because the Self channel has better conditions due to the proximity of the transmitter and receiver.

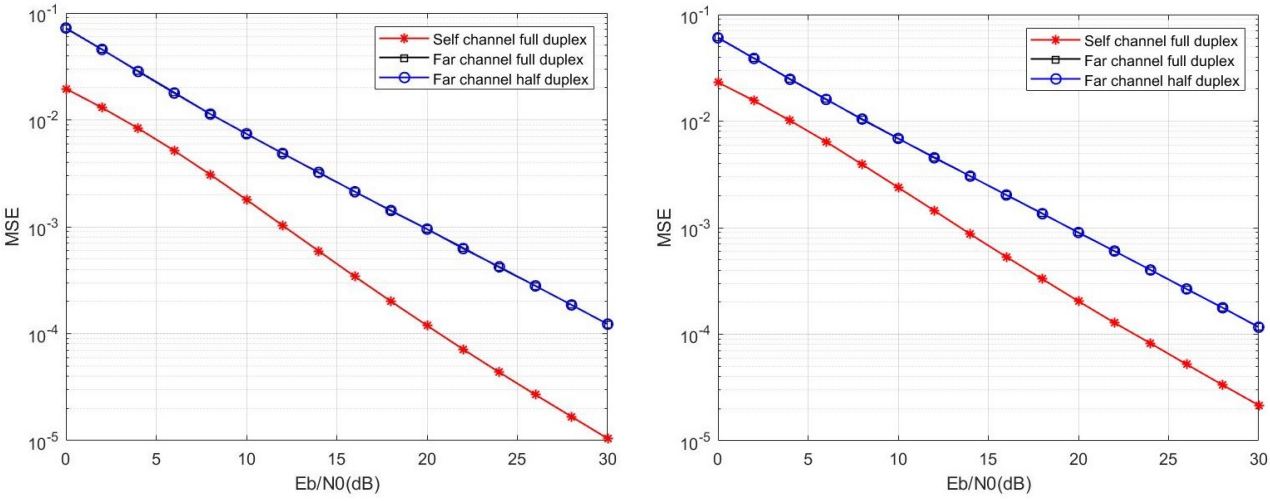

(a). $\theta = 0°$. (b). $\theta = 4°$.

Figure 9. MSE of the MMSE channel estimation at different angles.

In Figure 10, the BER curves for two full-duplex and half-duplex systems are illustrated. It can be seen that the two curves are not exactly identical and there is a slight difference between them. But this difference is inevitable and is not the reason for the inefficiency of the proposed method. According to the BER curve, the performance of the half-duplex system is slightly better than the full-duplex system, which is related to the overall structure of the full-duplex system.

In the half-duplex system, the Far channel is first estimated, then the Far data are extracted. But in the full-duplex system, in general, the Self channel is estimated first. Then the product of the estimated Self channel by the Self data is calculated and is subtracted from the received data. Finally, according to the data obtained from the previous step, the Far channel is estimated and the Far data are extracted, according to equation 30 (of course, in the proposed method, due to the existence of orthogonality, both Self and Far channels are estimated simultaneously). That is why the bit error efficiency of the half-duplex system is slightly better than that of the full-duplex system. Of course, it should be mentioned again that the bandwidth usage of the full-duplex system is twice that of the half-duplex system.

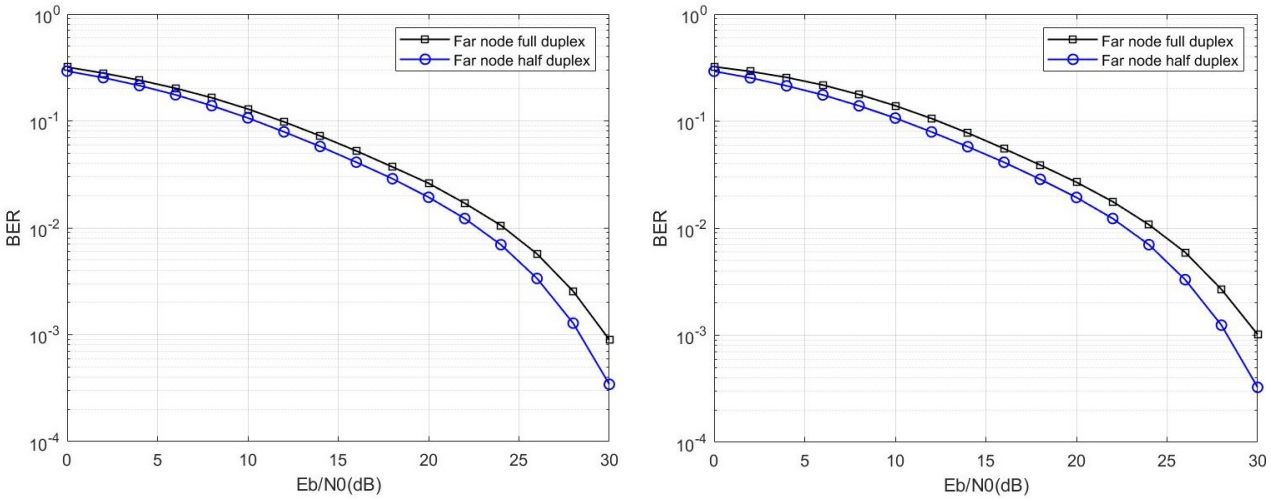

(A). $\theta = 0°$. (B). $\theta = 4°$.

FIGURE 10. BER of the MMSE channel estimation at different angles.

In Figure 11 and Figure 12, the MSE and BER curves were displayed using the MMSE channel estimation method for different channels with different channel lengths. As can be concluded from these figures, the proposed method for cancelling self-interference has no limitations and is suitable for each channel with different characteristics. Also, we can see from Figure 13 and Figure 14 that the proposed orthogonal full-duplex method has a high efficiency in dealing with different Self-node and Far-node distances, and changes in the distance do not affect the system's efficiency.

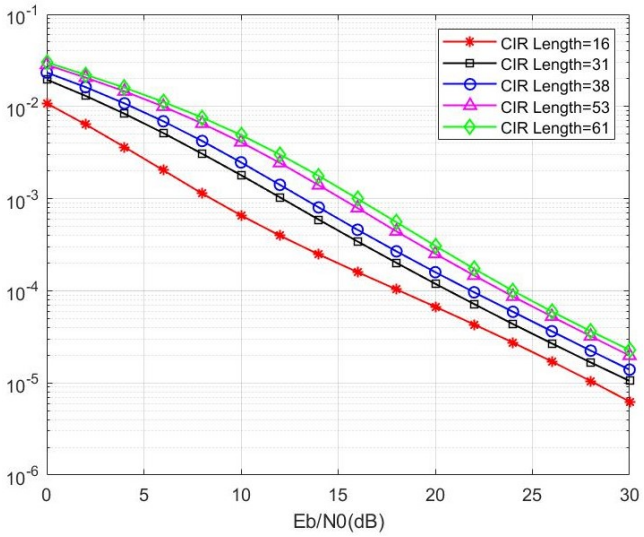

FIGURE 11. MSE of the SI MMSE channel estimation with different CIR length.

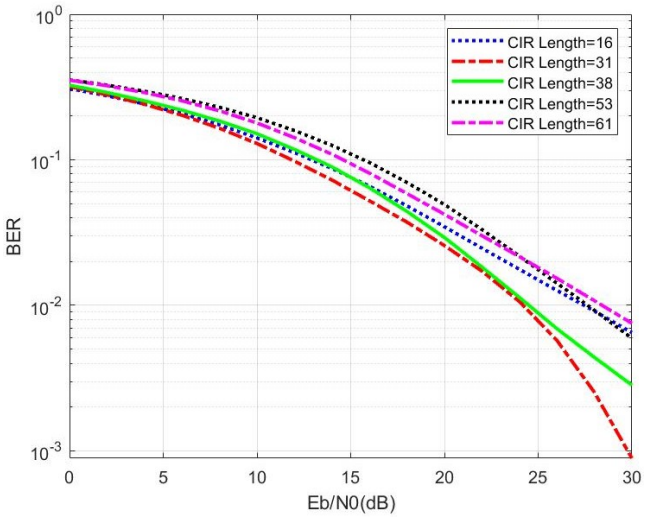

FIGURE 12. BER of the Far MMSE channel estimation with different CIR length.

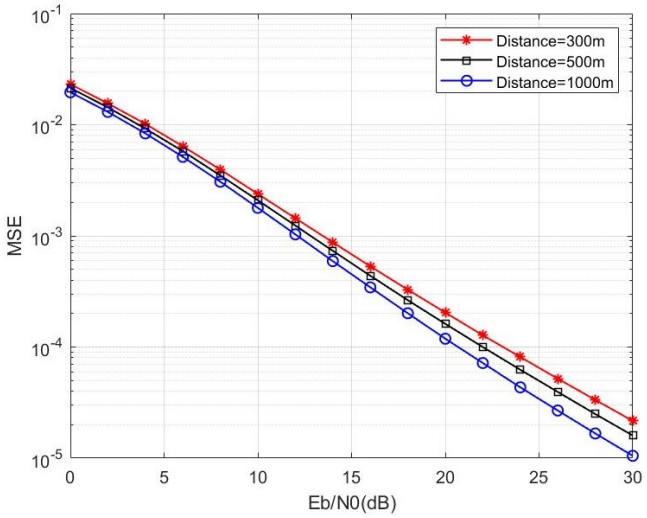

FIGURE 13. MSE of the SI MMSE channel estimation with different distances.

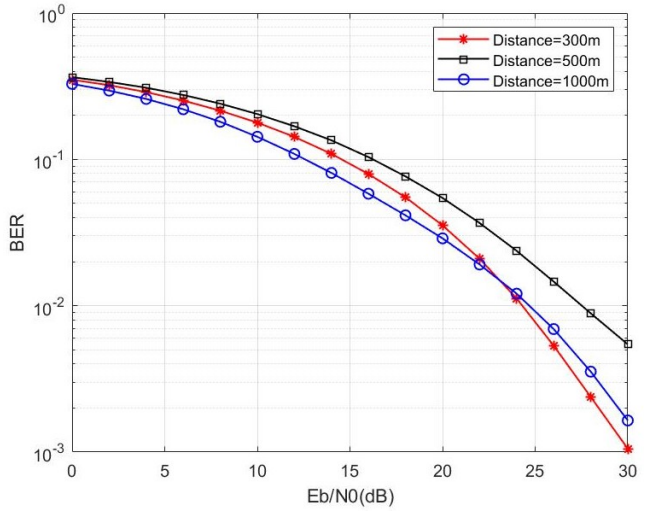

FIGURE 14. BER of the Far MMSE channel estimation with different distances.

Finally, Figure 15 shows the actual and estimated channel frequency response for both the Self-channel and the Far-channel. As can be seen, the channel estimation accuracy is excellent in both channels, and this is due to the accurate separation of the two Self signal and Far signal. In the proposed system, by establishing orthogonality conditions between two signals, the estimation of both channels occurs simultaneously and the elimination of self-interference is done effectively, which is a big problem in full-duplex systems, and the proposed method of this paper can be a suitable solution of this problem.

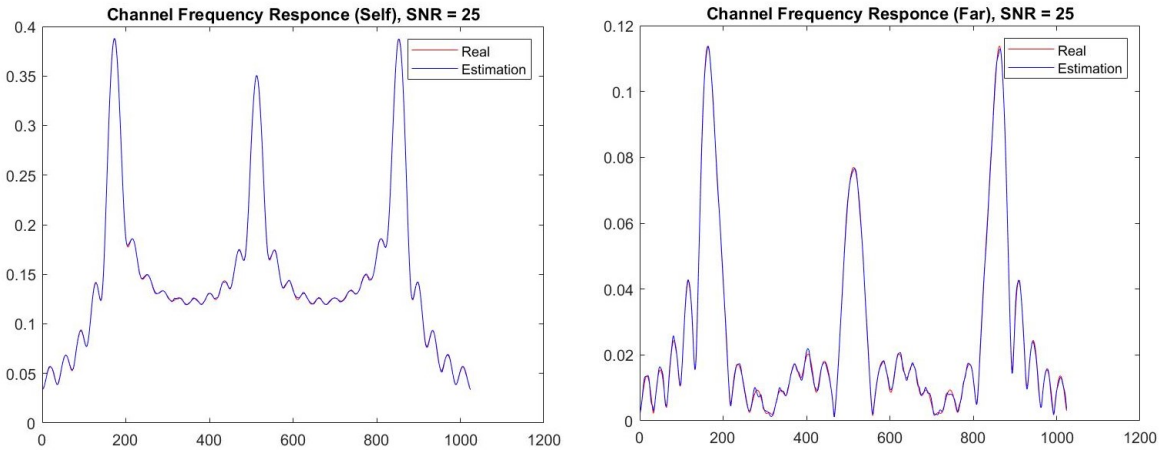

(a). Self channel. (b). Far channel.

Figure 15. Estimation of CFR.

5. Conclusion

In this paper, the separation of Self signal from Far signal in full-duplex systems is presented. The proposed self-interference cancelation method uses two received OFDM blocks and provides orthogonality between the Self signal and the Far signal, and in this way separates the Far signal from the self-interference signal. The main contribution of this paper is the complete and accurate cancelation of self-interference from the Far signal without the conditions of the Self and Far channels affecting the efficiency of the proposed method, unlike previous works that had these problems. The correctness of the proposed method has been proved mathematically and it has been shown by a simulation and comparison with the half-duplex system that the efficiency of channel estimation and receiving Far-node data in the proposed full-duplex system are the same as that of the half-duplex system. It is also shown that the proposed method has a good performance with fixed or shifted FD and no dependence on the channel length or distance. As a result, the proposed method can be considered a good solution for full-duplex systems with much better spectral performance than half-duplex systems. The findings also indicate that the proposed channel model correctly represents the behaviour of multipath propagation in a shallow water environment in a delay spread as compared with the traditional works in horizontal communications, where the results at $\theta = 90°$are very close with Bellhop simulator for delay spread measurement.

References

[1] M. Stojanovic, J. Preisig. Underwater acoustic communication channels: Propagation models and statistical characterization. *IEEE Communications Magazine* **47**(1):84–89, 2009. https://doi.org/10.1109/MCOM.2009.4752682

[2] A. E. Abdelkareem, B. S. Sharif, C. C. Tsimenidis, J. A. Neasham. Compensation of linear multiscale Doppler for OFDM-based underwater acoustic communication systems. *Compensation of Linear Multiscale Doppler for OFDM-Based Underwater Acoustic Communication Systems* **2012**:139416, 2012. https://doi.org/10.1155/2012/139416

[3] M. C. Domingo. Overview of channel models for underwater wireless communication networks. *Physical Communication* **1**(3):163–182, 2008. https://doi.org/10.1016/j.phycom.2008.09.001

[4] Z. Zhang, K. Long, A. V. Vasilakos, L. Hanzo. Full-duplex wireless communications: Challenges, solutions, and future research directions. *Proceedings of the IEEE* **104**(7):1369–1409, 2016. https://doi.org/10.1109/JPROC.2015.2497203

[5] K. E. Kolodziej, B. T. Perry, J. S. Herd. In-band full-duplex technology: Techniques and systems survey. *IEEE Transactions on Microwave Theory and Techniques* **67**(7):3025–3041, 2019. https://doi.org/10.1109/TMTT.2019.2896561

[6] G. Qiao, S. Liu, Z. Sun, F. Zhou. Full-duplex, multi-user and parameter reconfigurable underwater acoustic communication modem. In *2013 OCEANS – San Diego*, pp. 1–8. 2013. https://doi.org/10.23919/OCEANS.2013.6741096

[7] J. Zhang, G. Qiao, C. Wang. Acoustic communication networks. In *2013 OCEANS – San Diego*, pp. 1–6. 2013. https://doi.org/10.23919/OCEANS.2013.6741129

[8] L. Shen, B. Henson, Y. Zakharov, P. Mitchell. Digital self-interference cancellation for full-duplex underwater acoustic systems. *IEEE Transactions on Circuits and Systems II: Express Briefs* **67**(1):192–196, 2020. https://doi.org/10.1109/TCSII.2019.2904391

[9] L. Li, A. Song, L. J. Cimini, et al. Interference cancellation in in-band full-duplex underwater acoustic systems. In *OCEANS 2015 - MTS/IEEE Washington*, pp. 1–6. 2015. https://doi.org/10.23919/OCEANS.2015.7404411

[10] Y. Widiarti, Suwadi, Wirawan, T. Suryani. A geometry-based underwater acoustic channel model for time reversal acoustic communication. In *2018 International Seminar on Intelligent Technology and Its Applications (ISITIA)*, pp. 345–350. 2018. https://doi.org/10.1109/ISITIA.2018.8711067

[11] J. Zhou, H. Jiang, P. Wu, Q. Chen. Study of propagation channel characteristics for underwater acoustic communication environments. *IEEE Access* **7**:79438–79445, 2019. https://doi.org/10.1109/ACCESS.2019.2921808

[12] X. Zhu, C.-X. Wang, R. Ma. A 2D non-stationary channel model for underwater acoustic communication systems. In *2021 IEEE 93rd Vehicular Technology Conference (VTC2021-Spring)*, pp. 1–6. 2021. https://doi.org/10.1109/VTC2021-Spring51267.2021.9448976

[13] S. Panchal, S. Patel, S. Panchal, J. Pabari. Design of novel channel propagation model for underwater acoustic wireless communication inside a tank. *Research Square* 2022. https://doi.org/10.21203/rs.3.rs-1842984/v1

[14] G. Qiao, S. Gan, S. Liu, Q. Song. Self-interference channel estimation algorithm based on maximum-likelihood estimator in in-band full-duplex underwater acoustic communication system. *IEEE Access* **6**:62324–62334, 2018. https://doi.org/10.1109/ACCESS.2018.2875916

[15] M. Shammaa, H. Vogt, A. El-Mahdy, A. Sezgin. Adaptive self-interference cancellation for full duplex systems with auxiliary receiver. In *2019 International Conference on Advanced Communication Technologies and Networking (CommNet)*, pp. 1–8. 2019. https://doi.org/10.1109/COMMNET.2019.8742358

[16] Z. S. Liu, Q. J. Zhou, W. S. Gan, et al. Adaptive joint channel estimation of digital self-interference cancelation in co-time co-frequency full-duplex underwater acoustic communication. In *2019 IEEE International Conference on Signal, Information and Data Processing (ICSIDP)*, pp. 1–5. 2019. https://doi.org/10.1109/ICSIDP47821.2019.9173156

[17] A. M. M. Chandran, L. Wang, M. Zawodniok. Channel estimators for full-duplex communication using orthogonal pilot sequences. *IEEE Access* **8**:117706–117713, 2020. https://doi.org/10.1109/ACCESS.2020.3002726

[18] R. F. W. Coates. *Underwater acoustic systems.* Macmillan, 1990. https://doi.org/10.1007/978-1-349-20508-0

[19] N. Morozs. Channel modeling for underwater acoustic network simulation, 2020. P. 1–25. https://doi.org/10.24433/CO.1789096.v1

[20] H. A. Naman, A. E. Abdelkareem. Variable direction-based self-interference full-duplex channel model for underwater acoustic communication systems. *International Journal of Communication Systems* **35**(7):e5096, 2022. https://doi.org/https://doi.org/10.1002/dac.5096

FEMTOSECOND LASER PROCESSING OF ADVANCED TECHNICAL MATERIALS

Tomáš Primus[a,b,*], Martin Novák[a], Pavel Zeman[a], František Holešovský[b]

[a] *Czech Technical University in Prague, Faculty of Mechanical Engineering, Department of Production Machines and Equipment, Horská 3, 128 00 – Prague 2, Czech Republic*

[b] *Czech Technical University in Prague, Faculty of Mechanical Engineering, Department of Machining, Process Planning and Metrology ,Technická 4, 160 00 – Prague 6, Czech Republic*

[*] corresponding author: T.Primus@rcmt.cvut.cz

Abstract. Ultra-short pulsed laser ablation may be used for high-precision machining with very low thermal influence on the processed materials. Due to this reason, lasers are increasingly used for processing of advanced materials, such as titanium alloys, nickel-based alloys or steel, every year. In this study, four advanced technical materials were analysed and compared under femtosecond laser irradiation with three different wavelengths. The main laser-material interaction parameters were identified, namely the ablation threshold and removal efficiency parameters. Higher removal rates were found for Ti6Al4V alloy with all three harmonic wavelengths. To increase process productivity, a method of increasing the repetition rate and scanning speed was presented. With the maximum repetition rate, the productivity increased five-fold with a similar removed depth and surface quality. Finally, the suitability of the identified parameters with regard to quality and productivity was demonstrated for fabrication of two complex structures – honeycomb and dot – which has the potential to improve friction properties of advanced materials.

Keywords: Femtosecond laser ablation, Ti6Al4V, Inconel 718, AISI 316L, tool steel, surface texture.

1. Introduction

Ultra-fast lasers operating with femtosecond or picosecond pulses have seen a significant development in the last few years [1]. They have become irreplaceable in many industrial sectors, such as electronics [2], material processing [3] or surface structuring and functionalization [3, 4]. The benefits of ultra-fast laser processing include very precise material processing without heat affection and high process control [5]. However, the knowledge of ablation behaviour and laser-matter interaction is crucial before commencing material processing. Basic ablation characteristics include an ablation threshold and removal efficiency [6, 7]. The ablation threshold indicates the minimum fluence needed to start the material ablation [5, 8, 9]. Removal efficiency can be defined as the amount of material removed per time and per energy input [5]. It has been determined that the maximum removal efficiency can be found for e^2 multiple of the threshold fluence [6]. However, a low process productivity, coupled with the high cost of devices, remains a significant limit. There are several approaches to increasing productivity, including both newly developed methods, such as burst mode [10, 11] or multi-beam technique, [12] and more conventional methods, such as optimization of wavelength [2], in-creased repetition rate [2, 13, 14] or changes in the pulse duration [15]. There are fewer studies of conventional methods, even though optimisation of the repetition rate, energy and wavelength can increase the productivity of the ablation process several-fold on an existing laser equipment. In addition, published studies related to laser matter-interaction basics (e.g. [9, 15, 16]) deal with removal rates in nm/pulse or µm/pulse, which can be difficult to use in practical applications. Moreover, a complex comparison of the ablation characteristics for the same laser set-up among advanced materials, such as steel, titanium alloy and nickel-based alloy is absent from the open literature. These selected materials are used in a wide range of applications ranging from automotive, medicine, oil, and chemical industries to aerospace industry [17–19]. A thorough description of an optimisation of wavelength, laser power and repetition rate for maximizing productivity in the available laser system is likewise lacking, despite the fact that this knowledge is necessary for a wider industrial use of ultra-fast lasers.

This paper presents a complex comparison of ablation behaviour with respect to the surface quality of advanced highly-used industrial materials (Ti6Al4V, Inconel 718, tool steel and stainless steel) under femtosecond laser irradiation by using three different wavelengths. The ideal ablation parameters were studied in depth through an increasing repetition rate experiment resulting in an increased process productivity. Finally, the experimentally obtained results were demonstrated in a complex structure production for a possible tribology application.

2. Materials and methods

2.1. Laser set-up

A femtosecond laser source (Ligtcon Carbide CB3-40W) was used for the experiments. This source was integrated into a Master 1 laser micro-machining station with optical paths for three harmonic wavelengths $\lambda = 1030\,\text{nm}$, 515 nm, 343 nm. The laser beam was delivered through galvo-scanners (InteliScan14) and focused with a F-theta lens on the working plane. The main characteristics of the laser set-up and laser source are listed in Table 1.

Laser source	**Lightcon Carbide CB3-40W**
Wavelength λ [nm]	1030 (IH), 515 (IIH), 343 (IIIH)
Power P_{avg} [W]	40 (IH), 20 (IIH), 11 (IIIH)
Repetition rate f [kHz]	200–1000
Pulse duration τ_p	260 fs –10 ps
Beam quality TEM00; M^2	<1.2 (IH)

Table 1. Laser source type used with main parameters.

2.2. Materials

Four technical materials, namely two types of steel, Inconel 718 nickel-based alloy and Ti6Al4V titanium grade 5 alloy, were chosen for this study. A total of one round shape sample with a diameter of 80 mm and thickness of 15 mm from each material was prepared for the experiments. The surface of the samples was finished by grinding and the initial surface roughness was measured using an InfiniteFocus G5 optical microscope. The results of the initial surface roughness measurements are listed in Table 2. The detailed chemical composition of these materials is listed in Table 3 and their physical properties are listed in Table 4.

Material	**Ra [µm]**	**Rz [µm]**
Tool steel	0.36	3.04
Inconel 718	0.26	2.25
Ti6Al4V	0.40	2.87
Stainless steel	0.40	3.03

Table 2. Initial surface roughness of the samples measured by an optical method according to ISO 25178 standard explained by the parameter Sa (arithmetical mean height of the area) and Sz (maximum height of the area).

3. Methods

In this paper, the full process chain of laser surface structuring is described for four advanced materials (tool steel, stainless steel, Ti6Al4V and Inconel 718). Firstly, the ablation threshold of all four materials under femtosecond laser irradiation with three different wavelengths was studied. Then, the ablation behaviour by removal rates and volume ablation rate with surface roughness was demonstrated for three harmonics. In the interest of increasing surface structuring productivity, the use of a higher repetition rate and scan speed was demonstrated and evaluated. Finally, the suitability of the obtained parameters was demonstrated on surface structuring of two designed structures (dot and honeycomb). The aim of this study is to directly compare the ablation behaviour of four advanced technical materials under laser irradiation from three different wavelengths and femtosecond pulses. Moreover, the obtained parameters were used to increase structuring productivity and complex surface structure preparation.

3.1. Pre-experiment of hatching angle evaluation

Firstly, the effect of the hatching angle on surface roughness was studied to eliminate the effect of the scanning parameters on material behaviour after the laser ablation process. Hatching angle ($\varphi°$) can be defined as an angle of rotation between each laser scanning passes, see Figure 1. For this experiment, 9 different hatching angles were set according to previous knowledge and results from [25]. The main idea for choosing hatching angles was an appropriate combination of even and odd numbers, prime numbers, and including angles from 15 to 90 degrees. Other laser and scanning parameters were kept constant, based on previous knowledge and consequence to upcoming experiments and can be found in Table 5. This experiment was done on the tool steel material, where squares of 5×5 mm were fabricated by 120 laser passes. After each pass, the hatching angle was rotated by φ.

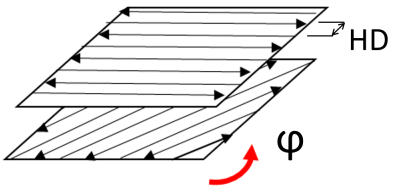

Figure 1. The effect of the hatching angle on surface roughness expressed by Sa [µm].

One of the constant scanning parameters was pulse overlap (S_x), defined as the percentage overlapping of pulses in the beam moving direction. Overlap S_x can be expressed by Equation (1) as the function of the scanning speed v [mm/s], repetition rate f [Hz] and beam diameter 2ω [mm].

Material	Designation	Chemical composition (Wt [%])					
Tool steel	1.2379	C 1.4-1.6	Cr 11-12.5	Mo 0.6-0.9	V 1.2	Mn 0.2-0.4	Si 0.2-0.5
Inconel 718	2.4668	Ni+Co 50-55	Cr 17-21	Mo 2.8-3.3	Ti 0.65-1.15	Al 0.2-0.8	Nb+Ta 4.75-5.5
Ti6Al4V (grade 5)	3.7164	Al 5.5-6.7	V 3.5-4.5	Fe 0-0.4	C <0.08		
Stainless steel (AISI 316L)	1.4404	Cr 16.5-18	Ni 10	Mo 2-2.5	C <0.03		

Table 3. Chemical composition of the samples in Wt [%] and their designation according to DIN norm. Chemical composition data were received from the material supplier.

Material	Melting point [°C]	Density [g/cm³]	Thermal conductivity [W/m K⁻¹]	Thermal expansion coefficient [x10⁻⁶ K]	Ref.
Tool steel	1560	7.6	18.5–20	9.8–12.9	[20]
Inconel 718	1321–1393	8.1	9.3–11.5	8–12	[21, 22]
Ti6Al4V	1660	4.5	6.7–7.3	8.7–9.1	[23]
Stainless steel	1375–1400	7.99	13–17	15–18	[24]

Table 4. The physical properties of tested materials.

Wavelength (λ)	1030 nm
Pulse overlap (Sx)	90 %
Fluence (F)	3.5 J/cm^2
Repetition rate (f)	200 kHz
Square size	5×5 mm
Number of passes	120
Hatching angle (φ)	15°, 17°, 30°, 45°, 53°, 60°, 75°, 83°, 90°

Table 5. Process and scanning parameters used to determine the hatching angle effect on surface roughness.

$$S_x = 1 - \frac{v}{2\omega_0 f} \tag{1}$$

The hatching overlap (H_y) [%] is the percentage overlapping of the hatching lines with a defined hatch distance (HD) and known beam diameter, according to Equation (2). In this study, the same S_x and H_y values were set for all the experiments.

$$H_y = \frac{D - HD}{D} \cdot 100 \tag{2}$$

The surface roughness of the ablated craters was evaluated by the same optical method as the reference state. Parameter Sa [μm] is the arithmetical mean height of the area, an extension parameter of Ra [μm]. Sa values were obtained from measurements of the whole area (5×5 mm) using the Gaussian robust filter according to ISO 25178 [26].

3.2. Ablation thresholds

Different numbers of pulses for ablation threshold determination, varying from 1 to 1000, can be found in the literature [5, 6, 9]. For this experiment, 10 pulses in one place were selected due to the continuity with laser machining with an overlap of 90 %. The ablation threshold evaluation method used in this study, presented, for example, by [6], is based on measuring the crater (spot) diameter. As energy increases, the crater diameter increases, especially for metals. Then, the threshold fluence ($F_{th} = J/cm^2$) and exact spot diameter ($2\omega_0$) can be evaluated using the approximation computation by Equation (3) [6]:

$$\ln 2E_p = \frac{D^2}{2\omega_0^2} + \ln F_{th} + \ln \pi\omega_0^2, \tag{3}$$

where D^2 is the crater diameter for pulse energy E_p. In our case, each selected E_p was repeated ten times in a row and then the crater diameters were measured and averaged to increase the measurement accuracy. For a direct comparison of the ablation behaviour of the selected materials, all three available wavelengths were used.

3.3. Removal efficiency

The removal efficiency experiment was designed using the known ablation threshold values and optimal hatching angle. The main idea of these experiments was to determine the ablation behaviour of the chosen materials, especially the removed volume of material per time. Two different expressions were used for the determination of the ablation efficiency: removal rates $\Delta V/P_{avg}$ [mm^3/min/W] and volume ablation rates

ΔV [mm^3/min] with respect to the surface quality, expressed by the parameter Sa [µm] the arithmetical mean height of the area. Removal rates can be also expressed as a function of fluence threshold (F_{th}) and optical penetration depth δ. Finally, the best values of fluence efficiency were used for the experiment with increasing scanning speed and constant overlap.

$$\frac{\Delta V}{P_{avg}} = \frac{1}{4} \cdot \frac{\delta}{F_{th}} \cdot \ln^2(2 \cdot \frac{F}{F_{th}}) \tag{4}$$

For the removal rate estimations, the squares of 5×5 mm were ablated with 120 laser passes and hatch rotation by a defined angle after each pass. The proper hatching angle was set according to the pre-experimental results. The experiment was performed with a repetition rate of 200 kHz and pulse duration around $\tau \approx 267$ femtoseconds. All of the parameters used in the experiment are presented in Table 6.

λ [nm]	2ω [μm]	S_x, H_y [%]	f [kHz]	τ [fs]
1030 (IH)	33	90	200	267
515 (IIH)	31	90	200	267
343 (IIIH)	22	90	200	267

TABLE 6. Laser and scanning parameters for the removal efficiency experiment.

After laser processing, the samples were cleaned for 15 minutes with ethanol in an ultrasonic bath. The depth and surface roughness of the ablated craters were evaluated with an InfiniteFocus G5 optical microscope (Bruker Alicona, Austria). For detailed observations, a laser confocal microscope VKX-1000 from Keyence was employed.

3.4. Increasing scanning speed and repetition rates

The experimental design that was used for the removal rates was also used for the increasing productivity experiment by increasing the repetition rate with a constant overlap. This experiment was performed for all the materials and for one laser wavelength (1030 nm). The constant parameter of laser fluences found to be the most effective in terms of removal rates was used. Then, the repetition rate was increased from 100 kHz to 1 MHz, with a constant overlap of 90 %, which also resulted in an increase of the scanning speed from 660 to 6600 mm/s. The main idea of this experiment was to determine the highest achievable laser ablation productivity with our laser source.

3.5. Surface structuring

Two structures, namely dot and honeycomb, were designed (Figure 2) to demonstrate the suitability of the identified parameters. The dimensions of each structure are listed in Table 7. For the dot structure, the basic dimensions are the depth (H) and diameter determined by the spot diameter (D) and pitch (R).

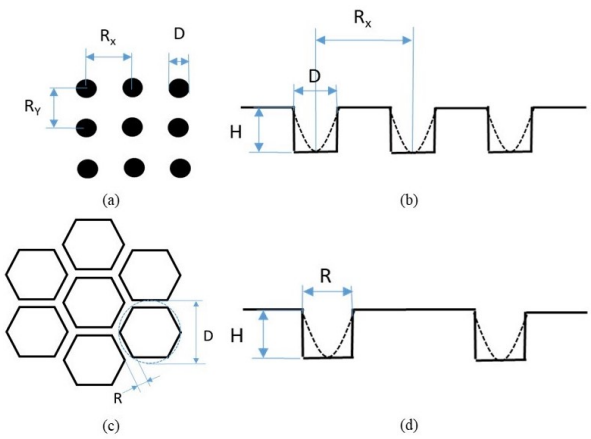

FIGURE 2. Schema of designed surface structures with basic dimension: a) dot structure – view from top; b) dot structure –cros-section profile; c) honeycomb structure – view from top; d) honeycomb structure – cros-section profile.

Structure type	H [µm]	D [µm]	R, Rx, Ry [µm]
Dot	10	35	100
Honeycomb	10	150	35

TABLE 7. Structure dimensions, depth (H), diameter (D), dot pitch (Rx, Ry) and line width of honeycomb structure (R). All values are given in micrometre.

This is the same for the honeycomb structure, where parameter D is defined as the circumscribed circle of one of the hexagons. Pitch (R) for the honeycomb is given by the spot diameter.

4. Results and discussions

4.1. Effect of hatching angle on surface roughness

Before the main experiments, the effect of the hatching angle on surface roughness was estimated. Stainless steel was only one material used for this experiment. The results of the surface roughness measurements for different hatching angles φ obtained from the pre-experiment can be found in Figure 3. The hatching angle $\varphi = 17°$ had the lowest impact on surface roughness and was, therefore, chosen for the subsequent experiments. The highest surface roughness of $Sa = 1.06$ µm was measured for a hatching angle of 45°; it is 1.5 times higher than for an angle of 17°.

4.2. Ablation threshold

The ablation threshold measurement was done for 10 pulses in one place due to the correlation with the following experiments, where an overlap of 90 % was used. Found values are displayed in Figure 4.

The lowest ablation thresholds were generally found for the third harmonics used. This result supports the fact that with decreasing wavelength, photon energy increases [27]. The threshold fluences were found to be

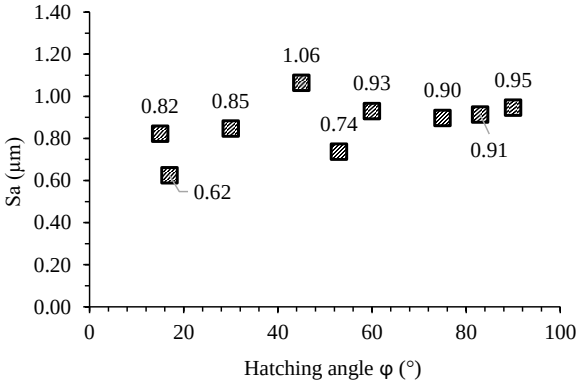

FIGURE 3. The effect of the hatching angle on surface roughness expressed by Sa [µm].

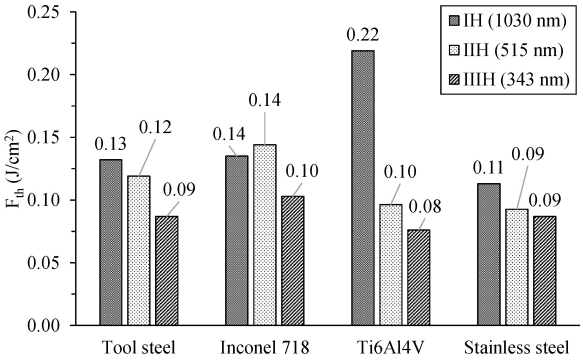

FIGURE 4. The values of ablation threshold for tested materials and wavelengths.

similar for all the materials except for Ti6Al4V with the first harmonic, where the highest threshold value of all the materials was measured. Obtained values were compared with the values found in the literature; see Table 8. Mostly the F_{th} for N=1 or N=100 pulses can be found. Similarities between measured and literature values can be seen for F_{th} (100). The threshold for one pulse ablation is usually much higher than for higher pulse counts. The literature review also confirmed that, for the first harmonic used, titanium alloy should have the highest F_{th} of the studied materials.

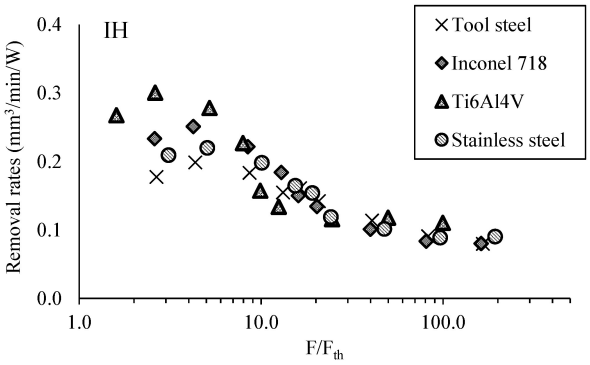

(A). IH (1030 nm)

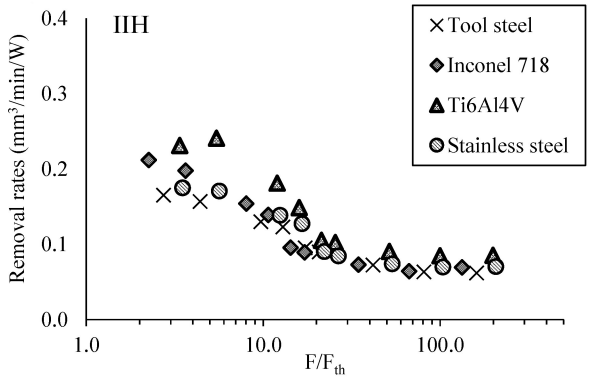

(B). IIH (515 nm)

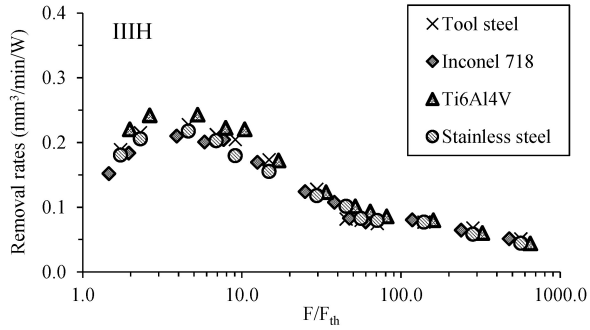

(C). IIIH (343 nm)

FIGURE 5. The removal rates for tested materials and three harmonic wavelengths.

4.3. REMOVAL EFFICIENCY

Using the ablation threshold values, the removal rate dependences were plotted (Figure 5). A logarithmic x-axis with F/F_{th} ratio was used for a better data reproduction. All plot dependences had similar behaviour, reported by [6], reaching a maximum for $e^2 \times F_{th}$, then decreasing and staying constant for a higher F/F_{th} ratio.

The highest removal rates were found for Ti6Al4V titanium alloy for all three harmonics, especially for IH (Figure 5a) where the removal rates reached $\delta V/P_{avg} = 0.3\,\mathrm{mm^3/min/W}$. A possible explanation of this fact may be related to the material's thermal properties. Ti6Al4V titanium alloy had the lowest thermal conductivity (6.7–7.3 $\mathrm{W/m\,K^{-1}}$) of the tested materials. The thermal conductivity coefficient describes the ability of a material to transfer or conduct heat [32]. While, the lowest removal rates were found for tool steel, especially for the optimal F/F_{th} ratio. The thermal conductivity of tool steel is the highest of all the tested materials. The relationship between thermal conductivity and the removal rates is obvious. Even though femtosecond laser irradiation is a cold ablation process, some heat is produced, especially for fluences higher than the ablation threshold. The produced heat is transferred to the lattice. Therefore, for the high thermal conductivity coefficient, a large amount of heat is transferred to the lattice, meaning

Material	Laser wavelength pulse duration	F_{th} (1) [J/cm²]	F_{th} (100) [J/cm²]	Ref.
Ti6Al4V	800 nm, 30 fs	0.29	-	[9]
Ti6Al4V	790 nm, 130 fs	0.272	0.142	[28]
pure Ti	775 nm, 150 fs	0.28	0.08/1.41	[8]
AISI 316L	800 nm, 260 fs	0.21	-	[9]
AISI 304	800 nm, 260 fs	0.24	-	[15]
AISI 316	775 nm, 150 fs	0.21	0.13	[8]
AISI 304	1064 nm, 10 ps	0.5	0.1	[29]
AISI 316	1030 nm 170 fs	0.15	0.135 (50 p)	[14]
AISI 316	1030 nm, 515 nm, 10 ps	0.26 (1030), 0.15 (515 nm)	-	[5]
AISI 304L	800 nm, 100 fs-4,5 ps	0.02-0.05	-	[30]
AISI 304	775 nm, 150 fs	0.16	-	[19]
HR4 nickel alloy, alloy 115	800 nm, 100 s	0.377	0.152	[31]

TABLE 8. Literature review of the fluence threshold values $F_{th}(1)$ and $F_{th}(100)$.

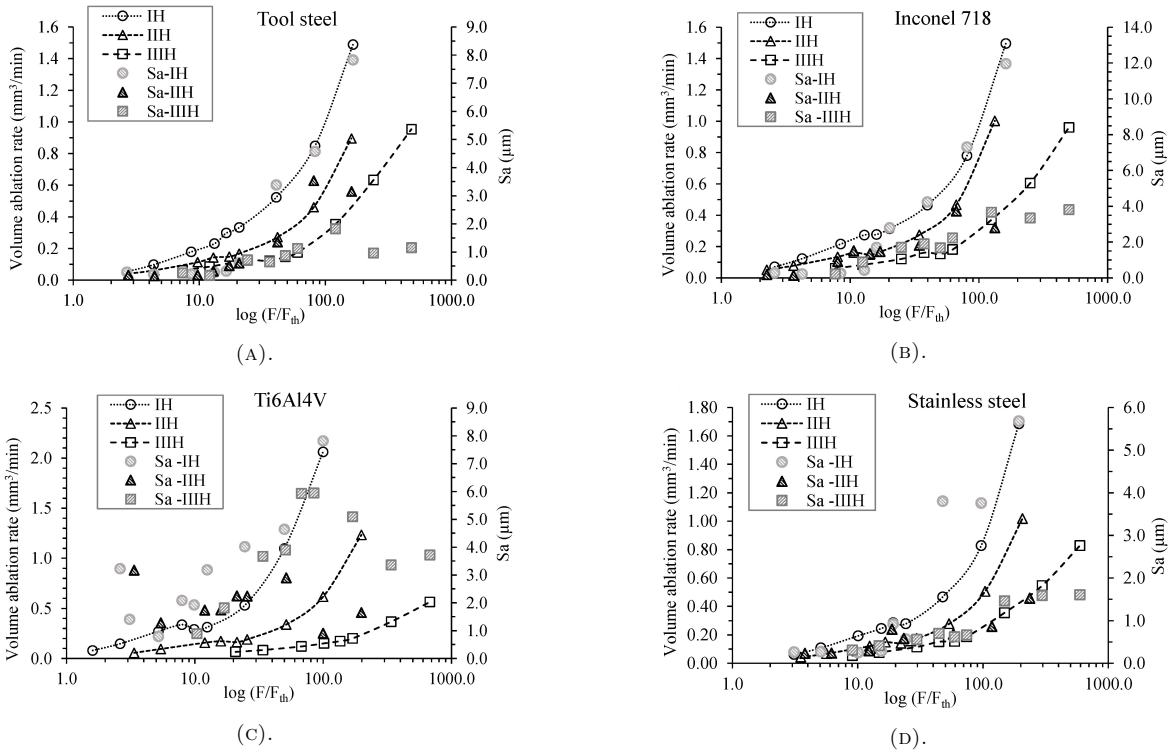

FIGURE 6. Volume ablation rate and surface roughness (Sa) dependency on the laser fluence.

a low amount of heat to melt and ablate the material. As a result, materials with high thermal conductivity are more difficult to ablate by laser.

However, very minor differences in removal rates were found for IIIH (Figure 5c). As reported by [18], material absorptivity, especially for metals, increases with shorter wavelengths. In addition, at shorter wavelengths, the laser energy is absorbed in a smaller volume of material, which localises the heated interaction region. Thus, the possibility of thermal conduction is reduced.

A limit of the removal rate parameter is its focus on process effectivity. In spite of this fact, the volume ablation rate parameter could be useful for describing processes that need higher material ablation without regard to energy consumption. However, negative effects can occur, e.g. heat affection and increased surface roughness. Therefore, a compromise between the ablation rate and surface roughness needs to be found. An ideal example can be seen in Figure 6a for tool steel. For the achieved $\Delta V = 1\,\mathrm{mm}^3/\mathrm{min}$, an ideal solution is to use IIIH, which demonstrated the lowest surface roughness (Sa = 1.1 µm), much lower than for IH (Sa = 4.5 µm) and IIH (Sa = 3.1 µm) for the same volume ablation rate. Similar behaviour was also observed for tool steel (Figure 6a) using IIIH, where Sa remains constant even for higher fluences. For stainless steel (Figure 6d), the Sa values achieved for IIH were lower than for IIIH and much lower than for IH. A very specific behaviour in comparison with the other materials was found for Ti6Al4V (Figure 6c). The lowest Sa was measured for IIH, much lower

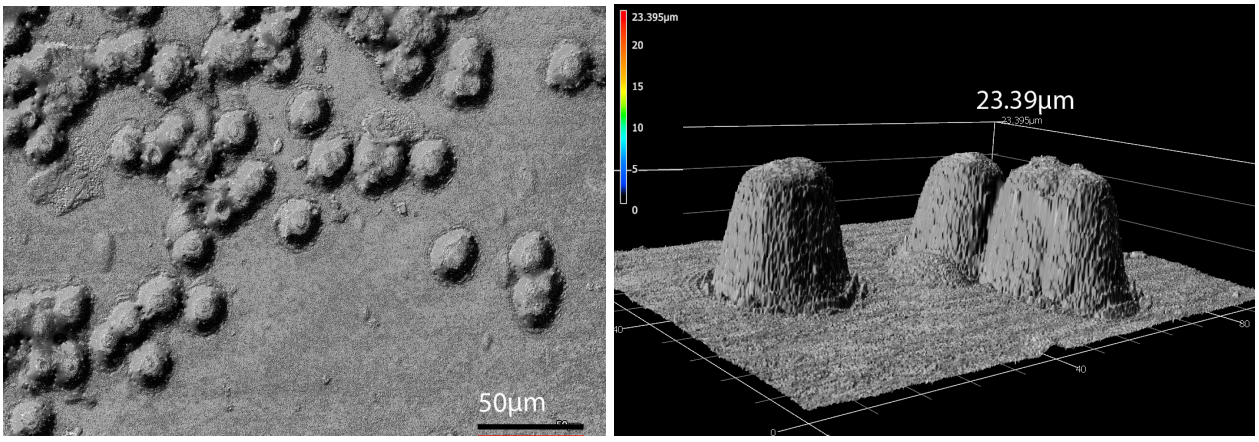

Figure 7. a) 2D image of cone-like features formed on lasered Ti6Al4V surface, b) 3D image of cone-like features.

than for IH and also for IIIH. Moreover, for IIIH, the maximum volume ablation rate was the lowest of all the tested materials. However, for IH, the maximum ($\Delta V = 2.06$ mm^3/min) was achieved in comparison with the other materials, with a very high Sa of 8 µm due to significant thermal effects. High surface melting was observed for all the materials for higher fluences. The highest Sa was measured for Inconel 718, reaching Sa $\approx$ 12 µm.

For Ti6Al4V (Figure 6c), an increase in surface roughness was observed for low fluences, especially for IH and IIH. Optical inspection of ablated areas was done by optical and confocal microscopes. Examples of different ablated materials with same used wavelength and fluence can be seen in Appendix A Figure 11 detailed inspection of the Ti6Al4V surface, for F=0.5 J/cm^2 and IIH used, revealed some debris, see Figure 7. These elements covered the whole lasered surface at a height of about 25 µm. As published by [33], cone-like features form due to material redeposition and the thermal effects of fluences ranging from $F = 0.49$–0.86 J/cm^2. For higher fluences, some micro-cracks start to form. The same results were found in our study. Formation of cone-like features can be limited by using IIIH, probably due to the higher energy of incoming photons along with a higher material absorption.

4.4. Increasing scanning speed and repetition rates

In this paper, the method of increasing the repetition rate for increasing process productivity was chosen. The laser system used allows us to use a 1 MHz repetition rate with a maximum output power of 40 W with a scanning speed of more than 5 m/s. For this reason, the repetition rate was tested across the entire adjustable spectrum from 100 kHz to 1 MHz. The same fluence, which was found to be optimal in the previous experiments, was used, recalculated to the applied repetition rate. The optimal fluence values are shown in Table 9.

Material	F_{opt} **[J/cm^2]**
Stainless steel	0.57
Tool steel	0.57
Inconel 718	0.57
Ti6Al4V	0.45

Table 9. Optimal fluences obtained from removal efficiency experiment for 200 kHz used for increasing scanning speed experiment.

In Figure 8c, the volume ablation rates in relation to the repetition rate are displayed. As expected, the productivity of the process increases by increasing the repetition rate or scanning speed. To demonstrate the inclination of increase, trendlines were used. The highest angle of inclination can be seen for Ti6Al4V. It shows the highest productivity gains. The volume ablation rates increase more than five-fold when the repetition rate is changed from 200 kHz to 1 MHz. However, surface roughness increases slightly for scanning speeds higher than 4000 mm/s (in Figure 8a). This is due to high acceleration and deceleration angles on the short track in combination with the limits of the scanning head that was used. As can be seen from Figure 8b, the removed depth remains constant as the repetition rate and scanning speed increase, respectively. This experiment proved that using a higher repetition rate is beneficial for process productivity. The plots in Figure 8 also demonstrate the ability of the materials to be ablated by laser. The highest removed depth was measured for Ti6Al4V along with the greatest surface roughness caused by significant melting and redeposition of debris as presented for 200 kHz. The steel materials show the lowest removed depth with low surface roughness, comparable to Inconel 718. While, the removed depth was significantly higher for Inconel 718 than for both of the steel materials.

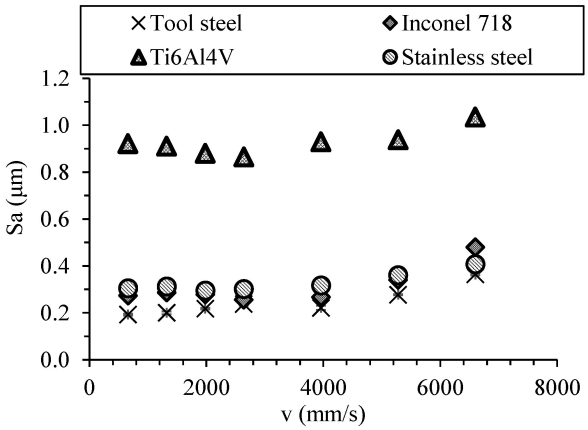

(A). Surface roughness.

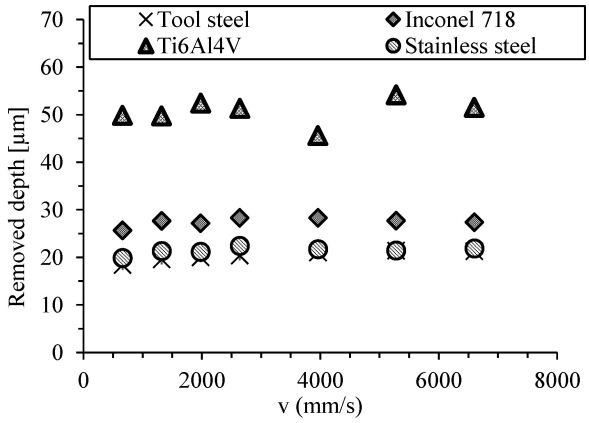

(B). Removed depth.

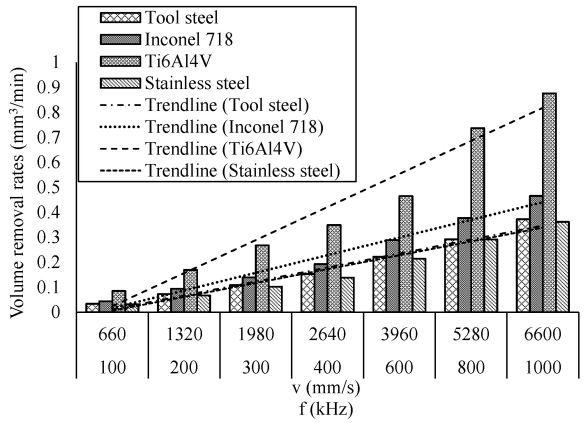

(C). Volume removal rates.

FIGURE 8. Increasing scanning speed results.

4.5. SURFACE STRUCTURING

Using the maximal repetition rate and scanning speed is useful in regard to high process productivity. Some scanning problems can appear during high scanning speeds, such as acceleration and deceleration for short tracks. Even when the sky-writing function developed by galvo-scanner provider SCANLAB GmbH company is used, it is best to use a scanning speed below 4 m/s, especially for geometrically complex structures. The sky-writting function uses predictive algorithms for eliminating acceleration and deceleration of the galvo-scanner mirrors. Two different structures were chosen for the demonstration of the developed processing parameters, namely dot and honeycomb structures. The dot structure was fabricated using a different number of pulses in one place with a defined fluence.

The honeycomb structure was based on a CAD model. The laser beam moved through the lines defined by the model. Both structures had a similar depth of H = 10 µm. The results of the dot structure measurement are presented in the Table 10. Structure depth, diameter and line width were measured from 10 profile lines across the sample. The shape of the fabricated dots was good without material ejection over the edge of the crater. All the dots also had a very good circularity and the proposed depth was achieved. The honeycomb structure also achieved good compliance with the proposed dimensions; see Table 11. A repetition rate of 600 kHz and scanning speed of 3.9 m/s were used for structuring with fluences ranging from $F = 1.27$ to $1.84\,\mathrm{J/cm^2}$ according to the fabricated material. The proposed depth was achieved by a defined number of repetitions ranging from 24 to 28. A very precise structure depth can be obtained with this strategy, with a deviation of only a few tens of micrometre. An example of a 2D view and depth profile of the dot structure for each material can be seen in Appendix A Figure 10 and for the honeycomb structure in Appendix A Figure 11. The designed and fabricated structures have the potential to improve friction properties of materials by decreasing the coefficient of friction as reported by [34]. Structured surfaces can be beneficial in moving mechanical components made from advanced materials such as mechanical seals, piston rings or thrust bearings.

5. CONCLUSIONS

Based on the observations of the current study, the following conclusions can be drawn:

- The ideal hatching angle was found in the pre-experiment. A hatching angle of 17° had the lowest impact on surface roughness. Using odd hatching angles has the advantage that the laser beam never scans twice in the same path.
- The ablation threshold was measured for all the materials using three harmonic wavelengths. The highest fluence threshold value was found for Ti6Al4V titanium alloy when using the first harmonic (1030 nm). Conversely, using the third harmonic (343 nm) led to the lowest ablation thresholds due to the high energy of the incoming photons.
- The highest ablation rates were obtained for Ti6Al4V, especially for IH and IIH, because Ti6Al4V had the lowest thermal conductivity of all the tested materials. For higher F/F_{th} ratio, the differences become smaller. However, the surface roughness expressed by Sa [µm] was the highest of all the materials. Also, some cone-like structures

Material	F [J/cm^2]	Number of pulses [-]	H [µm]	D [µm]
Tool steel	0.573	250	10.37 ± 0.31	28.5 ± 0.77
Inconel 718	0.573	210	10.17 ± 0.23	29 ± 0.73
Ti6Al4V	0.456	180	9.77 ± 0.19	28 ± 0.65
Stainless steel	0.573	260	10.18 ± 0.28	28.4 ± 0.82

Table 10. Laser parameters used for dot structure fabrication with measured results of hole depth (H) and diameter (D).

Material	F [J/cm^2]	Number of pulses [-]	S_x, H_y [%]	H [µm]	R [µm]
Tool steel	1.56	26	90	9.56 ± 0.22	33.5 ± 0.52
Inconel 718	1.56	24	90	9.57 ± 0.25	36 ± 0.65
Ti6Al4V	1.27	24	90	10.14 ± 0.34	31.3 ± 0.47
Stainless steel	1.84	28	90	10.2 ± 0.18	37.1 ± 0.84

Table 11. Laser and scanning parameters used for honeycomb structure fabrication with measured results of structure depth (H) and line width (R).

formed on the lasered surfaces for lower fluences. These effects can be eliminated by using IIIH.

- For IIIH, the differences between the ablation behaviour of all the materials were negligible. For shorter wavelengths, the absorptivity of metals increases and at the same time, the effect of thermal conductivity decreases.
- The experiment for increasing productivity was successful. It was proved that the productivity can be increased more than five-fold. At the same time, a higher scanning speed did not have a negative effect on the surface roughness or removed depth.
- A demonstration of the identified parameters was presented in fabrication of two different complex structures. Good shape and circularity were obtained for the dot structure, along with compliance with the proposed depth of the structure. Simultaneously, the honeycomb structure was fabricated according to the proposal with a good optical quality. Both structures had the potential to improve friction properties of advanced materials.

The presented study summarises and compares the ablation behaviour of four advanced materials and gives a complete overview of the findings of basic ablation parameters for a complex shape structure production by femtosecond laser.

List of symbols

λ Wavelength [nm]
F Fluence [J/cm^2]
F_{th} Threshold fluence [J/cm^2]
E_p Pulse energy [J]
τ Pulse duration [ps, fs]
f Repetition rate [kHz]
M^2 Laser beam quality [–]
S_x Pulse overlap in scanning direction [%]
H_y Pulse overlap in traverse direction [%]
φ Hatching angle [°]
δ Optical penetration depth [nm]

Acknowledgements

This work was supported by the Grant Agency of the Czech Technical University in Prague, grant no. SGS22/159/OHK2/3T/12 and no. SGS22/158/OHK2/3T/12.

References

[1] K. Sugioka. Progress in ultrafast laser processing and future prospects. *Nanophotonics* **6**(2):393–413, 2017. https://doi.org/10.1515/nanoph-2016-0004.

[2] N. Hodgson, A. Steinkopff, S. Heming, et al. Ultrafast laser machining: process optimization and applications. *Laser Applications in Microelectronic and Optoelectronic Manufacturing (LAMOM) XXVI* **11673**:1167308, 2021. https://doi.org/10.1117/12.2584178.

[3] K. Ahmmed, C. Grambow, A.-M. Kietzig. Fabrication of micro/nano structures on metals by femtosecond laser micromachining. *Micromachines* **5**(4):1219–1253, 2014. https://doi.org/10.3390/mi5041219.

[4] J. Bonse, S. Kirner, M. Griepentrog, et al. Femtosecond laser texturing of surfaces for tribological applications. *Materials* **11**(5):801, 2018. https://doi.org/10.3390/ma11050801.

[5] P. Lickschat, D. Metzner, S. Weißmantel. Fundamental investigations of ultrashort pulsed laser ablation on stainless steel and cemented tungsten carbide. *The International Journal of Advanced Manufacturing Technology* **109**(3-4):1167–1175, 2020. https://doi.org/10.1007/s00170-020-05502-8.

[6] B. Jaeggi, B. Neuenschwander, M. Schmid, et al. Influence of the pulse duration in the ps-regime on the ablation efficiency of metals. *Physics Procedia* **12**:164–171, 2011. https://doi.org/10.1016/j.phpro.2011.03.118.

[7] V. Stankevič, A. Čermák, S. Mikalauskas, et al. Processing of ultra-hard materials with picosecond pulses: From research work to industrial applications. *Journal of Laser Applications* **30**(3):032202, 2018. https://doi.org/10.2351/1.5040633.

[8] P. Mannion, J. Magee, E. Coyne, et al. The effect of damage accumulation behaviour on ablation thresholds and damage morphology in ultrafast laser micro-machining of common metals in air. *Applied Surface Science* **233**(1-4):275–287, 2004. https://doi.org/10.1016/j.apsusc.2004.03.229.

[9] S. Xu, Y. Chen, H. Liu, et al. Femtosecond laser ablation of Ti alloy and Al alloy. *Optik* **212**:164628, 2020. https://doi.org/10.1016/j.ijleo.2020.164628.

[10] P. Lickschat, A. Demba, S. Weissmantel. Ablation of steel using picosecond laser pulses in burst mode. *Applied Physics A* **123**(2):123–137, 2017. https://doi.org/10.1007/s00339-016-0743-y.

[11] M. Domke, V. Matylitsky, S. Stroj. Surface ablation efficiency and quality of fs lasers in single-pulse mode, fs lasers in burst mode, and ns lasers. *Applied Surface Science* **505**:144594, 2020. https://doi.org/10.1016/j.apsusc.2019.144594.

[12] P. Hauschwitz, R. Bičštová, A. Brodsky, et al. Towards rapid fabrication of superhydrophobic surfaces by multi-beam nanostructuring with 40,401 beams. *Nanomaterials* **11**(8), 2021. https://doi.org/10.3390/nano11081987.

[13] J. Finger, C. Kalupka, M. Reininghaus. High power ultra-short pulse laser ablation of IN718 using high repetition rates. *Journal of Materials Processing Technology* **226**:221–227, 2015. https://doi.org/10.1016/j.jmatprotec.2015.07.014.

[14] J. Schille, A. Heisterkamp, J. Neev, et al. High repetition rate femtosecond laser processing of metals. *Proceedings SPIE: Ultrafast Optics: Biomedical, Scientific, and Industrial Applications X* **7589**:758915, 2010. https://doi.org/10.1117/12.842600.

[15] S. Xu, R. Ding, C. Yao, et al. Effects of pulse durations and environments on femtosecond laser ablation of stainless steel. *Applied Physics A* **124**:310, 2018. https://doi.org/10.1007/s00339-018-1714-2.

[16] X. Sedao, M. Lenci, A. Rudenko, et al. Influence of pulse repetition rate on morphology and material removal rate of ultrafast laser ablated metallic surfaces. *Optics and Lasers in Engineering* **116**:68–74, 2019. https://doi.org/10.1016/j.optlaseng.2018.12.009.

[17] G. Çam, G. İpekoğlu, K.-H. Bohm, M. Koçak. Investigation into the microstructure and mechanical properties of diffusion bonded TiAl alloys. *Journal of Materials Science* **41**(16):5273–5282, 2006. https://doi.org/10.1007/s10853-006-0292-4.

[18] M. Henry, P. M. Harrison, I. Henderson, et al. Laser milling: a practical industrial solution for machining a wide variety of materials. *Proceedings of the SPIE* **5662**:627–632, 2004. https://doi.org/10.1117/12.596743.

[19] P. Mannion, T. J. Glynn, J. Magee, et al. Ablation thresholds in ultrafast laser micromachining of common metals in air. *Proceedings SPIE: Opto-Ireland 2002: Optics and Photonics Technologies and Applications* **4876**:470–478, 2003. https://doi.org/10.1117/12.463744.

[20] HASCO company. Material characteristics – 1.2379. [2022-08-04], https://www.hasco.com/en/werkstoffdatenblatt_1.2379.

[21] A. S. Hakeem, F. Patel, N. Minhas, et al. Comparative evaluation of thermal and mechanical properties of nickel alloy 718 prepared using selective laser melting, spark plasma sintering, and casting methods. *Journal of Materials Research and Technology* **12**:870–881, 2021. https://doi.org/10.1016/j.jmrt.2021.03.043.

[22] NeoNickel. (2021) Data sheet – alloy 718. [2022-08-04], https://www.neonickel.com/alloys/nickel-alloys/alloy-718/.

[23] Material-properties.org. (2022) About grade 5 titanium alloy – Ti-6Al-4V. [2022-08-04], https://material-properties.org/ti-6al-4v-density-strength-hardness-melting-point/.

[24] AZoNetwork. (2001) AZo materials, stainless steel – Grade 316 (UNS S31600), datasheet. [2022-08-04], https://www.azom.com/properties.aspx?ArticleID=863.

[25] C. Daniel, J. Manderla, S. Hallmann, C. Emmelmann. Influence of an angular hatching exposure strategy on the surface roughness during picosecond laser ablation of hard materials. *Physics Procedia* **83**:135–146, 2016. https://doi.org/10.1016/j.phpro.2016.08.026.

[26] International Organization for Standardization. *ISO 25178-2:2021, Geometrical product specifications (GPS) – Surface texture: Areal – Part 2: Terms, definitions and surface texture parameters, second edition*, 2021.

[27] M. D. Shirk, P. A. Molian. A review of ultrashort pulsed laser ablation of materials. *Journal of Laser Applications* **10**(1):18–28, 1998. https://doi.org/10.2351/1.521827.

[28] N. Maharjan, W. Zhou, Y. Zhou, Y. Guan. Ablation morphology and ablation threshold of Ti-6Al-4V alloy during femtosecond laser processing. *Applied Physics A* **124**(8):519, 2018. https://doi.org/10.1007/s00339-018-1928-3.

[29] G. Raciukaitis, C. R. Phipps, M. Brikas, et al. Accumulation effects in laser ablation of metals with high-repetition-rate lasers. *Proceedings SPIE: High-Power Laser Ablation VII* **7005**:70052L, 2008. https://doi.org/10.1117/12.782937.

[30] R. Le Harzic, D. Breitling, M. Weikert, et al. Pulse width and energy influence on laser micromachining of metals in a range of 100fs to 5ps. *Applied Surface Science* **249**(1-4):322–331, 2005. https://doi.org/10.1016/j.apsusc.2004.12.027.

[31] T. L. See, Z. Liu, H. Liu, et al. Effect of geometry measurements on characteristics of femtosecond laser ablation of HR4 nickel alloy. *Optics and Lasers in Engineering* **64**:71–78, 2015. https://doi.org/10.1016/j.optlaseng.2014.07.011.

[32] Z. Pluta, T. Hryniewicz. Thermal expansion of solids. *Journal of Modern Physics* **3**(8):793–802, 2012. https://doi.org/10.4236/jmp.2012.38104.

[33] G. Schnell, H. Lund, S. Bartling, et al. Heat accumulation during femtosecond laser treatment at high repetition rate – a morphological, chemical and crystallographic characterization of self-organized structures on Ti6Al4V. *Applied Surface Science* **570**:151115, 2021. https://doi.org/10.1016/j.apsusc.2021.151115.

[34] M. Bieda, C. Schmädicke, T. Roch, A. Lasagni. Ultra-low friction on 100Cr6-steel surfaces after direct laser interference patterning. *Advanced Engineering Materials* **17**(1):102–108, 2015. https://doi.org/10.1002/adem.201400007.

A. Appendices

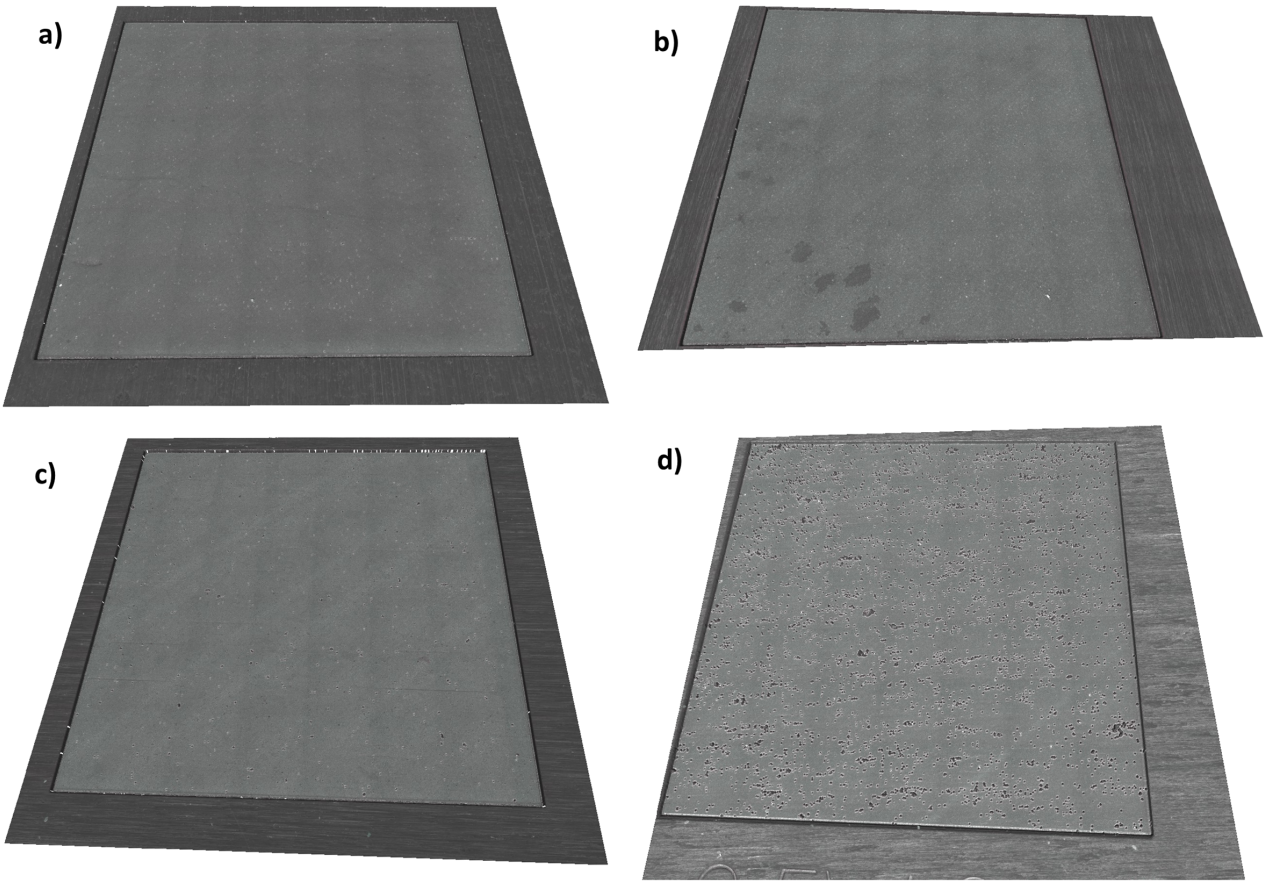

Figure 9. 3D images of ablated materials a) tool steel; b) stainless steel; c) Inconel 718; d) Ti6Al4V, using IIH and $F = 0.52\,\mathrm{J/cm^2}$.

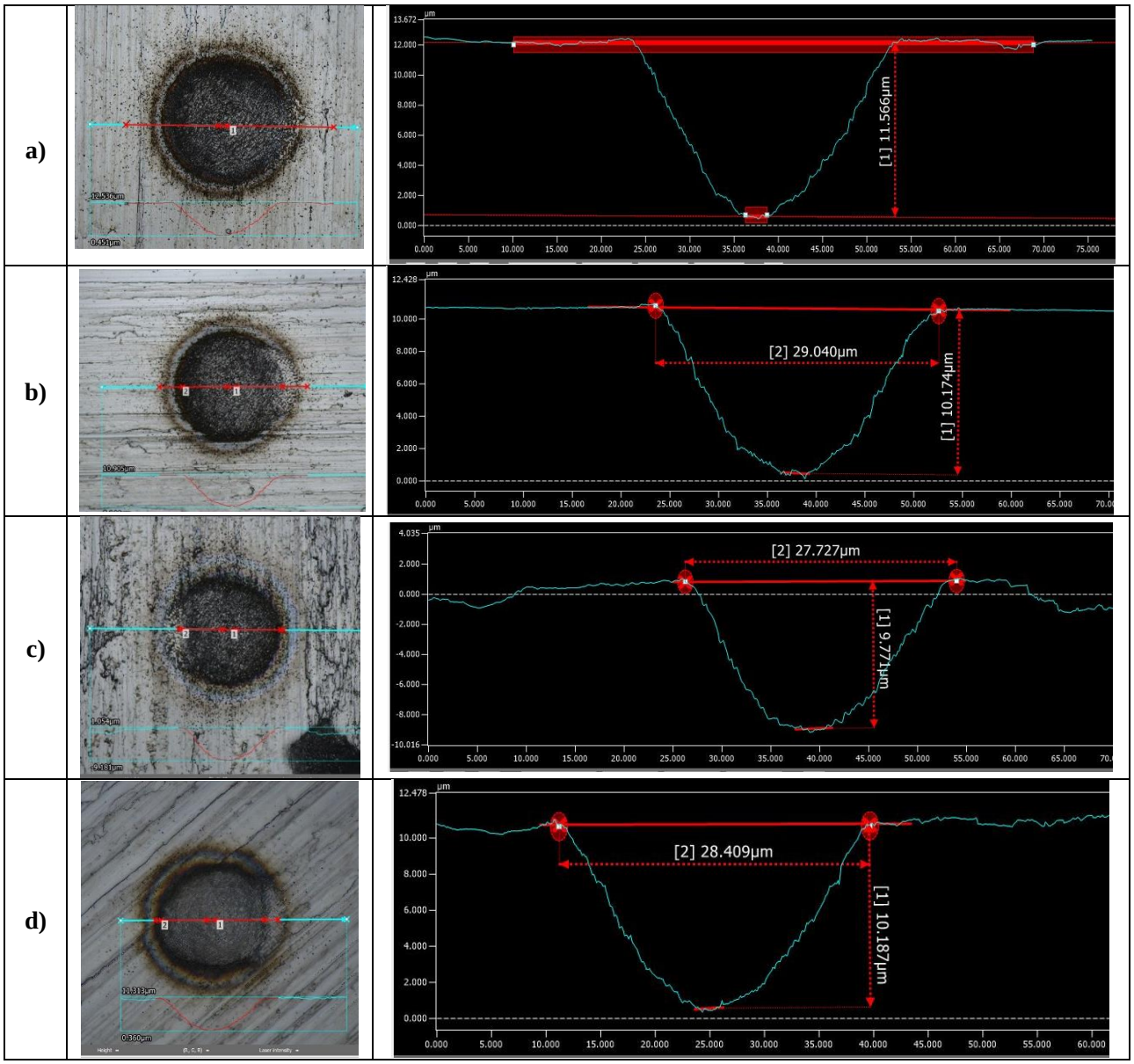

Figure 10. Examples of the dot structure fabricated in the tested materials: left – 2D image, right – depth profile, a) Tool steel; b) Inconel 718; c) Ti6Al4V; d) Stainless steel.

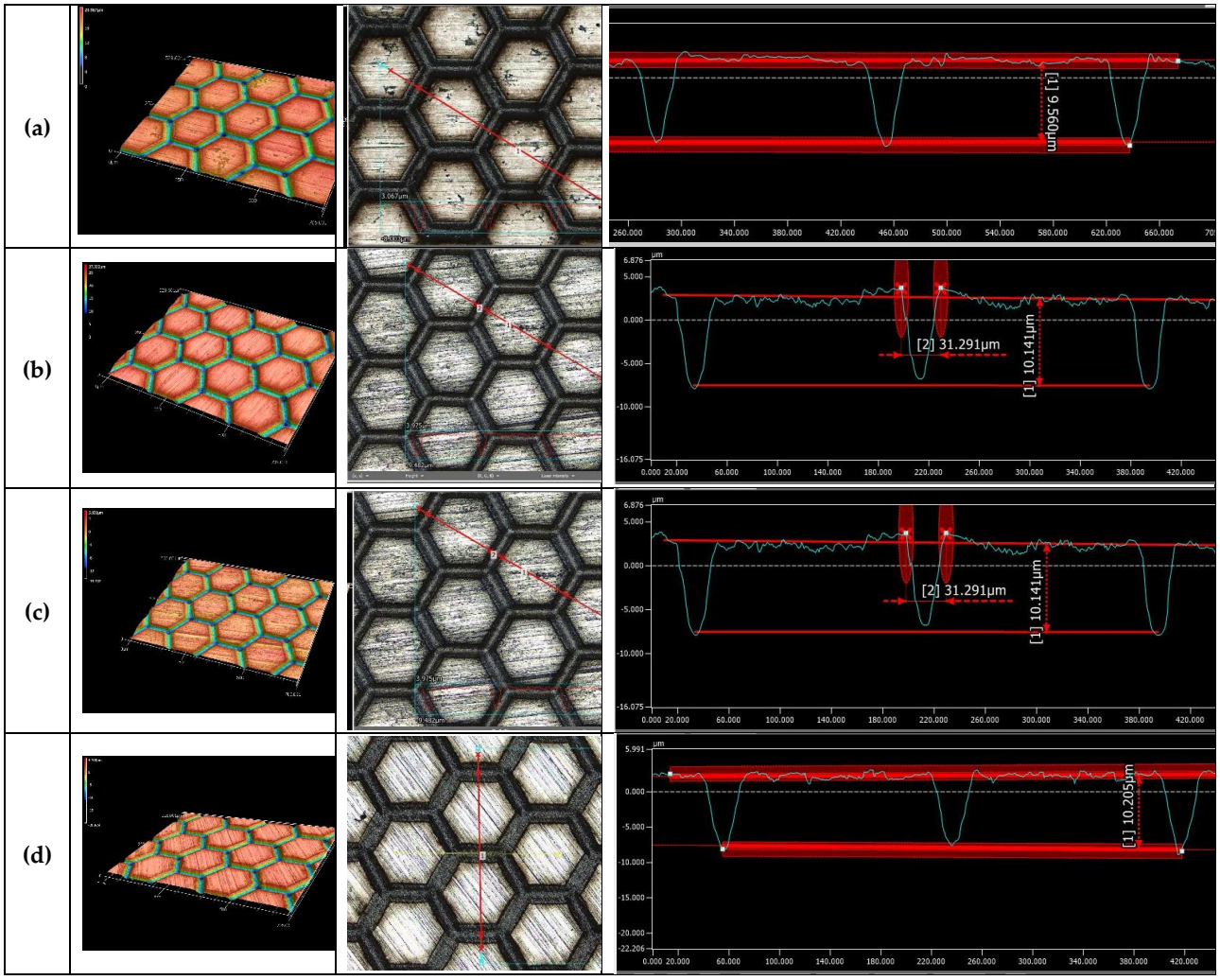

FIGURE 11. Examples of the honeycomb structure fabricated in the tested materials: left – 3D image, right – depth profile, a) Tool steel; b) Inconel 718; c) Ti6Al4V; d) Stainless steel.

COMPARATIVE STUDY OF STATE SPACE AVERAGING AND PWM WITH EXTRA ELEMENT THEOREM TECHNIQUES FOR COMPLEX CASCADED DC-DC BUCK CONVERTER

Sangeeta Shete*, Prasad Joshi

Shivaji University, Government College of Engineering, Department of Electrical Engineering, Karad, Maharashtra, India

* corresponding author: sangeetashete2019@gmail.com

Abstract. Until now, most commonly used state space averaging and PWM techniques have been applied to different converter topologies and their advantages and disadvantages were stated. However, the superiority of an analytical technique was not justified based on a parametric comparison of these techniques for the same converter topology. Hence, in this paper, first time a comparative evaluation of two commonly used modelling techniques for fourth order converter is presented. The first approach makes use of a state-space averaging of the converter and is based on analytical manipulations using different state representations of the converter. The second approach is based on PWM switch modelling with an extra element theorem and consists of topological manipulations. The two modelling techniques are applied to the same complex cascaded DC-DC Buck converter and a transfer function is obtained. These techniques are compared for different features and the study concludes that state space modelling technique is systematic and less complicated than PWM switch modelling with an extra element theorem for a higher order converter.

Keywords: Analytical technique, cascaded DC-DC Buck converter, state space averaging, PWM switch modelling, extra element theorem, transfer function.

1. Introduction

Analytical techniques play a vital role in analysing the behaviour of converters under different conditions, performance improvements and design aspects. DC-DC converters have a high number of components and nonlinear behaviour due to the existence of a switch and diode in circuit, which makes them complex in nature. A study of dynamic behaviour and assessment of stability of such nonlinear and complex circuits is a very challenging job. Article [1] presented the review of existing analytical techniques in a structured and meaningful manner and stated that the circuit averaging (CA), state space averaging (SSA), and PWM switch modelling are most commonly used analytical techniques, whereas signal flow graphs, energy factor, switching function, S-Z method are special techniques. SSA is an organised method which allows the inclusion of parasitic elements of a circuit even in the initial stage, permits to explore a linear system with a zero initial condition and nonlinear systems with all initial conditions [2–4]. It is preferred to design a robust controller. However, as it doesn't consider switching frequency in the analysis, this technique is applied by neglecting the ripple effect on inductor current and output voltage [5, 6], which affects its accuracy [7–9]. State space representation is used for mathematical modelling of SEPIC converter, which is further used to contrivance the controller. The results of PI controls and hysteresis controls are compared using PSIM software [10]. The PWM switch modelling technique employs determination of invariant properties of the PWM switch to obtain the average model of circuit and small signal characteristics can be obtained from this average model [11]. PWM technique with conventional approach is simple and pedagogical approach of analysis and provides complete information about steady state and dynamic properties of the converter. This approach is also useful for frequency domain analysis and quasi resonant converters. PWM technique using Extra Element Theorem (EET) is more efficient and practical for general circuits, as it leads to a faster analysis due to a reduced mathematical manipulation, meaningful form of expressions and it is easy to track the errors [12].

An enormous study has been conducted regarding SSA and PWM switch modelling techniques for converters. Article [2] investigated dynamic modelling of Zeta converter, wherein transfer functions, bode plot, transient response and steady state response were obtained using MATLAB and PSPICE. Article [13] obtained state equations and output equations using SSA technique for Buck, Boost and Buck-Boost converter and observed that the state space model simulation results are comparable with a hardware model with a deviation of only 0.0015 V. However, this technique doesn't simulate ripple effect of inductor current and output voltage due to the absence of switching frequency. Article [14] analysed SEPIC converter using an average state-space modelling approach taking into account power losses in converter elements and concluded that this methodology

contributes for converter design as per the requirements and reduces the need for accurate time domain simulations. Mathematical modelling of DC-DC Buck converter using state space averaging and validation of the models was performed using PSIM and MATLAB Simulink [15]. The studies were performed for state space small signal modelling of a double Boost converter integrated with SEPIC converter [3, 16, 17], and SEPIC converter with coupled and uncoupled inductor [18]. Book [19] presented the well-defined and systematic process of small signal analysis of nonlinear circuits using state space analysis to determine the control to output transfer function. The concepts and mathematical modelling of circuits using EET [20] and PWM with EET [21] were studied. The output impedances of three PWM DC-DC converters were analysed in a general and unified manner using PWM switch modelling with EET technique [22]. Article [23] presented the effect of an input filter interaction in the small signal analysis of voltage and current control mode of DC-DC Boost converter and concluded that the methodology is universally adopted. MATLAB Simulink was employed to study the output voltage for multiple DC-DC converters [24] and Boost converter [25].

Article [12] presented PWM with EET to a general circuit and concluded that it is a fast analytical technique which produces a well-ordered polynomial and low entropy form of transfer functions. However, by applying this technique to a complex SEPIC converter, the study concluded that as the circuit becomes complicated, a conventional node and mesh analysis is better instead of the PWM with EET. Nevertheless, the basis of comparison for this statement is not presented in the study, and therefore it is necessary to study the features of PWM with EET technique for higher order circuits. Some of the existing studies have developed the analytical models, obtained simulation results and commented on advantages, disadvantages and applications in a relative manner without comparing the results with a counterpart technique, which doesn't fit into the acceptable scientific and technical approach. The advantages, disadvantages and superiority of a technique should be based on a comparison of two or more techniques for the same converter topology. Even though numerous studies regarding SSA and PWM with EET techniques for different converters have been performed, surprisingly no efforts were done to compare these techniques for the same converter and to comment on the superiority of the analytical technique. The past few years have perceived notable development in the research of DC-DC converter topologies. Although the conversion efficiency of a single-stage converter is better than that of the two-stage converter, the quadratic converters are proposed for extremely large range of conversion ratios. As a part of this, complex cascaded Buck converter (CBC) is always preferred for many applications, as it has a better conversion ratio, high voltage step down ratio, and large voltage regulation [26]. Therefore, in this paper, a comparative evaluation of two widely preferred modelling tools for a higher order DC-DC converter is presented. The first approach makes use of a state-space averaged model of the converter based on the analytical manipulations, whereas the second approach is based on the PWM switch modelling with EET technique based primarily on the manipulations of circuits. The two modelling techniques are applied to a same complex cascaded DC-DC Buck converter and are compared on the basis of their various features to decide the superiority for a higher order circuit.

2. Materials and methods

2.1. Complex cascaded DC-DC Buck converter

The existence of two transistor switches of the conventional cascaded Buck converter can be reduced to a single transistor switch in the complex cascade DC-DC Buck converter as shown in Figure 1, which has two inductors and two capacitors making it a fourth-order circuit and has a quadratic conversion ratio of D^2. This single-transistor realisation is the most additional advantage over a straight forward cascade of two basic converters. The switching section consists of one active switch and three diodes. Though the circuit is complex, the conversion ratio of CBC cannot be realised with less than two capacitors, two inductors, and four switches. However, additional complexity of the converter network may compromise the wide conversion ratio. The control strategy of the complex CBC is depicted in Figures 2a and 2b. The ON state and OFF state correspond to the operation of two Buck converters connected in a cascade as depicted in Figure 3.

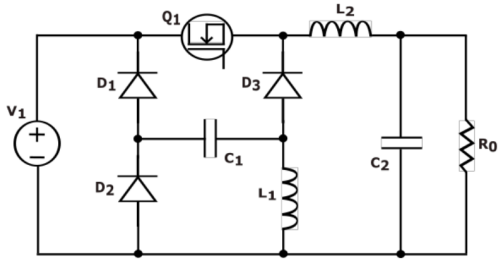

Figure 1. Topology of cascade DC-DC Buck converter.

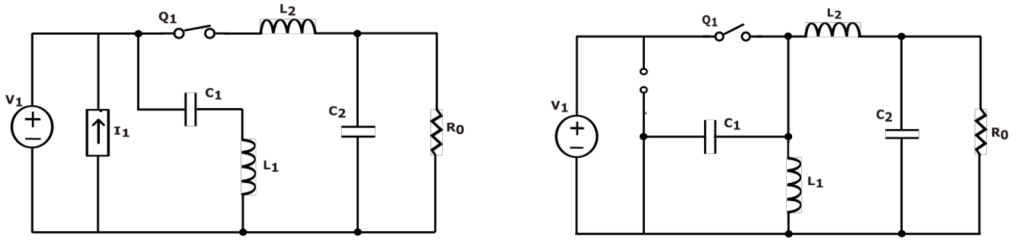

FIGURE 2. Switching mechanism of complex CBC.

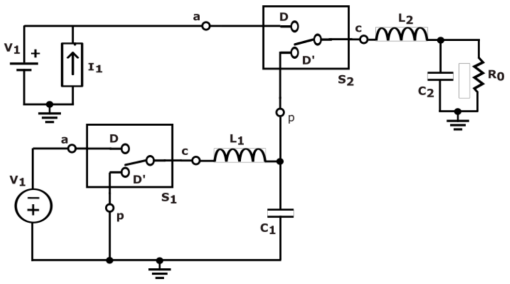

FIGURE 3. Operation of complex CBC.

The total output voltage is given by Equation 1.

$$V_2 = \frac{1}{T}\int_0^T (-DV_1 + DV_1(1+D))\,\mathrm{dt}$$
$$V_2 = D^2 V_1 \tag{1}$$

Where, D is the duty ratio and

$$D^2 = \frac{1}{T}\int_0^T \check{\mathrm{D}}^2(t)\mathrm{dt}$$

The chopper circuit of CBC has one active switch and three passive switches, which are driven by switching function $\check{\mathrm{D}}^2(t)$ and $\check{\mathrm{D}}^{'2}(t)$, respectively. The switching function is given as,

$$\check{\mathrm{D}}^2(t) = \begin{cases} 1 & 0 < t < T_{ON} \\ 0 & T_{ON} < t < T \end{cases}$$

2.2. State space averaging technique

The state-space averaging method is based on analytical operations for the converter states comprising the determination of linear state model for each possible configuration of circuit and subsequently combining all these elementary models into a single and unified one through a duty factor. The method involves a formulation of the state equation for each state, averaging, perturbation and then rearranging equations to obtain the required transfer function by applying Laplace transform. The complex CBC is considered in continuous conduction mode and switch and diodes are considered in ideal mode. Considering, inductor currents I_{L1}, I_{L2}, and capacitors voltages V_{C1} and V_{C2} as the state variables, the state equation and output equation in ON state of the CBC (Figure 2a) are expressed by the Equations 2 and 3.

$$\left.\begin{array}{c} \frac{\mathrm{d}(I_{L1})}{\mathrm{dt}} = \frac{V_1}{L_1} - \frac{V_{C1}}{L_1} \\ \frac{\mathrm{d}(I_{L2})}{\mathrm{dt}} = \frac{V_1}{L_2} - \frac{V_{C2}}{L_2} \\ \frac{\mathrm{d}(V_{C1})}{\mathrm{dt}} = \frac{I_{L1}}{C_1} \\ \frac{\mathrm{d}(V_{C2})}{\mathrm{dt}} = \frac{I_{L2}}{C_2} - \frac{V_2}{RC_2} \end{array}\right\} \tag{2}$$

$$V_2 = V_{C2} \tag{3}$$

Similarly, the state equation and output equation in OFF state of the converter (Figure 2b) are expressed by the Equations (4) and (5).

$$\left.\begin{array}{l} \frac{\mathrm{d}(I_{L1})}{\mathrm{dt}} = -\frac{V_{C1}}{L_1} \\ \frac{\mathrm{d}(I_{L2})}{\mathrm{dt}} = \frac{V_{C1}}{L_2} - \frac{V_{C2}}{L_2} \\ \frac{\mathrm{d}(V_{C1})}{\mathrm{dt}} = \frac{I_{L1}}{C_1} - \frac{I_{L2}}{C_1} \\ \frac{\mathrm{d}(V_{C2})}{\mathrm{dt}} = \frac{I_{L2}}{C_2} - \frac{V_2}{RC_2} \end{array}\right\} \tag{4}$$

$$V_2 = V_{C2} \tag{5}$$

The general form of state equations for ON state and OFF state are given as,

$$\begin{array}{ll} \dot{X}(t) = A_1 x(t) + B_1 u(t) & \text{During dT} \\ \dot{X}(t) = A_2 x(t) + B_2 u(t) & \text{During d'T} \\ Y(t) = C_1 x(t) & \text{During dT} \\ Y(t) = C_2 x(t) & \text{During d'T} \end{array}$$

Where $X(t)$ is the state vector, $x(t)$ is the state variable matrix, $u(t)$ is the input variable matrix, A_1 and A_2 are the state matrices and B_1 and B_2 are the input matrices, C_1 and C_2 are the output matrices and d is the switching function. Thus, Equations (2) and (3) are represented in matrix form as,

$$\begin{bmatrix} \dot{I_{L1}} \\ \dot{I_{L2}} \\ \dot{V_{C1}} \\ \dot{V_{C2}} \end{bmatrix} = \begin{bmatrix} 0 & 0 & -1/L_1 & 0 \\ 0 & 0 & 0 & -1/L_2 \\ -1/C_1 & 0 & 0 & 0 \\ 0 & 1/C_2 & 0 & -1/RC_2 \end{bmatrix} \begin{bmatrix} I_{L1} \\ I_{L2} \\ V_{C1} \\ V_{C2} \end{bmatrix} + \begin{bmatrix} 1/L_1 \\ 1/L_2 \\ 0 \\ 0 \end{bmatrix} V_1 \tag{6}$$

$$\text{and} \qquad V_2 = \begin{bmatrix} 0 & 0 & 0 & 1 \end{bmatrix} \begin{bmatrix} I_{L1} \\ I_{L2} \\ V_{C1} \\ V_{C2} \end{bmatrix} \tag{7}$$

Equations (4) and (5) are represented in matrix form as,

$$\begin{bmatrix} \dot{I_{L1}} \\ \dot{I_{L2}} \\ \dot{V_{C1}} \\ \dot{V_{C2}} \end{bmatrix} = \begin{bmatrix} 0 & 0 & -1/L_1 & 0 \\ 0 & 0 & 1/L_2 & -1/L_2 \\ 1/C_1 & -1/C_1 & 0 & 0 \\ 0 & 1/C_2 & 0 & -1/RC_2 \end{bmatrix} \begin{bmatrix} I_{L1} \\ I_{L2} \\ V_{C1} \\ V_{C2} \end{bmatrix} + \begin{bmatrix} 0 \\ 0 \\ 0 \\ 0 \end{bmatrix} V_1 \tag{8}$$

$$\text{and} \qquad V_2 = \begin{bmatrix} 0 & 0 & 0 & 1 \end{bmatrix} \begin{bmatrix} I_{L1} \\ I_{L2} \\ V_{C1} \\ V_{C2} \end{bmatrix}. \tag{9}$$

The matrices of Equations (6) to (9) are averaged with respect to switching function D and $D^{'}$ and are given in Equations (10) and (11).

$$A = A_1 D + A_2 D^{'} = \begin{bmatrix} 0 & 0 & -1/L_1 & 0 \\ 0 & 0 & D^{'}/L_2 & -1/L_2 \\ 1/C_1 & -D^{'}/C_1 & 0 & 0 \\ 0 & 1/C_2 & 0 & -1/RC_2 \end{bmatrix} \& B = B_1 D + B_2 D^{'} = \begin{bmatrix} D/L_1 \\ D/L_2 \\ 0 \\ 0 \end{bmatrix} \tag{10}$$

$$C = C_1 D + C_2 D^{'} = \begin{bmatrix} 0 & 0 & 0 & 1 \end{bmatrix} \tag{11}$$

Thus, a complete averaged state space model of the CBC is given by the Equations (12) and (13).

$$\begin{bmatrix} \dot{I_{L1}} \\ \dot{I_{L2}} \\ \dot{V_{C1}} \\ \dot{V_{C2}} \end{bmatrix} = \begin{bmatrix} 0 & 0 & -1/L_1 & 0 \\ 0 & 0 & D^{'}/L_2 & -1/L_2 \\ 1/C_1 & -D^{'}/C_1 & 0 & 0 \\ 0 & 1/C_2 & 0 & -1/RC_2 \end{bmatrix} \begin{bmatrix} I_{L1} \\ I_{L2} \\ V_{C1} \\ V_{C2} \end{bmatrix} + \begin{bmatrix} D/L_1 \\ D/L_2 \\ 0 \\ 0 \end{bmatrix} V_1 \tag{12}$$

$$V_2 = \begin{bmatrix} 0 & 0 & 0 & 1 \end{bmatrix} \begin{bmatrix} I_{L1} \\ I_{L2} \\ V_{C1} \\ V_{C2} \end{bmatrix} \tag{13}$$

To obtain the linear small-signal state-space model, perturbation is added in each state variables and linear steady state model is obtained as in Equation (14).

$$\begin{bmatrix} \dot{\hat{I}}_{L1} \\ \dot{\hat{I}}_{L2} \\ \dot{\hat{V}}_{C1} \\ \dot{\hat{V}}_{C2} \end{bmatrix} = \begin{bmatrix} 0 & 0 & -1/L_1 & 0 \\ 0 & 0 & D^{'}/L_2 & -1/L_2 \\ 1/C_1 & -D^{'}/C_1 & 0 & 0 \\ 0 & 1/C_2 & 0 & -1/RC_2 \end{bmatrix} \begin{bmatrix} \hat{I}_{L1} \\ \hat{I}_{L2} \\ \hat{V}_{C1} \\ \hat{V}_{C2} \end{bmatrix} + \begin{bmatrix} -V_1/D^{'}L_1 \\ V_1/D^{'}L_2 \\ -DV_1/2RC_1 \\ 0 \end{bmatrix} \tag{14}$$

The general equation of Laplace transform of the linear steady state model is given by the following expression,

$$\hat{x}(s) = [sI - A]^{-1}[(A_1 - A_2)X + (B_1 - B_2)U]\hat{d}(s) = [[sI - A]^{-1}B_d]\hat{d}(s). \tag{15}$$

For CBC,

$$(sI - A) = s \begin{bmatrix} 1 & 0 & 0 & 0 \\ 0 & 1 & 0 & 0 \\ 0 & 0 & 1 & 0 \\ 0 & 0 & 0 & 1 \end{bmatrix} - \begin{bmatrix} 0 & 0 & -1/L_1 & 0 \\ 0 & 0 & D^{'}/L_2 & -1/L_2 \\ 1/C_1 & -D^{'}/C_1 & 0 & 0 \\ 0 & 1/C_2 & 0 & -1/RC_2 \end{bmatrix}$$

$$(sI - A) = \begin{bmatrix} s & 0 & 1/L_1 & 0 \\ 0 & s & -D^{'}/L_2 & 1/L_2 \\ -1/C_1 & D^{'}/C_1 & s & 0 \\ 0 & -1/C_2 & 0 & s + 1/RC_2 \end{bmatrix}. \tag{16}$$

$$\text{Now,} \qquad [sI - A]^{-1} = \frac{\text{Co-factor of } ((sI - A))^T}{\text{Determinant of } (sI - A)}. \tag{17}$$

$$\text{Let, Co-factors of } (sI - A) = \begin{bmatrix} C_{11} & C_{12} & C_{13} & C_{14} \\ C_{21} & C_{22} & C_{23} & C_{24} \\ C_{31} & C_{32} & C_{33} & C_{34} \\ C_{41} & C_{42} & C_{43} & C_{44} \end{bmatrix} \text{ then,}$$

$$(\text{Co-factors of } (sI - A))^T = \begin{bmatrix} C_{11} & C_{21} & C_{31} & C_{41} \\ C_{12} & C_{22} & C_{32} & C_{42} \\ C_{13} & C_{23} & C_{33} & C_{43} \\ C_{14} & C_{24} & C_{34} & C_{44} \end{bmatrix}. \tag{18}$$

Where, co-factors are given in Table 1.

Co-factor	Expression	Co- factor	Expression
C_{11}	$S^3+S^2\left(\frac{1}{RC_2}\right)+S\left(\frac{1}{L_2C_2}+\frac{D^{'2}}{L_1C_1}\right)+\frac{D^{'2}}{RC_1C_2L_2}$	C_{31}	$-S^2\frac{1}{L_1}-S\frac{1}{RC_2L_1}+\frac{1}{C_2L_1L_2}$
C_{12}	$\frac{D^{'}}{L_2}-\frac{1}{RC_1C_2}-S\frac{1}{C_1}$	C_{32}	$-S^2\frac{D^{'}}{L_2}-S\frac{D^{'}}{RC_2C_2}$
C_{13}	$S^2\frac{1}{C_1}-S\frac{1}{RC_1C_2}+\frac{1}{C_1C_2L_2}$	C_{33}	$S^3+S^2\left(\frac{1}{RC_2}\right)+S\frac{1}{L_2C_2}$
C_{14}	$-\frac{D^{'}}{C_1C_2L_2}$	C_{34}	$-S\frac{D^{'}}{C_2L_2}$
C_{21}	$-S\frac{D^{'}}{C_1L_1}-\frac{D^{'}}{RC_1C_2L_1}$	C_{41}	$\frac{D^{'}}{C_1L_1L_2}$
C_{22}	$S^3+S^2\left(\frac{1}{RC_2}\right)+S\frac{1}{L_1C_1}+\frac{1}{RC_1C_2L_1}$	C_{42}	$-S^2\frac{1}{L_2}-\frac{1}{C_1L_1L_2}$
C_{23}	$S^2\frac{D^{'}}{C_1}+S\frac{D^{'}}{RC_1C_2}$	C_{43}	$-S\frac{D^{'}}{C_1L_2}$
C_{24}	$S^2\frac{1}{C_2}+\frac{1}{C_1C_2L_1}$	C_{44}	$S^3+S\frac{D^{'2}}{L_2C_1}+S\frac{1}{C_1L_1}$

TABLE 1. (Co-factors of $(sI-A))^T$.

Determinant of $(sI-A)$ is

$$s\begin{bmatrix} s & -D^{'}/L_2 & 1/L_2 \\ D^{'}/C_1 & s & 0 \\ -1/C_2 & 0 & s+1/RC_2 \end{bmatrix}+0\begin{bmatrix} 0 & D^{'}/L_2 & 1/L_2 \\ -1/C_1 & s & 0 \\ 0 & 0 & s+1/RC_2 \end{bmatrix}$$

$$+1/L_1\begin{bmatrix} 0 & s & 1/L_2 \\ -1/C_1 & D^{'}/C_1 & 0 \\ 0 & -1/C_2 & s+1/RC_2 \end{bmatrix}+0\begin{bmatrix} 0 & s & D^{'}/L_2 \\ -1/C_1 & D^{'}/C_1 & s \\ 0 & -1/C_2 & 0 \end{bmatrix}.$$

This yields the determinant of $(sI-A)$ as,

$$1+s\left(\frac{L_2+D^{'2}L_1}{R}\right)+s^2[L_2C_2+L_1C_1+L_1C_2D^{'2}]+s^3\left(\frac{L_1L_2C_1}{R}\right)+s^4(L_1L_2C_1C_2) \tag{19}$$

Substituting Equations (18) and (19) in (15),

$$[sI-A]^{-1}=\frac{\begin{bmatrix} C_{11} & C_{21} & C_{31} & C_{41} \\ C_{12} & C_{22} & C_{32} & C_{42} \\ C_{13} & C_{23} & C_{33} & C_{43} \\ C_{14} & C_{24} & C_{34} & C_{44} \end{bmatrix}}{1+s\left(\frac{L_2+D^{'2}L_1}{R}\right)+s^2[L_2C_2+L_1C_1+L_1C_2D^{'2}]+s^3\left(\frac{L_1L_2C_1}{R}\right)+s^4(L_1L_2C_1C_2)} \tag{20}$$

and $$B_d=\begin{bmatrix} -V_1/D^{'}L_1 \\ V_1/D^{'}L_2 \\ -DV_1/2RC_1 \\ 0 \end{bmatrix}.$$

Thus, from Equation (14), the equation of Laplace transform of complex CBC becomes,

$$\hat{x}(s) = \left\{ \left[\frac{\begin{bmatrix} C_{11} & C_{21} & C_{31} & C_{41} \\ C_{12} & C_{22} & C_{32} & C_{42} \\ C_{13} & C_{23} & C_{33} & C_{43} \\ C_{14} & C_{24} & C_{34} & C_{44} \end{bmatrix}}{1 + s\left(\frac{L_2 + D'^2 L_1}{R}\right) + s^2[L_2C_2 + L_1C_1 + L_1C_2D'^2] + s^3\left(\frac{L_1L_2C_1}{R}\right) + s^4(L_1L_2C_1C_2)} \right] \begin{bmatrix} -V_1/D' L_1 \\ V_1/D' L_2 \\ -DV_1/2RC_1 \\ 0 \end{bmatrix} \right\} \hat{d}(s). \tag{21}$$

The general equation of Laplace transform of the output at a steady state is given by,

$$\hat{y} = C\hat{x}(s) + [(C_1 - C_2)X(s)]\hat{d}(s).$$

From Equation (7) and (9), $C_1 = C_2$. Thus, $\hat{y} = C\hat{x}(s)\hat{d}(s)$.

Hence for complex CBC,

$$\hat{V}_2(S) = \begin{bmatrix} 0 & 0 & 0 & 1 \end{bmatrix} \left\{ \left[\frac{\begin{bmatrix} C_{11} & C_{21} & C_{31} & C_{41} \\ C_{12} & C_{22} & C_{32} & C_{42} \\ C_{13} & C_{23} & C_{33} & C_{43} \\ C_{14} & C_{24} & C_{34} & C_{44} \end{bmatrix}}{1 + s\left(\frac{L_2 + D'^2 L_1}{R}\right) + s^2[L_2C_2 + L_1C_1 + L_1C_2D'^2] + s^3\left(\frac{L_1L_2C_1}{R}\right) + s^4(L_1L_2C_1C_2)} \right] \begin{bmatrix} -V_1/D' L_1 \\ V_1/D' L_2 \\ -DV_1/2RC_1 \\ 0 \end{bmatrix} \right\} \hat{d}(s). \tag{22}$$

Solving Equation (23), control to output transfer function of complex CBC is,

$$\frac{\widehat{V}_2(s)}{\hat{d}(s)} = \frac{\left(1 + sL_1\left(\frac{DD'}{2R}\right) + s^2 L_1C_1\left(\frac{1+D}{2D}\right)\right)}{1 + s\left(\frac{L_2 + D'^2 L_1}{R}\right) + s^2[L_2C_2 + L_1C_1 + L_1C_2D'^2] + s^3\left(\frac{L_1L_2C_1}{R}\right) + s^4(L_1L_2C_1C_2)}. \tag{23}$$

It is realised that the calculation of matrix $(sI - A)^{-1}$ becomes complicated for any high order circuits, which is in agreement with what is stated in [27].

2.3. PWM switch with EET technique

The main principle of the PWM switch modelling technique is the elimination of active and passive switches by their time-averaged models and obtain the averaged circuit model for a switched network, which is further inserted into the converter circuit. The final model is a time-averaged equivalent circuit model, where all branch currents and node voltages correspond to averaged values of corresponding original currents and voltages. Replacement of active and passive switches from the basic switch model (Figure 4) by switching functions d and d', respectively, is depicted in Figure 5.

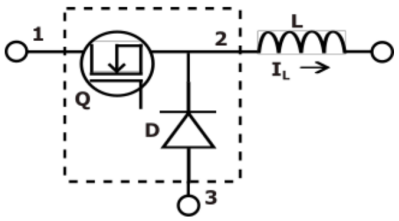

FIGURE 4. Basic circuit model of switch.

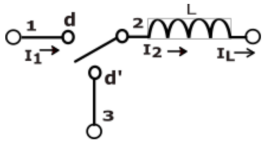

FIGURE 5. Replacement of switches.

The invariant average equations for Figure 5 are,

$$\left.\begin{aligned} I_1 &= dI_2 \\ V_{23} &= dV_{13} \end{aligned}\right\} \tag{24}$$

Adding a small deviation in duty ratio function d and then differentiating Equation (24),

$$\left.\begin{array}{c} \hat{\imath}_1 = D\hat{\imath}_2 + I_2\hat{d} \\ \widehat{V}_{23} = D\widehat{V}_{13} + V_{13}\hat{d} \end{array}\right\}, \tag{25}$$

where, D, I_2 and V_{13} are the steady state operating points of PWM switch. The PWM switch model from invariant average Equations (24) is obtained as depicted in Figure 6. Also, using Equation (25), dependent sources $D\hat{\imath}_2$ and $D\widehat{V}_{23}$ are replaced with 1:D transformer and moving control source $\hat{d}V_{13}$ from common terminal side to active terminal side, and the PWM switch model is obtained as in Figure 7. Thus, in PWM switch modelling with EET, the switch and diode are replaced point by point with its equivalent circuit model and further EET is employed to find out TF of the converter circuit.

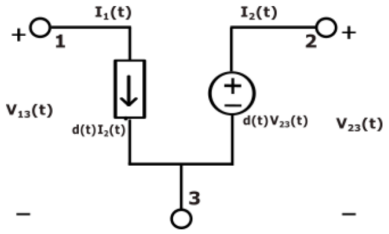

FIGURE 6. PWM switch model.

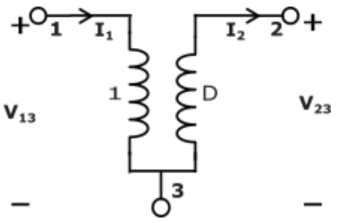

FIGURE 7. PWM switch model as 1:D transformer ratio.

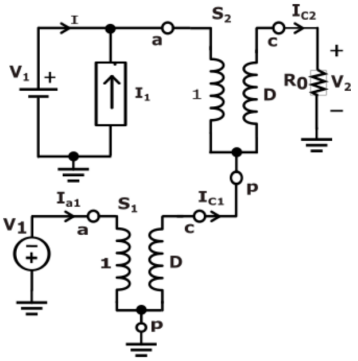

FIGURE 8. Two PWM switches as 1:D transformer ratio for CB.

Therefore, for complex CBC, the conditions of ON state and OFF state of switches are employed and two PWM switches are identified, which are represented as S_1 and S_2. The identified PWM switch models are replaced with 1:D transformer along with their small signals as depicted in Figure 8. In order to determine dc operating point of complex CBC, all inductors are short circuited and capacitors are open circuited. Referring to Figure 8, dc operating point with respect to switch S_1 is,

$$V_{ap1} = V_1.$$

Current flowing through terminal 'c' of switch S_1 is,

$$I_{c1} = I_{c2} - DI_{c2} = D^{'}I_{c2}.$$

Similarly, dc operating point with respect to switch S_2 is,

$$V_{ap} = V_1(1+D),$$
$$I_{c2} = \frac{V_2}{R} = \frac{D^2V_1}{R}.$$

Once the dc operating point is determined, 4-EET is applied that provides separate, independent steps of the analytical technique. The general form of control to output transfer function is $\left[\frac{\widehat{v_2}(s)}{\hat{d}(s)}\right]$. In the very first step of 4-EET, denominator $\hat{d}(s)$ is determined, for which each impedance element of the converter is treated as extra element and input sources are set to zero. With respect to Figure 3 C_1, C_2, L_2 and L_1 are considered as 4 ports and numbered as port (1), (2), (3) and (4), respectively. Treating these ports as an extra element,

various time constants are determined by removing port elements and observing the remaining circuit through the removed port.

The denominator of the transfer function is given by the following equation:

$$\hat{d}(s) = 1 + a_1 s + a_2 s^2 + a_3 s^3 + a_4 s^4, \tag{26}$$

where

$$\left.\begin{array}{c} a_1 = \tau_1 + \tau_2 + \tau_3 + \tau_4 \\ a_2 = \tau_1\tau_1^2 + \tau_1\tau_1^3 + \tau_1\tau_1^4 + \tau_2\tau_2^3 + \tau_2\tau_2^4 + \tau_3\tau_3^4 \\ a_3 = \tau_1\tau_1^3\tau_{31}^2 + \tau_4\tau_4^1\tau_{41}^2 + \tau_4\tau_4^1\tau_{41}^3 + \tau_3\tau_2^3\tau_{23}^4 \\ a_4 = \tau_4\tau_4^1\tau_{41}^3\tau_{413}^2 \end{array}\right\} \tag{27}$$

Figure 9 is referred for determination of (τ) for a_1, which is explained in Table 2.

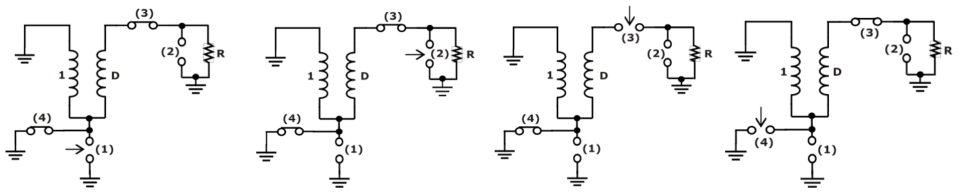

FIGURE 9. Determination of (a) τ_1 (b) τ_2 (c) τ_3 (d) τ_4.

τ	**Expression**
τ_1	Time constant of first port is R_{eq} x C_1, determined by observing the circuit through port (1), capacitor of this port 1 is assumed as extra element and is removed temporarily, L_1, L_2 and C_2 are assumed in dc condition. By observing through port 1, the R_{eq} is 0, therefore, $\tau_1 = R_{eq}$ x $C_1 = 0$.
τ_2	Time constant of second port is R_{eq} x C_2, determined by observing the circuit through port (2), capacitor of this port is now extra element and is removed temporarily, L_1, L_2 and C_1 are assumed in dc condition. After observation, R_{eq} is 0, therefore, $\tau_2 = R_{eq}$ x $C_2 = 0$.
τ_3	Time constant of third port is $\left(\frac{L_2}{R_{eq}}\right)$, which is determined by observing the circuit through port (3). Inductor of this port is extra element and is removed temporarily and C_1, C_2 and L_1 are kept in dc condition. By observation, R_{eq} is R. Hence, $\tau_3 = \frac{L_2}{R}$.
τ_4	Time constant of fourth port is $\left(\frac{L_1}{R_{eq}}\right)$, which is determined by observing the circuit through port (4). Inductor of this port is extra element and is removed temporarily and C_1, C_2 and L_2 are kept in dc condition. By observing the circuit it is seen that R_{eq} is $\frac{R}{D'^2}$. Hence, $\tau_4 = \frac{L_1 D'^2}{R}$.

TABLE 2. Determination of (τ) for a_1.

By summarizing the results of Table 2, we get:

$$a_1 = \frac{L_2}{R} + \frac{L_1 D'^2}{R} \tag{28}$$

First two terms and the last term of the a_2 (Equation (27)) are zero. The calculation of a_2 is only addition of middle terms, i.e. $(\tau_1\tau_1^4 + \tau_2\tau_2^3 + \tau_2\tau_2^4)$, which are indeterminate and is removed by changing the port sequence as $[\tau_4\tau_4^1 + \tau_3\tau_3^2 + \tau_4\tau_4^2]$. Referring the Figure 10, terms τ_4^1 , τ_3^2 and τ_4^2 are determined as described in Table 3.

By summing up the results from the Table 3, we get:

$$a_2 = L_1C_1 + L_2C_2 + L_1C_2D'^2. \tag{29}$$

The first term of the a_3 (Equation (27)) cannot be determined as it gives a ratio of (0/0), this indeterminacy in time constants is removed with new sequence of ports for a_3 which is,

$$a_3 = \tau_1\tau_1^3\tau_{31}^2 + \tau_4\tau_4^1\tau_{41}^2 + \tau_4\tau_4^1\tau_{41}^3 + \tau_3\tau_2^3\tau_{23}^4. \tag{30}$$

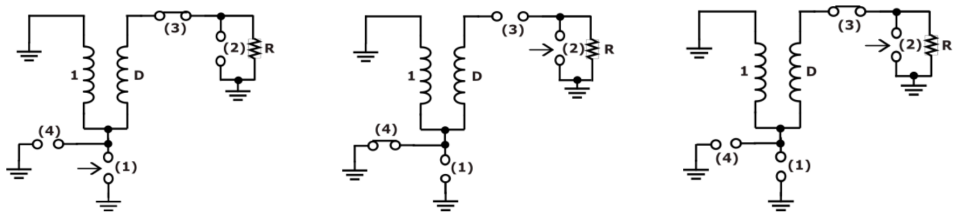

FIGURE 10. Determination of (a) τ_4^1 (b) τ_3^2 (c) τ_4^2.

τ	Expression
τ_4^1	Observing the circuit through port (1), port (4) is considered in high frequency state and ports (2) and (3) are kept in dc condition, capacitor of port (1) is treated as extra element and removed temporarily, equivalent resistance R_{eq} is $\frac{R}{D'^2}$. Hence $\tau_4\tau_4^1 = L_1C_1$.
τ_3^2	Observing the circuit through port (2), port (3) is considered in high frequency state and ports (1) and (4) are kept in dc condition, capacitor of port (2) is treated as extra element and removed temporarily, equivalent resistance R_{eq} is R. Therefore $\tau_3\tau_3^2$ is L_2C_2.
τ_4^2	Observing the circuit through port (2), port (4) is considered in high frequency state and ports (1) and (3) are kept in dc condition, capacitor of port (2) is treated as extra element and removed temporarily, equivalent resistance R_{eq} is R. Therefore $\tau_4\tau_4^2$ is $L_1C_2D'^2$.

TABLE 3. Determination of (τ) for a_2.

The first two terms and last term of the Equation (30) are zero. To calculate τ_{41}^3 , the circuit in Figure 11 is observed through port (3), while ports (1) and (4) are kept in a high frequency condition. Here R_{eq} is R which results in $\tau_{41}^3 = \frac{L_3}{R_{eq}} = \frac{L_3}{R}$. Hence,

$$a_3 = \tau_4\tau_4^1\tau_{41}^3 = \frac{L_1L_2C_1}{R}. \tag{31}$$

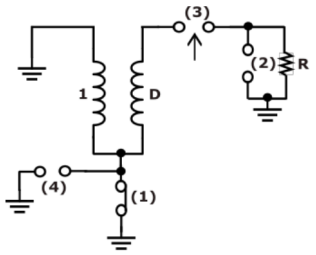

FIGURE 11. Determination of τ_{41}^3.

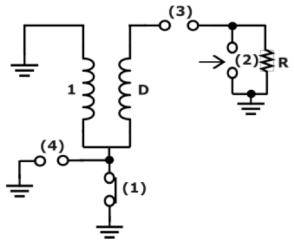

FIGURE 12. Determination of τ_{413}^2.

For the determination of a_4, referring to Figure 12, τ_{413}^2 is determined by observing the circuit through port (2), while ports (4), (1) and (3) are kept in high frequency condition. In such situation, R_{eq} is R and τ_{413}^2 is RC_2. The calculation of the term $(\tau_4\tau_4^1\tau_{41}^3\tau_{413}^2)$ results in $(L_1L_2C_1C_2)$. Hence,

$$a_4 = L_1L_2C_1C_2. \tag{32}$$

Using Equations (28), (29), (31) and (32) in Equation (26), the denominator of control to output transfer function of complex CBC becomes,

$$\hat{d}(s) = 1 + \left(\frac{L_2}{R} + \frac{L_1D'^2}{R}\right)s + (L_1C_1 + L_2C_2 + L_1C_2D'^2)s^2 + \left(\frac{L_1L_2C_1}{R}\right)s^3 + L_1L_2C_1C_2s^4. \tag{33}$$

Now, the excitation applied to the port is retained as it is and additional excitation is applied to the port of the extra element with the extra element removed. With these two excitations, the response is considered as null. Simultaneously, the conversion ratio D^2 is differentiated with respect to D. Considering this differentiation and null response condition altogether, the numerator of transfer function is determined.

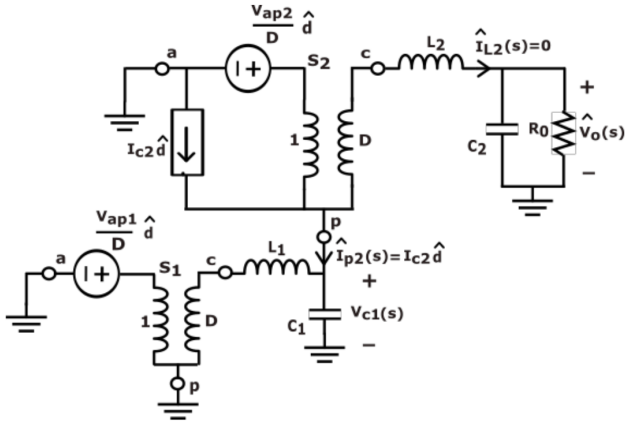

FIGURE 13. Null condition at the output of complex CBC for determination of numerator.

By considering a null response at the output of complex CBC (Figure 13), it is observed that the presence of $\hat{\imath}_{L2}(s)$ creates the condition as represented by the equation, $\hat{\imath}_{p2}(s) = \hat{\imath}_{c2}\hat{d}(s)$ and the resultant voltage across C_1 is,

$$\widehat{V}_{c1}(s) = V_{ap}\hat{d}\frac{(1/(sC_1)}{(SL_1 + 1/sC_1)} + I_{c2}\hat{d}\left[sL_1||(1/sC_1)\right]. \tag{34}$$

This voltage must be the same as that of D side of the second PWM switch. Hence,

$$\widehat{V}_{c1}(s) = -\left[\frac{V_{ap2}}{D}\hat{d} - \widehat{V}_{c1}(s)\right]D. \tag{35}$$

From Equations (34) and (35),

$$D^{'}V_{ap1}\frac{1}{1 + s^2L_1C_1} + D^{'}I_{C2}\frac{sL_1}{1 + s^2L_1C_1} + V_{ap2} = 0. \tag{36}$$

Which yields the numerator of the control to output transfer function of complex CBC as given by,

$$\widehat{V}_2(s) = 1 + sL_1\frac{DD^{'}}{2R} + s^2L_1C_1\frac{1+D}{2D}. \tag{37}$$

Using Equations (33) and (37), the overall transfer function of complex CBC is given by the Equation (38):

$$\frac{\widehat{V}_2(s)}{\hat{d}(s)} = \frac{\left(1 + sL_1\left(\frac{DD^{'}}{2R}\right) + s^2L_1C_1\left(\frac{1+D}{2D}\right)\right)}{1 + s\left(\frac{L_2+D'^2L_1}{R}\right) + s^2[L_2C_2 + L_1C_1 + L_1C_2D'^2] + s^3\left(\frac{L_1L_2C_1}{R}\right) + s^4(L_1L_2C_1C_2)}. \tag{38}$$

3. SIMULATION OF COMPLEX CBC

The simulation circuit is developed; voltage and current graphs (Figure 14), time response (Figure 15) and frequency response plot (Figure 16) are obtained for complex CBC using MATLAB simulation to study the behaviour of CBC. The circuit parameters for the simulation are selected as: Inductors $L_1 = 524\,\mu H$, $L_2 = 1200\,\mu H$, capacitors $C_1 = C_2 = 5\,\mu F$, output resistance $R_0 = 8.05\,\text{ohm}$, switch (Q_1) parameters: FET ON resistance $= 0.1\,\Omega$, internal diode resistance $= 0.01\,\Omega$, internal diode forward voltage $= 0.7\,V$, diode (D_1, D_2, D_3) parameters: resistance $= 0.01\,\Omega$, forward voltage $= 0.8\,V$, switching frequency $= 50\,KHz$.

For a duty ratio of 0.35, input voltage $V_1 = 25\,V$, and source current $= 0.05746\,A$, output voltage $V_2 = 3\,V$ and load current $= 0.367\,A$ was observed (Figure 14). Also output voltage and load currents for different duty ratios of complex CBC are depicted in Table 4. From the transient and steady state response, it is observed that the output voltage has settled to about 3 volts with the settling time of approximately 0.9 ms after the application of input voltage. The system is stable (Figure 16), as gain margin is positive (∞ db) and phase margin is also positive (450°).

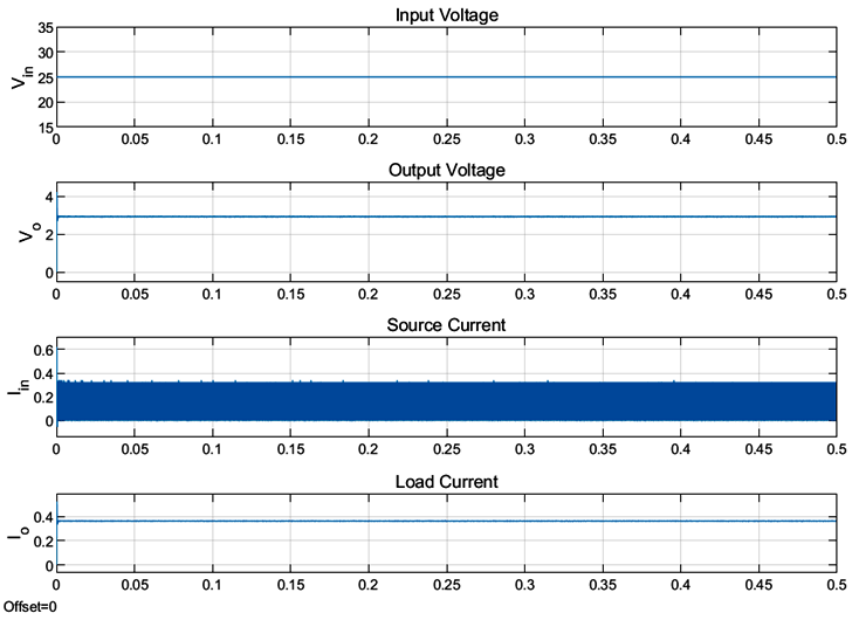

FIGURE 14. Voltage and current graphs of complex CBC.

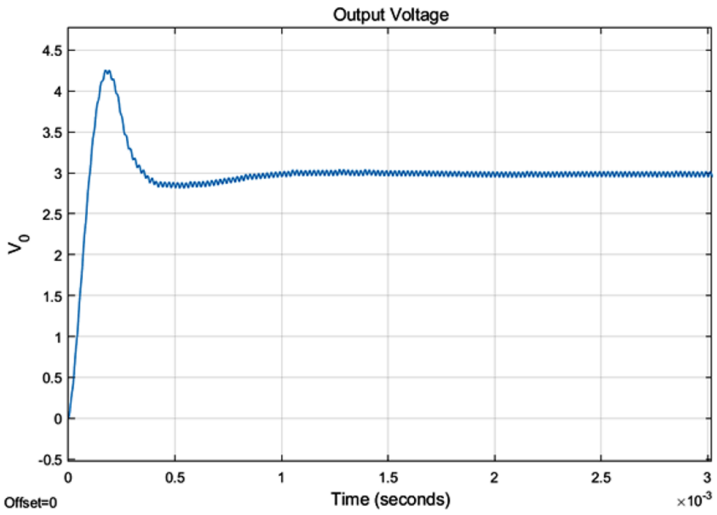

FIGURE 15. Transient and steady state response of complex CBC.

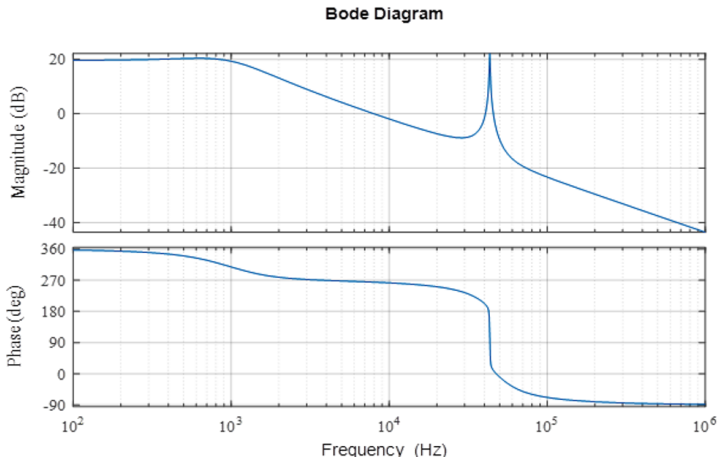

FIGURE 16. Bode plot of control to output transfer function of complex CBC.

Duty ratio	Output voltage [V]	Load current [A]
0.3	2.47	0.3076
0.4	3.434	0.4266
0.5	5.44	0.6762
0.6	8.601	1.068
0.7	11.78	1.464

Table 4. Load current and output voltage for different duty rates.

4. Results and discussion

SSA and PWM switch modelling with EET technique for CBC (Section 2.2 and 2.3) are brainstormed, compared for different features and the results are summarized in Table 5. In SSA, a linearisation of all the components of the converter is performed, whereas in the PWM switch model method, only non-linear switching devices are linearised and linear components remain unchanged. In SSA technique, a set of differential equations are written which are further averaged with respect to the duty ratio function. The averaged equations are then linearised by using principle of perturbation, Laplace transform is applied to the linear state space model of CBC and the control to output transfer function is obtained. Unlike SSA technique, differential equations are not required in PWM switch modelling technique. Averaging and linearisation with the help of perturbation is accomplished using the PWM switch itself. Instead of Laplace transform, EET is applied to the linearised model of CBC to derive the control to output transfer function.

The SSA model of CBC is a systematic procedure involving mathematics without any circuit transformation. It involves complex mathematical transformations and a higher number of mathematical equations. In contrast, PWM switch modelling technique with EET consists of simple mathematical transformations. However, expertise is required for proper circuit transformations. Based on the parametric comparison (Table 5) of two analytical techniques, it is observed that SSA is better than the PWM with EET for a high-order circuit, due to systematic, straightforward procedural steps. PWM with EET for a high-order circuit requires a higher number of circuit transformations and a high expertise, which makes it time consuming and difficult.

Features	SSA technique	PWM switch modelling with EET
Analysis approach	Mathematical	Mainly circuit oriented
Structure of analysis	Systematic	Less systematic
Equivalent diagram	Not required	Required
Circuit transformation	Not required	Required
Number of mathematical transformations	More	Less
Number of mathematical equations	More	Less
Complexity of mathematical transformations	High	Low
Expertise required	Mathematical	Identification of PWM switch, changing the port sequences in case of indeterminacy and application of EET
Identification of PWM switch	Not required	Required
Extra Element Theorem	Not applicable	Applicable
Form of transfer function	Low entropy	Low entropy
The complexity of the modelling process	Low	High
Steady state analysis	Yes	Yes
Transient state analysis	Yes	Yes

Table 5. Results of comparative evaluation of the modelling techniques.

5. Conclusion

This paper presents a comparative study of two modelling techniques commonly used for modelling of DC-DC converters, which is first in its kind. The transfer functions of a complex CBC converter were developed using

state space averaging and PWM switch modelling with an extra element theorem and the simulation results were obtained. The state space modelling approach is purely mathematical and systematic. However, it involves complex mathematics for high-order circuits. The PWM switch modelling approach is mainly circuit oriented approach, which involves relatively simple mathematical transformations. However, circuit transformations become complex for a high-order circuit. A number of complex circuit transformations and identification of the PWM switch, changing the port sequences in the case of indeterminacy and application of EET make the PWM switch modelling approach a complex one as compared to the state space averaging approach.

References

[1] S. H. Shete, P. M. Joshi. Analytical techniques for DC DC converters and 1Φ inverters: A comprehensive review. *Journal of The Institution of Engineers (India): Series B volume* **103**:1827–1844, 2022. https://doi.org/10.1007/s40031-022-00759-x.

[2] E. Vuthchhay, C. Bunlaksananusorn. Dynamic modeling of a zeta converter with state-space averaging technique. In *2008 5th International Conference on Electrical Engineering/Electronics, Computer, Telecommunications and Information Technology*, vol. 2, pp. 969–972. 2008. https://doi.org/10.1109/ECTICON.2008.4600593.

[3] S. Hegde, A. Izadian. A new SEPIC inverter: Small signal modeling. In *IECON 2013 – 39th Annual Conference of the IEEE Industrial Electronics Society*, pp. 240–245. 2013. https://doi.org/10.1109/IECON.2013.6699142.

[4] A. Davoudi, J. Jatskevich, T. De Rybel. Numerical state-space average-value modeling of PWM DC-DC converters operating in DCM and CCM. *IEEE Transactions on Power Electronics* **21**(4):1003–1012, 2006. https://doi.org/10.1109/TPEL.2006.876848.

[5] D. Czarkowski, M. K. Kazimierczuk. Energy-conservation approach to modeling PWM DC-DC converters. *IEEE Transactions on Aerospace and Electronic Systems* **29**(3):1059–1063, 1993. https://doi.org/10.1109/7.220955.

[6] M. Bartoli, A. Reatti, M. K. Kazimierczuk. Open loop small-signal control-to-output transfer function of PWM buck converter for CCM: modeling and measurements. In *Proceedings of 8th Mediterranean Electrotechnical Conference on Industrial Applications in Power Systems, Computer Science and Telecommunications (MELECON 96)*, vol. 3, pp. 1203–1206. 1996. https://doi.org/10.1109/MELCON.1996.551161.

[7] N. Kroutikova, C. A. Hernandez-Aramburo, T. C. Green. State-space model of grid-connected inverters under current control mode. *IET Electric Power Applications* **1**:329–338, 2007. https://doi.org/10.1049/iet-epa:20060276.

[8] H. Mashinchi Mahery, E. Babaei. Mathematical modeling of buck-boost dc-dc converter and investigation of converter elements on transient and steady state responses. *International Journal of Electrical Power & Energy Systems* **44**(1):949–963, 2013. https://doi.org/10.1016/j.ijepes.2012.08.035.

[9] S. Laali, H. M. Mahery. Buck DC-DC converter: Mathematical modeling and transient state analyzes. In *2012 3rd IEEE International Symposium on Power Electronics for Distributed Generation Systems (PEDG)*, pp. 661–667. 2012. https://doi.org/10.1109/PEDG.2012.6254073.

[10] M. Muntasir Nishat, M. A. Moin Oninda, F. Faisal, M. A. Hoque. Modeling, simulation and performance analysis of SEPIC converter using hysteresis current control and PI control method. In *2018 International Conference on Innovations in Science, Engineering and Technology (ICISET)*, pp. 7–12. 2018. https://doi.org/10.1109/ICISET.2018.8745619.

[11] V. Vorperian. Simplified analysis of PWM converters using model of PWM switch. Continuous conduction mode. *IEEE Transactions on Aerospace and Electronic Systems* **26**(3):490–496, 1990. https://doi.org/10.1109/7.106126.

[12] C. Basso. Switching-converter dynamic analysis with fast analytical techniques: Overview and applications. *IEEE Power Electronics Magazine* **4**(3):41–52, 2017. https://doi.org/10.1109/MPEL.2017.2718238.

[13] H. G. Tan Rodney, L. Y. H. Hoo. DC-DC converter modeling and simulation using state space approach. In *2015 IEEE Conference on Energy Conversion (CENCON)*, pp. 42–47. 2015. https://doi.org/10.1109/CENCON.2015.7409511.

[14] T. Polsky, Y. Horen, S. Bronshtein, D. Baimel. Transient and steady-state analysis of a SEPIC converter by an average state-space modelling. In *2018 IEEE 18th International Power Electronics and Motion Control Conference (PEMC)*, pp. 211–215. 2018. https://doi.org/10.1109/EPEPEMC.2018.8522000.

[15] B. P. Mokal, K. Vadirajacharya. Extensive modeling of DC-DC Cuk converter operating in continuous conduction mode. In *2017 International Conference on Circuit ,Power and Computing Technologies (ICCPCT)*, pp. 1–5. 2017. https://doi.org/10.1109/ICCPCT.2017.8074188.

[16] G. Kanimozhi, J. Meenakshi, V. T. Sreedevi. Small signal modeling of a DC-DC type double boost converter integrated with SEPIC converter using state space averaging approach. *Energy Procedia* **117**:835–846, 2017. https://doi.org/10.1016/j.egypro.2017.05.201.

[17] V. Eng, U. Pinsopon, C. Bunlaksananusorn. Modeling of a SEPIC converter operating in continuous conduction mode. In *2009 6th International Conference on Electrical Engineering/Electronics, Computer, Telecommunications and Information Technology*, pp. 136–139. 2009. https://doi.org/10.1109/ECTICON.2009.5136982.

[18] O. Kircioğlu, M. Ünlü, S. Çamur. Modeling and analysis of DC-DC SEPIC converter with coupled inductors. In *2016 International Symposium on Industrial Electronics (INDEL)*, pp. 1–5. 2016. https://doi.org/10.1109/INDEL.2016.7797807.

[19] N. Mohan, T. M. Undeland, W. P. Robbins. *Power Electronics – Converters, Applications and Design.* 3rd edition. John Wiley and Sons, 2013.

[20] C. Basso. *Linear Circuit Transfer Functions: An Introduction to Fast Analytical Techniques.* Wiley, Hoboken, NJ, 2016.

[21] V. Vorpérian. *Fast Analytical Techniques for Electrical and Electronic Circuits.* Cambridge University Press, Cambridge, U.K., 2002.

[22] S. K. Pidaparthy, B. Choi. Output impedance analysis of PWM DC-to-DC converters. In *2019 10th International Conference on Power Electronics and ECCE Asia (ICPE 2019 – ECCE Asia)*, pp. 849–855. 2019. https://doi.org/10.23919/ICPE2019-ECCEAsia42246.2019.8796492.

[23] B. Choi, D. Kim, D. Lee, et al. Analysis of input filter interactions in switching power converters. *IEEE Transactions on Power Electronics* **22**(2):452–460, 2007. https://doi.org/10.1109/TPEL.2006.889925.

[24] E. Can. PWM controlling of a new multi DC-DC converter circuit. *Technical Journal* **13**(2):116–122, 2019. https://doi.org/10.31803/tg-20190427093441.

[25] E. Can, H. H. Sayan. Different mathematical model for the chopper circuit. *Technical Journal* **10**(1-2):13–15, 2016. https://hrcak.srce.hr/file/238913.

[26] D. Maksimovic, S. Cuk. Switching converters with wide DC conversion range. *IEEE Transactions on Power Electronics* **6**(1):151–157, 1991. https://doi.org/10.1109/63.65013.

[27] M. M. Garg, Y. V. Hote, M. K. Pathak. Pi controller design of a dc-dc Zeta converter for specific phase margin and cross-over frequency. In *2015 10th Asian Control Conference (ASCC)*, pp. 1–6. 2015. https://doi.org/10.1109/ASCC.2015.7244716.

HEAT TRANSFER CHARACTERISTICS OF DOUBLE PIPE HEAT EXCHANGER HAVING EXTERNALLY ENHANCED INNER PIPE

Balasubramanian Vijayaragavan, Suyambu Pandian Asok, Chandrasekar Ramalekshmi Shakthi Ganesh*

Mepco Schlenk Engineering College, Department of Mechanical Engineering, Sivakasi, Virudhunagar District-626005, Tamilnadu, India

* corresponding author: shakthi.jan25@gmail.com

Abstract. An investigation on enhancement of heat transfer is carried out for a double pipe heat exchanger in which the outer wall of the inner pipe is provided with circumferential labyrinth passages. Rectangular and triangular cavities with fixed labyrinth tooth thickness, height, and pitch are considered and the effect of added labyrinth structures on the heat transfer characteristics is discussed. A two-dimensional steady numerical simulation is carried out using ANSYS-FLUENT software. The flow Reynolds number equals to 20 000 and 43 000 for the hot and cold fluids, respectively, while other fluid properties are constant. From the numerical analysis carried out in this work, it is identified that the added labyrinth passages in the heat exchange surface improve the heat transfer rate and can reduce the length of the heat exchanger. Numerical predictions agree well with the results obtained from the experiment conducted.

Keywords: Double pipe heat exchanger, heat transfer, numerical analysis, rectangular cavity.

1. Introduction

Heat exchange between hot and cold fluid plays a significant role in many applications. Heat transfer enhancement techniques implemented in heat exchangers reduce the running costs of the device by saving energy. Out of the various types of heat exchangers available, the double pipe heat exchanger shown in Figure 1 is a simple design with two concentric pipes, whose performance can be substantially improved by various enhancements. It is also suitable for high temperature and high pressure applications due to its small diameters. The literatures regarding these enhancements are primarily experimental in nature, with gases as working fluids [1, 2].

The heat transfer enhancement techniques in a double pipe heat exchanger are classified into passive and active techniques. Passive methods can work without any external aids by a geometric modification such as varying the cross section of the inner pipe [2–8]. Active methods require external stimulation such as vortex creation by rotating the inner pipe [9]. The helically corrugated inner pipe with alternating ridges and grooves in a double pipe heat exchanger was investigated using steady numerical simulations [2]. The new design improved the heat transfer by a factor of three as compared to the smooth-walled inner pipe.

The heat transfer characteristics of blossom shaped fins on the inner tube were investigated experimentally and numerically at a constant air inlet temperature [3]. The increase in the number of fins resulted in a more uniform distribution of the temperature field. The reasons for the performance improvement of the double pipe heat exchanger with helical fins and vortex generator were found to be the increase in heat transfer surface, reduction of hydraulic diameter, secondary flow caused by the helical channel and the vortices, destabilisation of fluid flow and intensification of turbulence induced by the vortex generators [4]. The inner twisted square duct with air as working fluid showed a considerable enhancement in the heat transfer in both the laminar and turbulent regimes [5]. Experimental investigations of a double pipe helical heat exchanger with a copper fin in the annulus section showed an improvement in the overall heat transfer coefficient calculated by replacing the hydraulic diameter with an equivalent diameter [6].

In the present study, an improvement in the performance of a double pipe heat exchanger is achieved by incorporating a labyrinth path in the annular region, which enhances the surface area of the inner tube externally. Thus, the labyrinth structure increases the surface area of heat transfer. During the flow through this enhanced structure, the fluid is made to pass through cavities and the corresponding land, resulting in vortex generation in each cavity. The recirculation caused by the vortex increases the heat transfer rate of the hot fluid by increasing the number of restrictions [10]. The labyrinth structure introduced in the outer surface of the inner pipe is shown in Figure 2.

In the conventional double pipe heat exchangers, the annular area is kept larger to allow the cold fluid flow to gain heat from the hot fluid flowing in the inner pipe. The innovation in the present study is the improvement in heat transfer by enhancing the annular flow path with the annular flow area much lesser than the pipe flow area and leaving the pipe flow undisturbed. Even a small amount of increase in

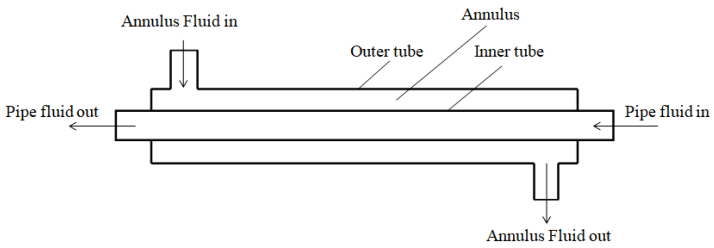

Figure 1. Schematic of the double pipe heat exchanger.

Figure 2. Heat exchanger with labyrinth.

the rate of the heat transfer by surface modification can result in a considerable improvement in process efficiency and economy. The dimensions of the heat exchanger before modification are given in Figure 3.

By incorporating the enhanced structure on the outer surface of the inner tube, the heat transfer by the fluid flowing in the annular region is improved [11–13]. The enhancement with a triangular geometry can provide a stable flow recirculation in the cavity [14]. Hence, the triangular cavity can be a good option for heat transfer studies in addition to the rectangular cavity, which is popularly used. The details of the rectangular and triangular cavity structures incorporated in the outer surface of the inner tube are shown in Figure 4 and Figure 5, respectively. The surface enhancers efficiently augment the heat transfer rate due to the induced turbulence intensity [15]. Heat transfer decreases with the increase in the thickness and pitch of the external surface enhancers to be introduced in the heat exchangers [11]. Hence, the thickness and pitch of the tooth surface to be machined are fixed as 4 mm and 8 mm, respectively. In the present work, water is selected as the working fluid and a two-dimensional numerical analysis is carried out. The investigation on the heat transfer characteristics of the double pipe heat exchanger is carried out both numerically and experimentally with Reynolds number values up to 43 000.

2. Numerical simulation

CFD software is largely used to study the fluid flow and heat transfer by solving the mathematical equations with the help of a numerical analysis. It is equally helpful in designing a heat exchanger system as well as in troubleshooting by suggesting design modifications [16]. The two-dimensional geometric model of the double pipe heat exchanger is developed in SOLIDWORKS designing tool and imported into the ANSYS FLUENT in IGS format. Due to the symmetric nature of the heat exchanger, only the top half of the heat exchanger is modelled, and an axisymmetric condition is applied in the ANSYS FLUENT solver. The existing problem is thus simulated by using a two-dimensional heat transfer analysis [17–19]. Triangle elements are applied for all the three regions. The axisymmetric heat exchanger models for plain profile, profile with rectangular, and triangular labyrinths, whose meshes are shown in Figure 6, 7 and 8, respectively, are developed. Region 1 represents the hot fluid domain; Region 2 represents the copper solid domain and Region 3 represents the cold fluid domain. The body sizing and refinement conditions differ for each region.

Zero heat flux boundary condition is applied to the outer wall and solid side walls, assuming to be perfectly insulated [10]. The solid fluid interfaces are no-slip walls where the heat flux and the temperature are continuous across the boundary line [1, 3]. A grid independent test was conducted to check the dependence of the solution on the quality of the mesh. Pressure-based solver and k-epsilon turbulence model are chosen for the study [17, 20]. The k-epsilon models are categorised in two equation models in which both the turbulent length and the time scale are determined by solving two separate transport equations. Out of the three different k-epsilon models in ANSYS FLUENT, the standard k-epsilon model is the most commonly used model for simulating a turbulent flow [21]. The inlet temperature and mass flow rate of the cold and hot fluids are specified. At the outlet, the mass flow outlet condition is specified for both the hot and cold fluids. Table 1 gives the details of the solution methods used. An important aspect in the numerical analysis is to arrive at a convergence of the solution. The convergence criterion for continuity, velocity, and k-epsilon equations are reduced to 0.001, and for the energy equation, the value is set to 0.0001.

The differential equations constituting the mathematical model for the physical problem under study is given below.

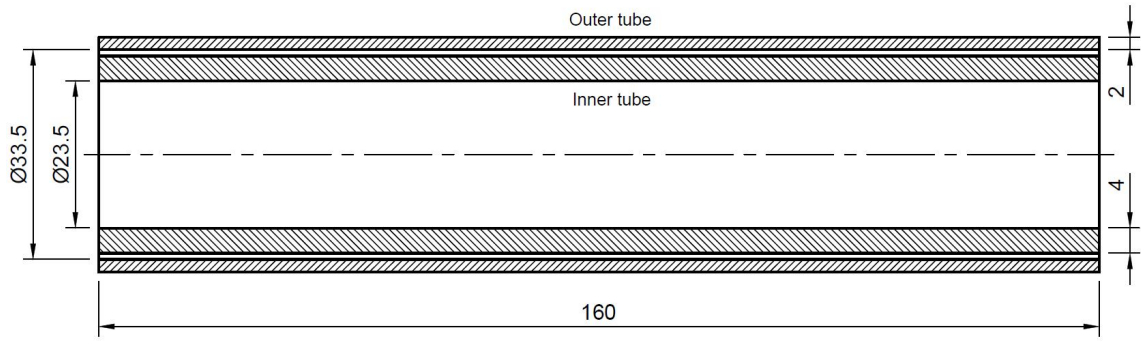

FIGURE 3. Dimensions of the plain heat exchanger.

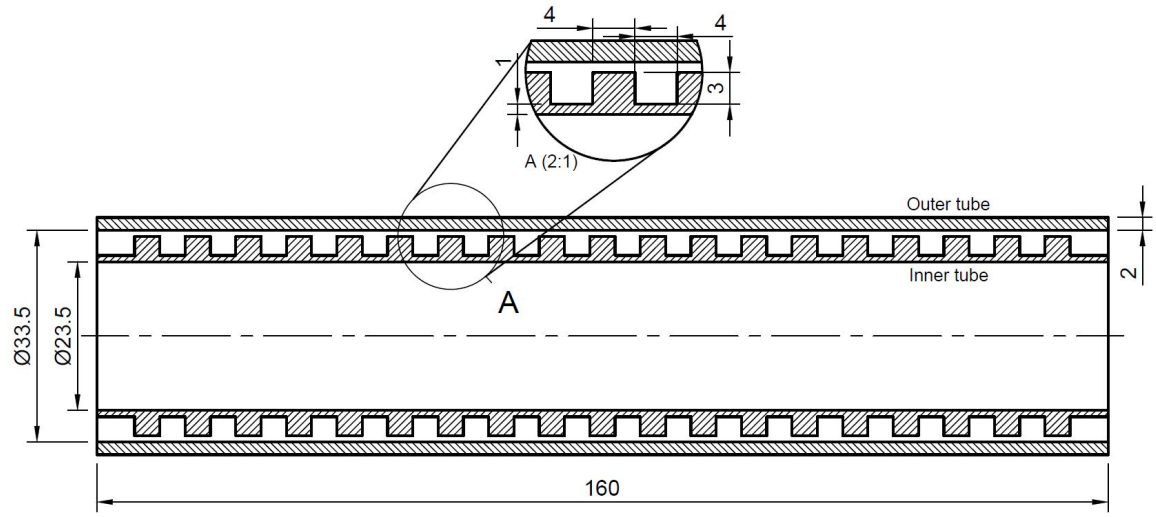

FIGURE 4. Dimensions of rectangular labyrinth heat exchanger.

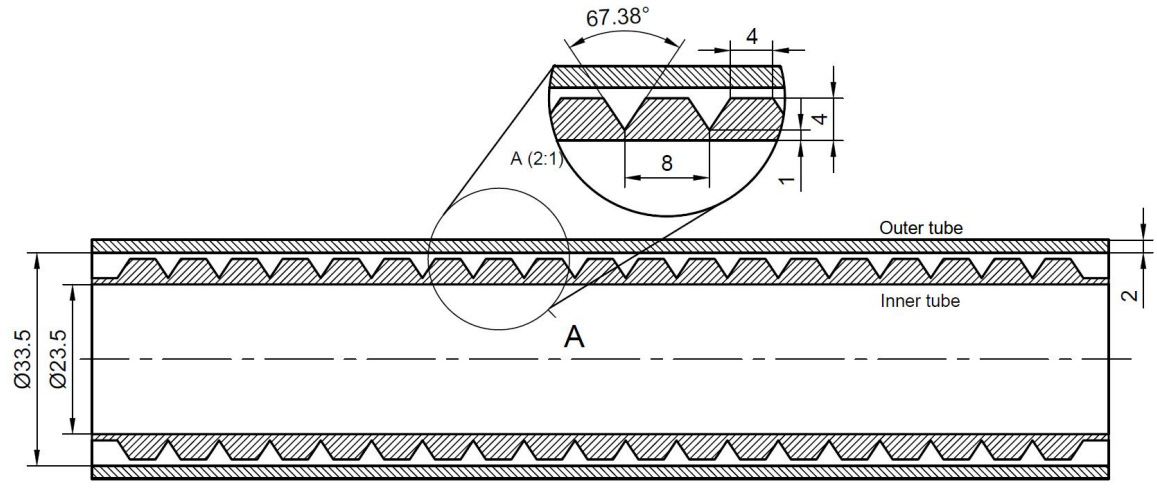

FIGURE 5. Dimensions of the triangular labyrinth heat exchanger.

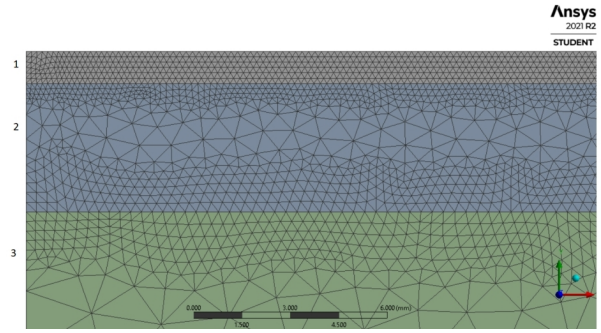

Figure 6. Mesh picture for plain heat exchanger model.

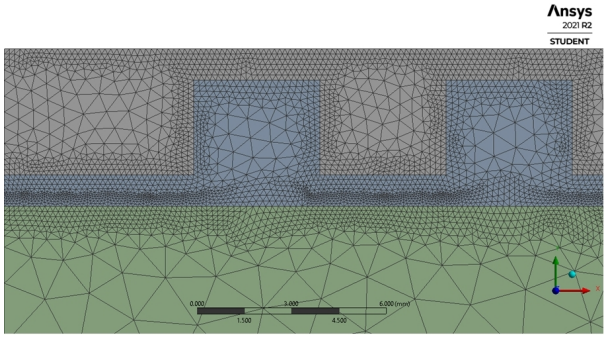

Figure 7. Mesh picture for heat exchanger with rectangular labyrinth.

Conservation of mass:

$$\frac{\partial \rho}{\partial t} + \frac{\partial (\rho u_j)}{\partial x_j} = 0. \tag{1}$$

Conservation of momentum:

$$\frac{\partial (\rho u_j)}{\partial t} + \frac{\partial (\rho u_j u_i)}{\partial x_j} = \rho f_i + \frac{\partial \sigma_{ji}}{\partial x_j}. \tag{2}$$

Conservation of energy:

$$\frac{\partial (\rho e)}{\partial t} + \frac{\partial (\rho e u_j)}{\partial x_j} = -\rho f_i u_i + \frac{\partial (\sigma_{ji} u_i)}{\partial x_j} - \frac{\partial q_j}{\partial x_j} \tag{3}$$

The established mathematical model is solved by a finite volume method where the computational domain is divided into small volumes, and then the discrete algebraic equations of the above model are solved by iteration. The residuals of the velocity, energy, and k-epsilon equations are small and a sample residual convergence plot for the plain double pipe heat exchanger is shown in Figure 9.

3. Equations used in theoretical calculation

Reynolds number is given by the relation,

$$Re = \frac{uD_h}{\Upsilon} \tag{4}$$

and the hydraulic diameter D_h is given by the difference between the inner diameter of the outer tube and the outer diameter of the inner tube [4]. For the plain profile, Nusselt number is given by

$$Nu = \frac{hD_h}{k} \tag{5}$$

and the heat transfer coefficient

$$h = \frac{Q}{(A \cdot \Delta T_{hot})}. \tag{6}$$

For the tooth profile, Nusselt number [3] is given by

$$Nu = 0.0405 Re^{0.608} \frac{H_f}{D_h}^{-1.03} \frac{W_f}{D_h}^{-0.908}. \tag{7}$$

The Nusselt number of the plain model is in the range of 0.5, whereas the Nusselt number of the tooth model is about 6 times larger. The lower Nusselt number for the plain model indicates a laminar flow with the domination by conduction whereas the higher Nusselt number for the tooth model indicates a transition zone in the flow path due to the presence of alternating teeth and cavities. Logarithmic mean (LMTD) of the temperature difference of the inlet and outlet is calculated both for the CFD and experimental values. The heat transferred based on the hot and cold fluids is calculated and the average heat transfer rate is used for the calculation of the overall heat transfer coefficient [6, 16]. The length of the model is kept constant for plain, rectangular, and triangular profiles. The overall heat transfer coefficient is calculated based on the temperature data, and flow rates based on the following equation [22].

$$U = \frac{q}{(A \cdot LMTD)} \tag{8}$$

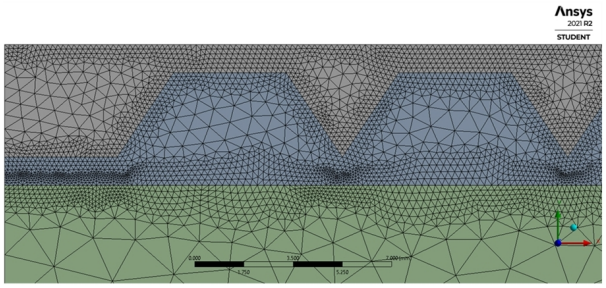

Figure 8. Mesh picture for heat exchanger with triangular labyrinth.

Item	Condition Taken
Solution Method	Pressure-Velocity Coupling
Scheme	Coupled
Gradient	Least squares cell based
Pressure	Second order
Momentum	Second order upwind
Turbulent kinetic energy	First order upwind
Specific dissipation rate	First order upwind
Energy	Second order upwind

Table 1. Details of the solution method.

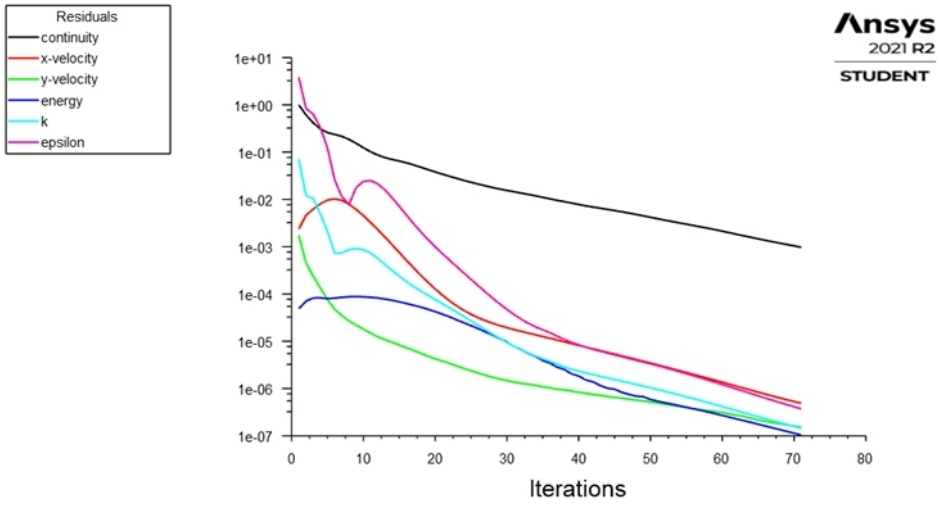

FIGURE 9. Convergence plot for plain heat exchanger.

S.No.	Specifications	Dimension [mm]
1	Inner diameter of the inner tube (d)	23.5
2	Thickness of the inner tube (ti)	4
3	Inner diameter of the outer tube (D)	33.5
4	Thickness of the outer tube (to)	2
5	Length of the heat exchanger (L)	160

TABLE 2. Dimensions of the heat exchanger tubes.

$$LMTD = \frac{(\Delta T_2 - \Delta T_1)}{\ln\left(\frac{\Delta T_2}{\Delta T_1}\right)} \tag{9}$$

4. Experiment details

Experiments are conducted for the parallel flow arrangement maintaining the mass flow rate of hot water at $0.4\,\mathrm{kg\,s^{-1}}$ in the annular region and the mass flow rate of cold water at $0.8\,\mathrm{kg\,s^{-1}}$ in the inner pipe. This corresponds to a Reynolds number of 20 000 and 43 000, respectively, when calculated based on the inlet velocity and the tube diameter [1]. The experiment setup consists of an inner tube made of copper where cold water is pumped from a storage tank. The outer tube is made of galvanized iron (GI) which has provision for hot water entry and exit. The hot water flows through the narrow annular gap between the inner copper pipe and the outer GI pipe. The dimensions of the heat exchanger tubes are stated in Table 2.

Temperatures are measured at the entry and exit points of hot and cold fluids with the help of sensors and their output signals are fed to the system through Arduino. The flow rates of the hot and cold fluids are measured by water flow sensors and their output signals are also logged by Arduino codes. The inlet temperature of the hot fluid is maintained at 350 K and the inlet temperature of the cold fluid is maintained at 295 K. The final assembly of the double pipe heat exchanger is shown in Figure 10.

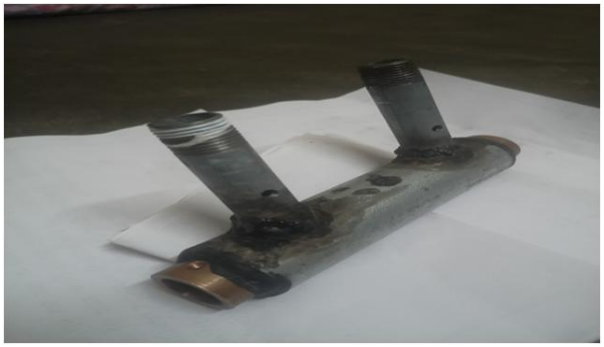

FIGURE 10. Assembly of the inner and outer pipe.

Applications with low mass flow rates give rise to a mixed condition in which the effect of forced convection and free convection are of an equal importance [23]. The flow rate in the annular region is kept small in order to initiate the mixed convection to achieve a better heat transfer. As the rectangular cavities show a better performance in the numerical analysis, the annular flow path in the heat exchanger is modified by machining rectangular grooves in the inner copper tube to investigate the improvement in the heat transfer coefficient [6]. The outer surface of the inner tube becomes geometrically unique with alternating ridges and grooves. The experiments are repeated with the same conditions for the plain profile and the rectangular cavity profile, which are shown in Figure 11 and Figure 12, respectively.

Figure 11. Outer surface of the inner pipe with plain profile.

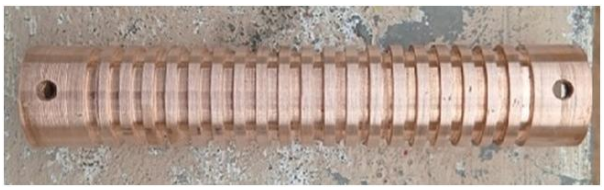

Figure 12. Outer surface of the inner pipe with rectangular profile.

5. Results and discussion

The heat exchanger performance can be improved by making the surface area larger, which is possible by increasing the diameter or the length of the heat exchanger. In this work, the heat exchanger length is increased and the effect on heat transfer characteristics is analysed. The initial condition considered is the hot fluid in the annulus at $0.4\,\mathrm{kg\,s^{-1}}$ and cold fluid in the inner pipe at $0.8\,\mathrm{kg\,s^{-1}}$. At the reduced length of 0.16 m, the temperature drop of the hot fluid is equal to the temperature rise of the cold fluid (Figure 13). The length is increased to 0.5 m and then to 1.5 m. When the length of the heat exchanger increases, the temperature drop of the hot fluid is higher than the temperature rise of the cold fluid though the flow rate of the cold fluid is higher.

The annular fluid is now changed to cold at $0.8\,\mathrm{kg\,s^{-1}}$ flow rate and pipe fluid to hot at $0.4\,\mathrm{kg\,s^{-1}}$ (Figure 14). Even now, the temperature drop of the hot fluid is higher than the temperature rise of the cold fluid, and the difference further increases with increased length.

When the flow rate of the hot and cold fluids is interchanged, the temperature rise of the cold fluid is higher than the temperature drop of the hot fluid (Figure 15).

The above results confirm that the heat exchange by the annular fluid is higher when the annular flow area is reduced in the manifold as compared to the inner pipe area. Hence, the annular fluid is fixed as hot water with a flow rate of $0.4\,\mathrm{kg\,s^{-1}}$ and the pipe fluid is fixed as cold water with a flow rate of $0.8\,\mathrm{kg\,s^{-1}}$ with the length of the heat exchanger fixed at 0.16 m to achieve a better heat transfer.

The calculation of the overall heat transfer coefficient is based on the inner surface of the tube, since the calculation based on the outer tube area may provide biased results [6]. The comparison of the overall heat transfer coefficient obtained from the numerical analysis is shown in Figure 16. The overall heat transfer coefficient of the rectangular labyrinth profile is twice than that of the plain profile and the value for the triangular labyrinth profile is in between the rectangular labyrinth and plain models. Hence, only the plain and rectangular labyrinth profiles are considered for experimental testing. The temperature plot for the plain and rectangular profiles is shown in the Figures 17 and 18, respectively.

Three replicates of testing are carried out for both the plain and rectangular cavity configurations. Temperature data are recorded every 10 seconds and the temperature used for the comparison is taken at a stable condition. Initially, the plain copper tube is placed inside the outer GI pipe and the temperature sensors are mounted on the inlets and outlets of the hot and cold pipes. One flow sensor is connected for each hot and cold pipes and the output signals of all the sensors are connected to the Arduino module. The experiment results support the findings from the numerical analysis that the tooth with a rectangular cavity labyrinth profile is having better heat transfer characteristics as compared to the plain profile. Figure 19 provides the comparison of numerical and experiment results of the plain and rectangular labyrinth heat exchangers.

Though the overall heat transfer coefficient is underestimated by the CFD analysis, this approach remains non-detrimental as the experimental testing shows a better exchanger performance than predicted [24]. When compared to the conventional heat exchanger with a finned inner tube, a significant reduction in pressure drop is achieved without affecting the heat exchanger performance. This result indicates that, for the double pipe heat exchanger model, it is an innovative way to provide vortex generators through labyrinth structures for the improvement of heat transfer. In other words, using the heat transfer enhancement technique presented in this paper, the modified double pipe heat exchanger can be a good choice for a situation that requires large quantity of heat to be removed in a limited heat exchanger volume.

6. Conclusion

Increased heat exchange can be achieved by increasing the heat transfer surface area, increasing the heat transfer coefficient, or creating turbulence in the flow of hot fluids. The increase in the exchange surface area by increasing the heat exchanger size directly increases the cost of the fabrication. The increase in the heat transfer coefficient requires increase in the flow velocity and Reynolds number, which needs modification in the process parameters. Hence the improvement is achieved by modifying the outer surface of the inner tube by creating turbulence in the flow. In the present work, three different lengths (0.16 m, 0.5 m and 1.5 m) are considered for CFD analysis in order to understand the effect of length on the heat exchange by annular fluid. Experiments are conducted for hot fluid mass flow rate of $0.4\,\mathrm{kg\,s^{-1}}$ in the annular region, and cold fluid mass flow rate of $0.8\,\mathrm{kg\,s^{-1}}$ in the inner

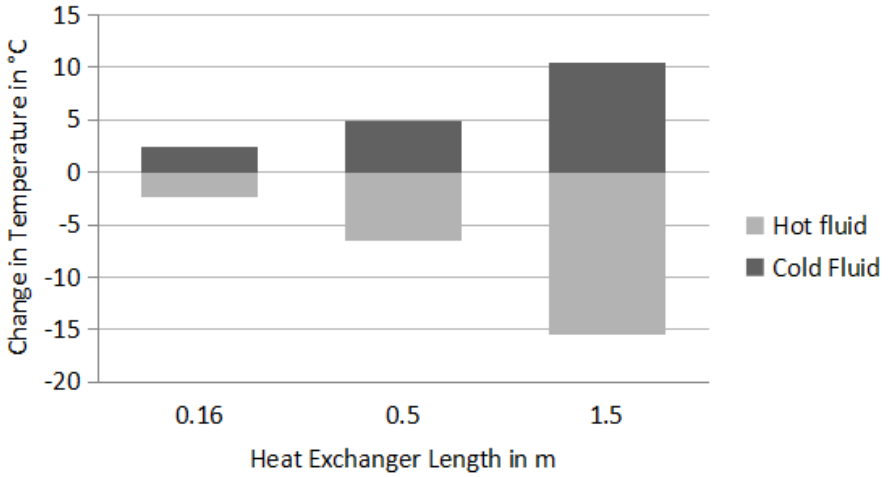

FIGURE 13. Effect of increasing the heat exchanger length (Hot fluid in annulus at $0.4\,\mathrm{kg\,s^{-1}}$).

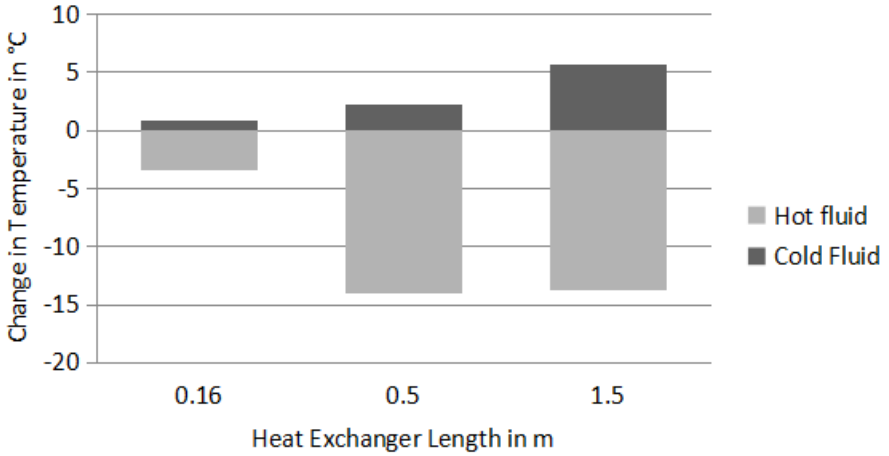

FIGURE 14. Effect of increasing the heat exchanger length (Hot fluid in inner pipe at $0.4\,\mathrm{kg\,s^{-1}}$).

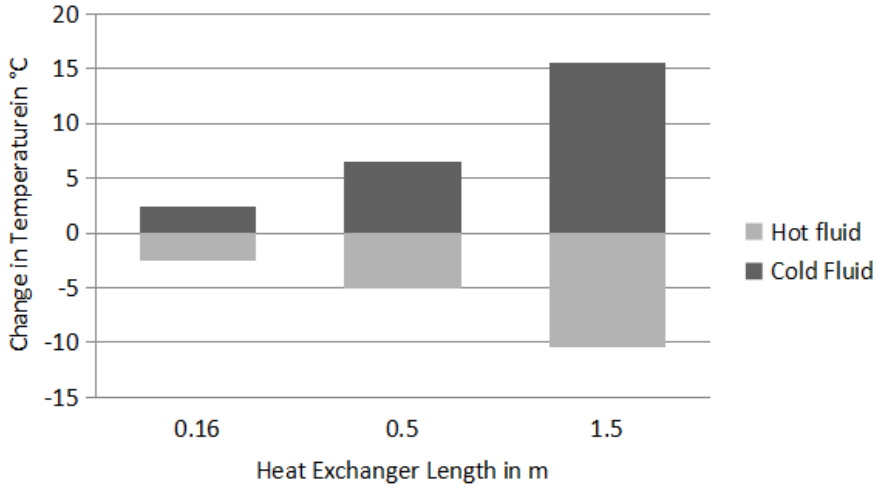

FIGURE 15. Effect of increasing the heat exchanger length (Hot fluid in inner pipe at $0.8\,\mathrm{kg\,s^{-1}}$).

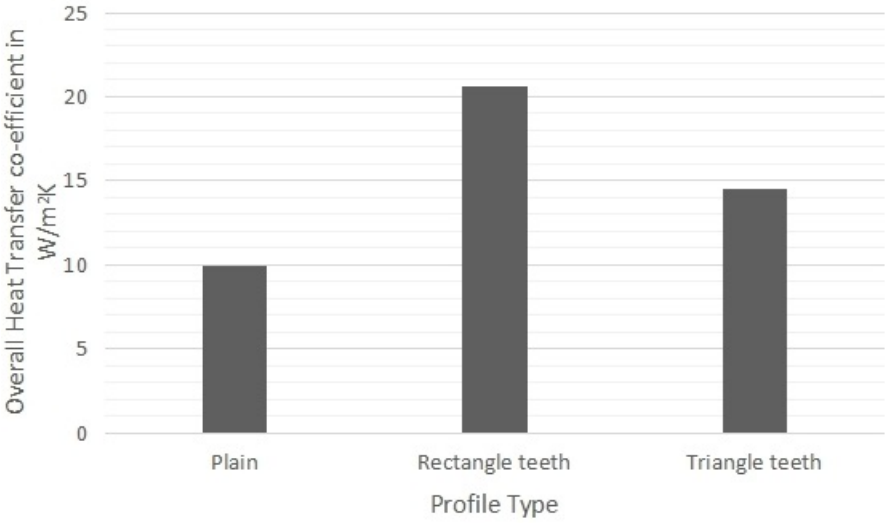

Figure 16. Comparison of overall heat transfer coefficient for CFD results.

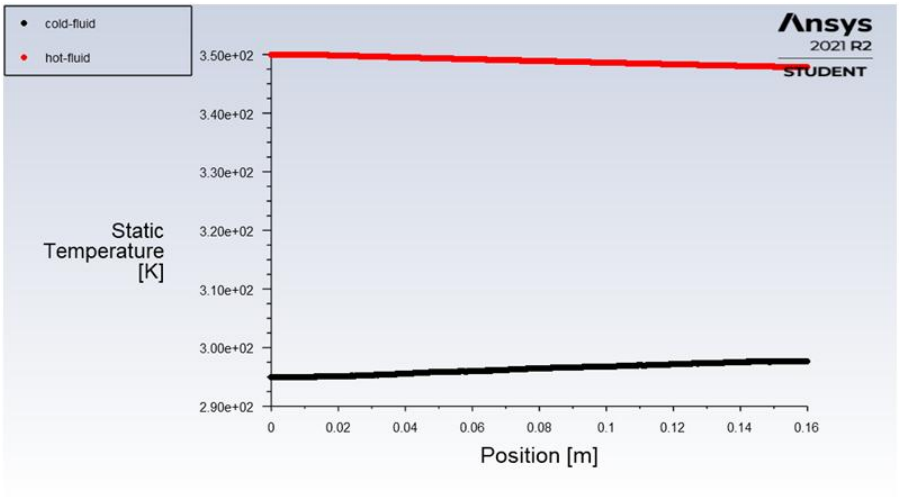

Figure 17. Temperature plot for plain heat exchanger.

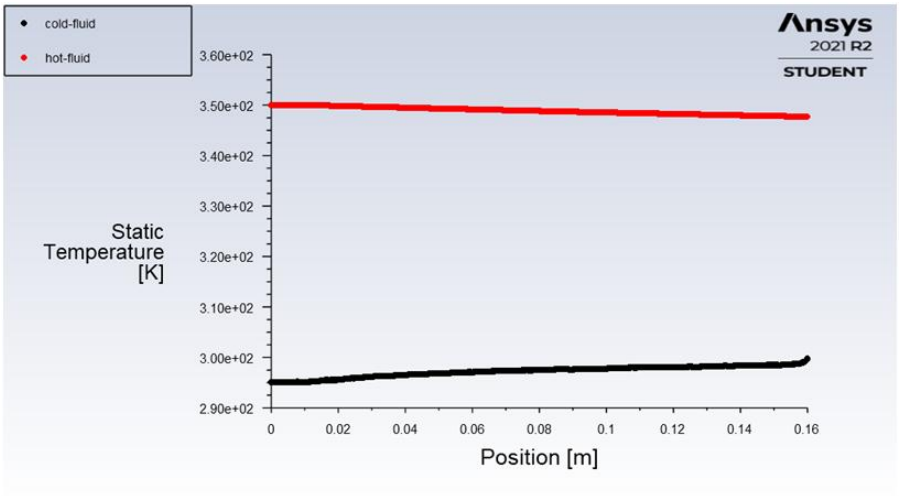

Figure 18. Temperature plot for rectangular labyrinth heat exchanger.

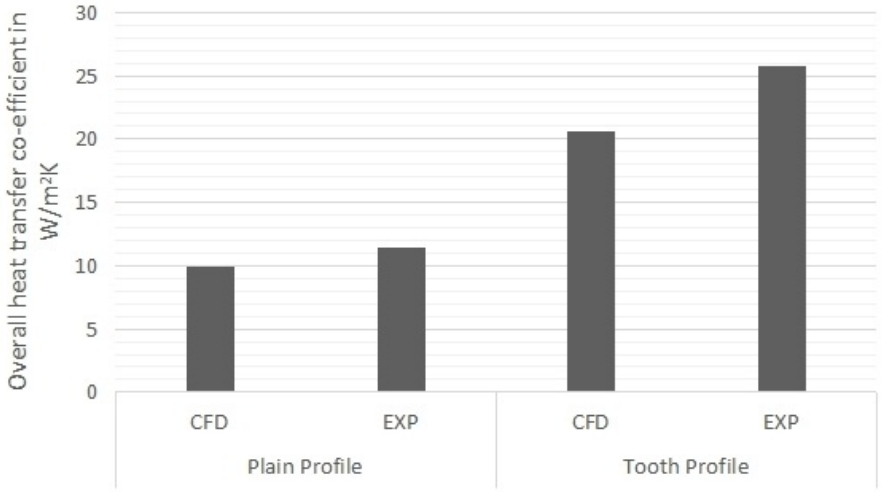

FIGURE 19. Comparison of experiment and numerical results.

pipe, with a constant length of 0.16 m. It is observed that heat transfer rate increases with reduced annular flow area. This effect is predominant when the flow rate of the pipe fluid is higher than the flow rate of the annular fluid and when the length of the heat exchanger increases. The heat transfer further improves when the plain annular flow path is replaced with labyrinth structures and rectangular cavity labyrinths are found to be better performing than the triangular cavity labyrinth. A two-dimensional axisymmetric model was analysed using ANSYS FLUENT software and the results are comparable with the experiment results.

LIST OF SYMBOLS

značka popis značky [jednotka]

ρ density [$\mathrm{kg\,m^{-3}}$]

u velocity [$\mathrm{m\,s^{-1}}$]

D_h hydraulic diameter [m]

Υ kinematic viscosity [$\mathrm{m^2\,s^{-1}}$]

h heat transfer co-efficient [$\mathrm{W\,m^{-2}K^{-1}}$]

k thermal conductivity [$\mathrm{W\,m^{-1}K^{-1}}$]

Q heat transferred [W]

A heat exchanger area [$\mathrm{m^2}$]

H_f height of the tooth [m]

W_f pitch of the tooth [m]

U overall heat transfer coefficient [$\mathrm{W\,m^{-2}K^{-1}}$]

T temperature [K]

Re Reynolds number (Dimensionless)

Nu Nusselt number (Dimensionless)

ΔT_1 difference between hot and cold fluid temperatures at entry

ΔT_2 difference between hot and cold fluid temperatures at exit

$LMTD$ Logarithmic Mean Temperature Difference

REFERENCES

[1] A. Lemouedda, A. Schmid, E. Franz, et al. Numerical investigations for the optimization of serrated finned-tube heat exchangers. *Applied Thermal Engineering* **31**(8-9):1393–1401, 2011. https://doi.org/10.1016/j.applthermaleng.2010.12.035

[2] J. M. Gorman, K. R. Krautbauer, E. M. Sparrow. Thermal and fluid flow first-principles numerical design of an enhanced double pipe heat exchanger. *Applied Thermal Engineering* **107**:194–206, 2016. https://doi.org/10.1016/j.applthermaleng.2016.06.134

[3] L. Duan, X. Ling, H. Peng. Flow and heat transfer characteristics of a double-tube structure internal finned tube with blossom shape internal fins. *Applied Thermal Engineering* **128**:1102–1115, 2018. https://doi.org/10.1016/j.applthermaleng.2017.09.026

[4] L. Zhang, H. Guo, J. Wu, W. Du. Compound heat transfer enhancement for shell side of double-pipe heat exchanger by helical fins and vortex generators. *Heat and Mass Transfer* **48**:1113–1124, 2012. https://doi.org/10.1007/s00231-011-0959-5

[5] R. Bhadouriya, A. Agrawal, S. Prabhu. Experimental and numerical study of fluid flow and heat transfer in an annulus of inner twisted square duct and outer circular pipe. *International Journal of Thermal Sciences* **94**:96–109, 2015. https://doi.org/10.1016/j.ijthermalsci.2015.02.019

[6] D. Majidi, H. Alighardashi, F. Farhadi. Experimental studies of heat transfer of air in a double-pipe helical heat exchanger. *Applied Thermal Engineering* **133**:276–282, 2018. https://doi.org/10.1016/j.applthermaleng.2018.01.057

[7] W.-L. Chen, W.-C. Dung. Numerical study on heat transfer characteristics of double tube heat exchangers with alternating horizontal or vertical oval cross section pipes as inner tubes. *Energy Conversion and Management* **49**(6):1574–1583, 2008. https://doi.org/10.1016/j.enconman.2007.12.007

[8] X. Tang, X. Dai, D. Zhu. Experimental and numerical investigation of convective heat transfer and fluid flow in twisted spiral tube. *International Journal of Heat and Mass Transfer* **90**:523–541, 2015. https://doi.org/10.1016/j.ijheatmasstransfer.2015.06.068

[9] W. El-Maghlany, E. Eid, M. Teamah, I. Shahrour. Experimental study for double pipe heat exchanger with rotating inner pipe. *International journal of advanced scientific and technical research* **4**(2):507–527, 2012.

[10] E. Ozden, I. Tari. Shell side CFD analysis of a small shell-and-tube heat exchanger. *Energy Conversion and Management* **51**(5):1004–1014, 2010. https://doi.org/10.1016/j.enconman.2009.12.003

[11] A. K. Agrawal, S. Sengupta. Laminar fluid flow and heat transfer in an annulus with an externally enhanced inner tube. *International Journal of Heat and Fluid Flow* **14**(1):54–63, 1993. https://doi.org/10.1016/0142-727X(93)90040-T

[12] J. Taborek. Double-pipe and multitube heat exchangers with plain and longitudinal finned tubes. *Heat Transfer Engineering* **18**(2):34–45, 1997. https://doi.org/10.1080/01457639708939894

[13] R. Raj, N. S. Lakshman, Y. Mukkamala. Single phase flow heat transfer and pressure drop measurements in doubly enhanced tubes. *International Journal of Thermal Sciences* **88**:215–227, 2015. https://doi.org/10.1016/j.ijthermalsci.2014.10.004

[14] S. P. Asok, K. Sankaranarayanasamy, T. Sundararajan, et al. Pressure drop characteristics of water flow through static annular and triangular cavity labyrinth seals. *Engineering Applications of Computational Fluid Mechanics* **2**(4):482–495, 2008. https://doi.org/10.1080/19942060.2008.11015246

[15] S. Eiamsa-ard, S. Pethkool, C. Thianpong, P. Promvonge. Turbulent flow heat transfer and pressure loss in a double pipe heat exchanger with louvered strip inserts. *International Communications in Heat and Mass Transfer* **35**(2):120–129, 2008. https://doi.org/10.1016/j.icheatmasstransfer.2007.07.003

[16] M. M. Aslam Bhutta, N. Hayat, M. H. Bashir, et al. CFD applications in various heat exchangers design: A review. *Applied Thermal Engineering* **32**:1–12, 2012. https://doi.org/10.1016/j.applthermaleng.2011.09.001

[17] C. V. M. Braga, F. E. M. Saboya. Turbulent heat transfer, pressure drop and fin efficiency in annular regions with continuous longitudinal rectangular fins. *Experimental Thermal and Fluid Science* **20**(2):55–65, 1999. https://doi.org/10.1016/S0894-1777(99)00026-6

[18] L. Sun, C.-L. Zhang. Evaluation of elliptical finned-tube heat exchanger performance using CFD and response surface methodology. *International Journal of Thermal Sciences* **75**:45–53, 2014. https://doi.org/10.1016/j.ijthermalsci.2013.07.021

[19] H. Huisseune, S. De Schampheleire, B. Ameel, M. De Paepe. Comparison of metal foam heat exchangers to a finned heat exchanger for low reynolds number applications. *International Journal of Heat and Mass Transfer* **89**:1–9, 2015. https://doi.org/10.1016/j.ijheatmasstransfer.2015.05.013

[20] M. I. Kim, Y. Lee, B.-W. Kim, et al. CFD modeling of shell-and-tube heat exchanger header for uniform distribution among tubes. *Korean Journal of Chemical Engineering* **26**:359–363, 2009. https://doi.org/10.1007/s11814-009-0060-7

[21] H. Nemati, M. A. Moghimi. Numerical study of flow over annular-finned tube heat exchangers by different turbulent models. *CFD Letters* **6**(3):101–112, 2014.

[22] T. J. Rennie, V. G. S. Raghavan. Experimental studies of a double-pipe helical heat exchanger. *Experimental Thermal and Fluid Science* **29**(8):919–924, 2005. https://doi.org/10.1016/j.expthermflusci.2005.02.001

[23] T. Maré, N. Galanis, I. Voicu, et al. Experimental and numerical study of mixed convection with flow reversal in coaxial double-duct heat exchangers. *Experimental Thermal and Fluid Science* **32**(5):1096–1104, 2008. https://doi.org/10.1016/j.expthermflusci.2008.01.002

[24] S. Freund, S. Kabelac. Investigation of local heat transfer coefficients in plate heat exchangers with temperature oscillation IR thermography and CFD. *International Journal of Heat and Mass Transfer* **53**(19-20):3764–3781, 2010. https://doi.org/10.1016/j.ijheatmasstransfer.2010.04.027